Subtype-specific postmitotic transcriptional programs controlling dendrite morphogenesis of Drosophila sensory neuron(Dissertation_全文)

AUTHOR(S):

Hattori, Yukako

Subtype-specific postmitotic transcriptional programs controlling dendrite morphogenesis of *Drosophila* sensory neuron

Yukako Hattori

Abstract

Precise differentiation of neuronal subtypes ensures functional nervous systems. In addition to precedent studies on transcriptional programs in neural stem cells, more recent work sheds light on executive roles of transcriptional factors (TFs) at postmitotic stages. However, there are few genome-wide studies to assess just how different these postmitotic TF-directed programs that direct distinct traits of multiple subtypes are. More specifically, little was known about how divergent the corresponding binding sites and target genes of such TFs would be.

To reveal the underlying transcriptional programs, I employed the stereotyped organization of identified dendritic arborization (da) neurons in *Drosophila* as a model system. I focused on a BTB-zinc finger protein Abrupt (Ab) and a member of the Early B-Cell Factor/Olfactory 1 family, Knot (Kn), which act as selectors of distinct dendritic arbor morphologies of two classes of da neurons, termed class I and class IV, respectively, and performed binding-site mapping and transcriptional profiling of isolated these neurons. Their binding profiles were significantly similar to each other and enriched in cell-type specific enhancers of genes implemented in neural development. I identified a total of 429 target genes, of which 56 were common to Ab and Kn, and these targets included genes that were necessary for shaping dendritic arbors of either or both of the two classes. Furthermore, I found that a common target gene, encoding a cell adhesion molecule Ten-m, was expressed more

strongly in class I than IV, which was critical to the class-selective directional control of dendritic branch sprouting or extension. My analyses illustrate how differentiating neurons employ unique and common repertoires of gene expression to produce the class-selective morphological traits.

Table of Contents

List of abbreviations

kn	*knot*
ab	*abrupt*
ct	*cut*
Ten-m	*Tenascin major*
da neuron	dendritic arborization neuron
md neuron	multiple dendrite neuron
AEL	after egg laying
Dam	DNA adenine methyltransferase
DamID	Dam identification
GFP	green fluorescent protein
MARCM	Mosaic analysis with a repressible cell marker
BSs	binding sites
HOT	high occupancy target regions or hotspots
ME	misexpression
OE	overexpression
GO	Gene Ontology
LOF	loss of function
GOF	gain of function

Chapter 1

Introduction

Chapter 1. Introduction

1-1. Precise differentiation of neuronal subtypes ensures functional nervous systems

In early development of multicellular organisms, cell diversification occurs on a large scale with spectacular complexity and precision (Figure 1). Among all organs, the nervous system contains by far the greatest cellular diversity, as well as tremendous complexity in cellular connectivity (Figure 1B). To generate this incredible system, developing animals need to orchestrate large numbers of regulatory genes in temporally and spatially precise manners. This heavy task, encoded in the genome, is prerequisite for the emergence of functional neuronal circuits at later developmental stages.

The specified neuronal types can be distinguished from one another on the basis of a number of criteria of terminal differentiation, ranging from anatomies, such as elaboration of specific dendrite arbors and formation of axonal connectivity patterns, to electrophysiological properties (Sugino et al., 2006). One mechanism yielding these variations operates in neural stem cells that exhibit a cascade expression of different transcriptional factors (Figure 2 (Bertrand et al., 2002; Hobert et al., 2010; Southall and Brand, 2009). A distinct mechanism would be that expression of key transcriptional factors (TFs) are initiated not in dividing progenitors cells, but in postmitotic cells, and those postmitotic TFs realize cell-type variations (Figure 3 and Figure 4; Dalla Torre di Sanguinetto et al., 2008; Fishell and Hanashima, 2008; Vrieseling and Arber,

2006). Evidence for the latter mechanism has been reported more recently under some developmental contexts, such as diversification of spinal motor neurons into discrete subpopulations (Figure 3). However there have been few systematic searches for binding profiles of such postmitotic TFs in the genome, or inventories of their target genes. Consequently, when I focused on TFs that direct distinct traits of multiple subtypes within the same category of neurons, little was known about how divergent the corresponding binding sites and target genes would be.

1-2. The *Drosophila* dendritic arborization (da) neurons

One of the signature neuronal hallmarks exploited for this study is the diverse morphology of the dendritic arbor, which supports differential processing of synaptic or sensory inputs, thereby realizing functional variations (Figure 5; Hausser and Mel, 2003; Jan and Jan, 2003; London and Hausser, 2005). The underlying transcriptional programs can be revealed with appropriate model systems, such as the stereotyped organization of identified dendritic arborization (da) neurons in *Drosophila* (Figure 6), which have contributed much to elucidating both the genetic controls underlying the morphological diversity of dendritic arbors and the physiological functions of nociception and proprioception (Corty et al., 2009; Grueber et al., 2002; Im and Galko; Jan and Jan; Landgraf and Evers, 2005). At the mature larval stage, da neurons in the abdominal hemisegment are classified into 4 categories, classes I-IV, in order of increasing territory size and/or branching complexity (Figure 7; Grueber et al., 2002). Class I neurons are characterized by formation of simple comb-like small

dendritic arbors and contribute to proprioception (Figure 7 and Figure 8). On the other hand, class IV neurons develop far more complicated and expansive ones and play roles in somatosensory nociception (Figure 6A, Figure 7, and Figure 9). Mammalian skin also possesses multiple types of mechanoreceptors that sense distinct stimuli such as skin stretch, movement or pain (Figure 10).

1-3. Ab and Kn are class-specific transcription regulators that control dendrite morphogenesis

A group of TFs play pivotal roles in this class specification in postmitotic cells. The founding member is a homeodomain protein, Cut (Ct), which is differentially expressed among the three classes II-IV and controls class-specific arbor shapes (Figure 7; Grueber et al., 2003). In addition to this multi-level selector, a BTB-zinc finger protein Abrupt (Ab) and a member of the Early B-Cell Factor/Olfactory 1 family, Knot (Kn; also designated as Collier), are selectively expressed in class I and IV, respectively, and each endows the class-I or IV-specific dendritic pattern (Figure 11-14; Crozatier and Vincent, 2008; Hattori et al., 2007; Jinushi-Nakao et al., 2007; Li et al., 2004; Sugimura et al., 2004). For example, In contrast to a control class I neuron that forms the simple comb-like dendritic arbor, the same class I misexpressing *kn* dramatically increases in the number of branch terminals, which I call class IV-like (Figure 14C and 14D). A series of loss- or gain-of-function conditions of Ab or Kn do not dramatically affect the expression of the other respective TF in the embryo, providing no strong evidence for an epistatic relationship between these two TFs (Hattori et al., 2007). Several target genes of these TFs are known or suggested

by candidate approaches (Crozatier and Vincent, 2008; Hattori et al., 2007; Jinushi-Nakao et al., 2007); however, genome-wide views have hitherto not been presented.

1-4. Overview of this study

Here I focused on transcriptional programs that are directed by the class I selector Ab and the class IV selector Kn. I searched for target genes of Ab and/or Kn on a whole genome scale to better understand how each TF regulates class-selective differentiation, and highlighted a subset of the target genes that are required for shaping the dendritic arbors of both or either of class-I or IV; I then focused on a particular target gene, and how it contributes to producing the class-selective morphological traits (Figure 15 and Figure 16).

Chapter 2

Results

Chapter 2. Results

Section 1. Identification of Ab or Kn target genes

2-1-1. Identification of in vivo binding sites (BSs) of Ab or Kn on a whole-genome scale

To identify target genes regulated by Abrupt (Ab) and Knot (Kn), I started profiling in vivo binding sites (BSs) by the DamID method (Figure 17A; Choksi et al., 2006; van Steensel et al., 2001; van Steensel and Henikoff, 2000). In brief, I expressed Ab or Kn, which had been fused with the Escherichia coli DNA adenine methyltransferase (Dam), at a very low, i.e. leaky, level in embryos in order to methylate GATC sequences adjacent to the BSs of the respective TFs. I hybridized amplified methylated genomic fragments to tiling arrays. Data of four independent replicates of the arrays were processed to determine the representative BS profile (Figure 17B, Figure 18, and Figure 19). On the basis of my objective standards, I defined BSs of each TF, as well as Ab- or Kn-"bound" genes (Figure 20, Figure 21, and Table S1). Our analysis defined 2665 Ab-bound genes and 2652 Kn-bound genes (for the definition of a bound gene and numbers of genes bound by TFs in embryos in comparison to previous studies, see 4-3. Analysis of DamID data). 48% of the bound genes of one TF were overlapped by the other (Figure 21B). The common bound genes are designated as the Ab/Kn-bound genes hereafter.

Distributions of these BSs were analyzed with respect to positions

inside or outside genes, and showed large proportions within 5 kb upstream of the transcriptional start site (28.0% and 26.7% for Ab and Kn, respectively), and binding within introns (35.7% and 30.0% for Ab and Kn, respectively; Figure 22A). Enrichment analysis of individual genomic regions in the BSs supported the view that the BSs tended to be excluded from coding sequences and untranslated regions (CDS and UTR in Figure 22B). These findings are consistent with results of other transcription factor-binding studies and regulatory sequence studies in *Drosophila* embryos, and cell lines of mice and humans (Birney et al., 2007; Chen et al., 2008; Southall and Brand, 2009).

2-1-2. Expression profiling of isolated da neurons revealed that Ab and Kn binding resulted in both activation and repression of their target genes

The above BS data did not yield information about whether they are target genes in da neurons or not, since Ab and Kn are also expressed in cell types other than da neurons (Dubois et al., 2007; Hu et al., 1995). To complement my DamID analysis, I isolated da neurons from larvae and obtained genome-wide expression profiles under the conditions where ectopic expression of *ab* or *kn* in all classes of da neurons severely affected morphologies of dendritic arbors, presumably due to altered levels of transcription of target genes of each TF (Figure 23). For simplicity, I designated this expression style as misexpression or ME throughout this study. I identified 1508 genes that were up- or down-regulated by *ab* ME and 451 by *kn* ME (Figure 24A, 24B, respectively). These genes were designated as *ab*- or *kn*-“dependent” genes (Table S1D and S1E). Annotations of the dependent genes were enriched in GO terms such as

“actin cytoskeleton organization,” “cell adhesion,” and “transport” (Figure 25).

2-1-3. Identification of 429 Ab and/or Kn target genes, out of which 56 were common

Cross-referencing the *ab* ME data set with the set of the Ab-bound genes showed that 196 up-regulated and 190 down-regulated genes were identified as Ab-bound genes. Thus, I designated these 386 genes as Ab “target” genes, or simply “targets” hereinafter (Figure 24A, 24C, and Table S1F), and strictly distinguished them from the bound genes that were defined on the basis of the DamID data alone. Likewise, 99 *kn*-dependent genes (59 up and 40 down) were designated as Kn target genes (Figure 24B, 24C, and Table S1G). I confirmed the increase or the decrease in the expression levels of a subset of target genes by immunohistochemistry and/or qPCR (Table S2; see also Figure 26). For example, the expression of *lola*, one of the up-regulated targets of Ab and Kn, is increased in *ab* ME or *kn* ME larvae, and decreased in *ab* or *kn* mutant embryos (Figure 26). The fact that the number of Ab targets identified is four-times more than that of Kn targets might reflect the longer duration of Ab expression (from embryos till mature larvae) than that of Kn expression, which is no longer detected in the larvae (Shimono et al., 2009). The total number of Ab and/or Kn targets was 429, of which 330 (85%) were unique to Ab (Figure 24C). The number of up-regulated or down-regulated genes suggests that Ab and Kn act as both transcriptional activators and repressors.

One naive expectation had been that at least a subset of the 56 common target genes would be regulated by Ab and Kn in opposite ways.

Unexpectedly however, there were no such targets; each of the 56 common target genes was either up-regulated by both Ab and Kn, or down-regulated by both Ab and Kn. I thought it possible that some common targets are regulated by the two TFs in quantitatively differential fashions, and such candidates are lined up in my microarray analysis under the *ab* ME or *kn* ME conditions (Table S1H). In fact, I confirmed such differential control of gene expression when I examined individual target genes, such as *lola* and *Ten-m* (discussed later). Out of the complete lists of the *ab* or *kn*-dependent and the bound genes (Table S1C), those implicated in neuronal differentiation or neuronal functions and miRNA genes are selected and enumerated in Table S3.

Section 2. Binding profiles of Ab and Kn

2-2-1. Co-occurrence of Ab and Kn BSs in comparison to those of other TFs

To compare BSs of Ab and/or Kn with those of other TFs, I clustered BSs for a total of 35 TFs by using *Drosophila* modENCODE data set (Figure 27) and found a strong correlation between the Ab BSs and Kn BSs (Figure 28). This result strengthened the possibility that the Ab/Kn-bound genes are transcriptionally regulated in (a) similar developmental context(s). This possibility appears to be consistent with my survey of Gene Ontology (GO) annotations of the Ab-bound genes and the Kn-bound ones, which showed a highly significant overrepresentation of the terms such as “neuron differentiation” in both gene groups (Figure 29). Our clustering also showed that both the Ab BSs and the Kn BSs were highly correlated with the BSs of a transcriptional co-repressor Gro that is shown to control class I dendrite morphogenesis (Figure 28; Parrish et al., 2006).

2-2-2. The BSs of Ab and/or Kn target genes were enriched in genomic regions that are classified into tissue specific enhancers and Polycomb chromatin

I then inspected the BSs of Ab or Kn by taking advantage of integrative data sets of histone modifications and chromatin components (Figure 30). Chromatin features of the *Drosophila* genome have been classified into five “chromatin

types” defined by DamID analysis of cell line Kc167 (RED, YELLOW, BLACK, BLUE, and GREEN; Figure 31; Filion et al., 2010) or nine “chromatin states” defined by ChIP-chip of BG3 or S2 cells (states 1~9; Figure 31; Kharchenko et al., 2010). I first confirmed that the combinatorial patterns of enrichments or paucities of the markers (such as those shown in Figure 30) are basically conserved among the cell lines, embryos that I used for DamID, and third-instar larvae from which I isolated da neurons for the expression profiling (Figure 32; see legend), although it would be ideal to obtain neuronal class-specific data sets and respective chromatin landscapes for each class of da neurons. Then I correlated BSs of the Ab or Kn target genes with the chromatin types or states (Figure 33, Figure 34).

For both Ab and Kn, the most prominent selectivity was manifested by the large fractions of the target BSs, especially the BSs of up-regulated targets, in the RED chromatin type that is transcriptionally active in a tissue-specific fashion (UP of Ab BS and UP of Kn BS in Figure 33A; Filion et al., 2010), and in state 3 chromatin that is classified into enhancers and intronic regulatory elements (UP of Ab BS and UP of Kn BS in Figure 33C; Kharchenko et al., 2010). This selectivity was also highlighted by the fold enrichment relative to the fractions of RED type or state 3 in the entire genome (see red boxes with black frames in Figure 33B and 33D). Most noticeably, RED type chromatin includes 50.0% of the BSs of Ab up-regulated targets, and its enrichment is 5.4 fold. State 3 is shown to be abundant in introns, being consistent with the enrichment of the DamID BSs in introns (Figure 22). Another less conspicuous but significant enrichment was seen in genomic regions that are marked by Polycomb group

(PcG) proteins or “Polycomb chromatin” (BLUE and state 6). It should be noted that BLUE and state 6 chromatins may not invariably mean transcriptionally silenced regions; one proposal is that a subregion of Polycomb chromatin is in a “balanced state,” where Polycomb group proteins and active markers coexist (Schwartz et al., 2010). In addition to Ab and Kn, I analyzed published data for the transcription factor Pros, which acts as a binary switch between self-renewal and differentiation in neural stem cells (Choksi et al., 2006), and characterized BSs that mapped to its target genes. BSs of the Pros target genes were also more prevalent in RED/state 3 and Blue/state 6 than the other classifications, but with a stronger preference for Blue/state 6 (see Pros BS in Figure 33).

Section 3. Targets with a broad range of molecular functions execute dendritic arbor formation

2-3-1. Target genes that contributed to dendrite morphogenesis of class I and/or IV

To examine roles of the target genes in dendrite morphogenesis, I selected 103 target genes out of the 429 on the basis of GO annotations and carried out their knockdown and/or overexpression in class I and IV neurons (Figure 35; see details 4-9. RNAi). Listed in Table S4 are 24 target genes whose knockdown phenotypes were validated with two distinct dsRNA sequences. Overexpression of 10 out of the 24 genes caused malformation of dendritic arbors. As for target genes whose null or strong alleles have been reported, I examined phenotypes of mutant neurons and obtained results essentially consistent with those obtained by knockdown analysis (described later in Figure 38). Many of these targets are conserved across species and have eluded previous knockdown or mutant screenings of dendrite morphogenesis (Gao et al., 1999; Parrish et al., 2006; Satoh et al., 2008; Ye et al., 2007; Zheng et al., 2008).

I expected that Ab targets and Kn targets would be transcriptionally up- or down-regulated by Ab in class I da neurons and by Kn in class IV, respectively, and such regulations would be required for sculpting dendrite arbors in each class-selective fashion. Indeed, *spinster* (*spin)*, encoding a protein implicated in endosome-to-lysosome transport (Dermaut et al., 2005; Sweeney and Davis, 2002), is one of the up-regulated targets of Ab*,* and its knockdown deformed the

comb-like shape of class I arbors (Figure 36A and 36B). Secondary branches, which are supposed to grow along the anterior-posterior axis (A-P axis) in a parallel manner, were misoriented to each other; consequently, the arbor size increased compared to that of the control, although the terminal number did not (Figure 36H, 36I). *spin* encodes a multimembrane-pass protein implicated in endosome-to-lysosome transport (Dermaut et al., 2005; Sweeney and Davis, 2002), and my results support the hypothesis that Ab-dependent up-regulation of *spin* and the role of Spin in membrane trafficking in class I are pivotal for its comb-like arbor formation. Likewise, one of the Kn targets, *CG14642*, which is predicted to encode a protein with a serine-type endopeptidase activity, was required specifically for spatial control of branching within the class IV arbor (Figure 37A and 37B). This was shown by the facts that *CG14642* knockdown did not alter the terminal number (Figure 37F) or the cumulative length of the arbor (Figure 37G), but caused a significant shift of branching activity to the proximal area in the arbor (Figure 37H).

In contrast to the Ab or Kn selective targets, the common targets were expected to play important roles in both class I and IV neurons. Consistent with this prediction, knockdown of four up-regulated targets significantly deformed both class I and IV arbors (Figure 36C-36D, 37C-37D, 38A-38D, and Table S4), as shown by the decrease either in the terminal number (Figure 36H, Figure 37F) or in the length per branch (Figure 37G), or by misdirections of branch extension (Figure 45, Figure 47; explained later). These targets are *dOrai*/*Olf186-F*, *lola*, *CG31431*, and *Ten-m*, which encode a Ca2+ release-activated Ca2+ channel (Agrawal et al., 2010; Venkiteswaran and

Hasan, 2009), a transcription regulator that controls neural development (Giniger et al., 1994; Spletter et al., 2007), a putative fibroblast growth factor-activated receptor, and a type-II transmembrane protein Ten-m (that is further characterized below), respectively. To examine whether the molecular network that includes dOrai controls dendritic arborization or not, I knocked down the gene encoding Stromal interaction molecule (dSTIM) that is localized on the ER and binds to dOrai, or *iptr* encoding the IP_3 receptor (Figure 39). The knockdown of *dSTIM* or *iptr* also significantly reduced the number of class I and class IV branches (Figure 39C-39H), supporting a critical contribution of the intracellular Ca2+ homeostasis regulation pathway in both classes.

On the other hand, knockdown of some of the common targets caused severe phenotypes in one of the two classes, and these include *Imp*, *Pak3*, or *tai* of the up-regulated group. For example, Knockdown of *Insulin growth factor II mRNA binding protein* (*Imp*), implicated in post-transcriptional events such as translational inhibition, RNA localization and RNA stabilization (Adolph et al., 2009; Boylan et al., 2008; Yisraeli, 2005), dramatically reduced the length of class IV arbors, but its effect on class I was not detected, at least with regard to the number of branch termini (Figure 36E, 36H, 37E, 37F, 37G, 38E-38H, 38K-38M).

Our overexpression experiments raise the possibility that quantitative control of expression of some of the target genes is critical for proper arbor development of class IV. For example, in contrast to the severe simplification of the arbor by the *Imp* knockdown as described above (Figure 37E), its overexpression increased the branch number (Figure 40A, 40C, and 40E). As

for *lola*, both knockdown and overexpression resulted in arbor simplification (Figure 37D and 40D). It is thus possible that the *lmp* and *lola* levels must be adequately controlled to determine the arbor complexity. Another instance was given by *spin* overexpression, which simplified class IV arbors (Figure 40B). These phenotypes are consistent with a hypothesis that *spin* expression should be repressed below a certain level for normal class IV development.

2-3-2. Kn-target genes that were required for Kn misexpression-induced transformation of dendritic arbor shapes

I further assessed the biological relevance of the targets in the context of Kn misexpression-induced transformation of dendritic arbor shapes. Misexpression of Kn in class I neurons increases the number of higher-order branches and deforms the comb shape, which I designate as a class IV-like transformation (Figure 41A and 41B; Hattori et al., 2007). I assumed that up-regulation of the Kn target genes most likely contributed to this class IV-like transformation (Figure 41E). To verify this hypothesis, I misexpressed Kn in class I neurons with concurrent knockdown of individual Kn target genes. Out of the six up-regulated targets which I showed were required for class IV arbor formation, knockdowns of five significantly suppressed the class IV-like transformation phenotype of class I neuron ddaE (Figure 41C, 41D, 41F and 41G; Table S4). Most notably, knockdown of *lola* or *dOrai* restored the class IV-like arbor to normal class I with respect to both the branch number and the comb-like shape (Figure 41C, 41D, 41F and 41G). Due to a technical difficulty, I was unable to address the relevance of the Ab targets in the Ab misexpression-induced context (see 4-9.

RNAi). Nonetheless, these results of my integrated approaches identified a group of target genes that were bound by either key TF, were transcriptionally regulated, and contributed to morphological diversification of the two classes of the da neurons (Figure 42).

Section 4. One common target gene *Ten-m* controls class-selective dendritic branch sprouting or extension

2-4-1. Knocking down a common target gene, *Ten-m*, in class I or IV altered directional features of branch sprouting or extension

To obtain mechanistic insights into the morphological diversification of dendritic arbors achieved by Ab and Kn target genes, I studied one of the common target genes, which encodes a homophilic cell adhesion molecule of the teneurin family, Tenascin major (Ten-m; Figure 43), in further depth. Ten-m is necessary for pathfinding decisions in motor axon navigation (Zheng et al., 2011) and instructs synapse organization in the olfactory circuit and at neuromuscular junctions (Figure 44; Hong et al., 2012; Mosca et al., 2012). I first showed that *Ten-m* RNAi worked efficiently in class I and IV neurons (Figure 52C-52D') and examined knockdown phenotypes (Figure 45-47).

I focused on the morphological features of class I ddaE, whose secondary branches sprout from the dorsally-oriented primary ones, with a significant posterior preference (Figure 45B). Those secondary branches extend along the anterior (A)-posterior (P) axis. The knockdown abrogated the directional preference of the branch sprouting, making comparable numbers of secondary branches sprout in both A and P directions (Figure 45C and 45D). I also examined another class I vpda (Figure 46; see legend).

To characterize phenotypes of class IV ddaC, I performed quantitative analyses using several parameters and found a significant alteration in neither

the total dendrite length, the number of branch termini, nor spatial disposition of branches within the dendritic arbor (data not shown). Instead, I found that the knockdown showed a significantly biased directional distribution of terminal branches (Figure 47). Compared to the control ddaC, branches under the knockdown conditions extended in a less radial manner.

2-4-2. Ten-m was more highly expressed in class I than IV, and in overlying epidermis in a non-uniform fashion

It has been shown that various types of neurons employ Tenurins to pair with target cells expressing the same Tenurin subclass (Figure 44 and 48; Hong et al., 2012; Leamey et al., 2007). So I speculated that dendritic branches of the da neurons might interact with adjacent cells by way of homophilic interactions of Ten-m. To explore this possibility, I primarily monitored *Ten-m* expression by detecting the *Ten-m* enhancer-dependent expression of a reporter in the respective *GAL4* enhancer trap line (Figure 49A; Hong et al., 2012) and found that Ten-m was expressed both in class I and class IV neurons and also in non-neuronal tissues such as epidermis, a subset of muscles (Mosca et al., 2012), and hemocytes (Figure 49B-49C, 49E-49F Figure 50). The expression patterns were intriguingly differential in two respects: (1) Ten-m was expressed much more strongly in class I than class IV (Figure 49B, 49B', 49E, and 49E'), which is consistent with higher activation by *ab* ME than *kn* ME (Table S1H). I also showed that this expression in class I was reduced in the *ab* mutant (Figure 51), which validated my identification of *Ten-m as* one of the Ab target genes. In addition to the *Ten-m* enhancer-dependent reporter expression, I found that

endogenous Ten-m signals were much stronger in class I than class IV (Figure 52). (2) The expression in the epidermis, which makes direct contacts with dendrites (Figure 53; Han et al., 2012; Kim et al., 2012a; Parrish et al., 2009), was non-uniform. It was higher in a stripe about three epidermal cells wide, encompassing neuronal cell bodies and proximal dendrites, than in the more distal zone (Figure 49B-49D, 49G). These results allowed me to posit that Ten-m may work both in the neuron and adjacent tissues to prompt dendrite patterning, and that the imbalance of Ten-m in the epidermis provides the directional cue for the branch sprouting of class I ddaE from the higher to lower Ten-m level (Figure 49G).

2-4-3. Knocking down or overexpression of *Ten-m* in adjacent tissues also abrogated directional features of branches

Next, I examined phenotypes of class I ddaE and class IV ddaC, when *Ten-m* was knocked down or overexpressed in adjacent tissues. To analyze knockdown phenotypes of ddaE, the drivers employed were *Ten-m-GAL4* for knockdown in all *Ten-m*-expressing cell types, and *arm-GAL4* for knockdown in adjacent tissues such as epidermis and muscles (Parrish et al., 2009). All knockdowns tested abrogated the directional preference of the branch sprouting (Figure 54). To verify the hypothesis that the imbalance of Ten-m in the epidermis provides the directional cue for the branch sprouting, I overexpressed *Ten-m* in the *hh* domain within epidermis (Figure 55), where *Ten-m* expression during development is normally much lower than in the proximal dendrite zone (Figure 49C, 55A, and 55B). In control larvae, secondary dendrites grew in the

hh domain (Figure 55C and 55C'); in striking contrast, branches were hardly seen in the *Ten-m* overexpressing domains (Figure 55D and 55D', and 55F). Moreover, the normal directional bias of sprouting of ddaE secondary branches was significantly impaired (Figure 55E). These results suggested that the dendritic branches did not ascend the presumptive counter slope of Ten-m in the epidermis (Figure 55B). These results of the knocking down or overexpression experiments are consistent with my hypothesis.

To address whether *Ten-m* in adjacent tissues contributes to dendrite morphogenesis of class IV ddaC or not, I knocked down *Ten-m* in all *Ten-m*-expressing cell types (Figure 56). In addition, I knocked down *Ten-m* selectively in the *hh* domain in the epidermis (see green zones in Figure 57C and 57D) that belongs to the Ten-m-low distal zone (Figure 57A-57D, 57K-57P). Compared to the control ddaC, extension of terminal branches under either knockdown condition was significantly biased along the A-P axis (Figure 57M and 57P), as it was when *Ten-m* was knocked down in the neuron (Figure 47G and 47H). Importantly, the directional distribution of terminal branches was not altered on the side opposite to the *hh* domain (magenta zones in Figure 57C and 57D, 57E-57J), strongly suggesting that the *Ten-m*-mediated dendrite-epidermis interaction locally contributed to orienting terminal branches in the wild type. These results lead me to speculate that in normal development the ddaC dendrites, once they enter the Ten-m-low zone, are prompted to arborize and direct their termini essentially in all directions, which most likely allows efficient coverage of the body surface with branches (Figure 6A and Figure 7; Grueber et al., 2002).

2-4-4. *Ten-m* overexpression in class IV endowed a directional preference of branch extension, which is reminiscent of the normal class I arbor

The above results show that *Ten-m* was necessary for normal arbor formation of both classes. Then how does this common target gene produce the class-selective morphological traits? I was intrigued by the finding that class IV ddaC expressed *Ten-m*, but at a much lower level than class I ddaE (Figure 49B, 49B', 49E, 49E', and Figure 58A). So I addressed whether overexpression of *Ten-m* in ddaC affected its dendrite morphogenesis or not (Figure 58). The control ddaC neurons directed their branch termini to A and P directions nearly equally (Figure 58B, 58B', and 58F); in contrast, branch growth of *Ten-m*-overexpressing ddaC showed a posterior preference (Figure 58C, 58C', and 58F), which is reminiscent of a directional feature of the ddaE secondary branches (Figure 58D, 58D', and 58F). This phenotype of the *Ten-m* overexpressing-ddaC was not associated with a net decrease of the branch number (Figure 58G), excluding the possibility that the ddaE-like posterior preference was a consequence of overall arbor simplification. These results could be interpreted to mean that the elevated level of Ten-m in ddaC branches makes them respond to the higher-to-lower level of epidermal Ten-m towards the posterior border in each hemisegement, as class I ddaE does.

All of my results strongly suggest the possibility that the Ten-m-mediated interaction between dendritic branches and the epidermis produces the distinct directional outputs of branch growth in neuronal subclass-specific fashions (Figure 59). In class I ddaE, the Ten-m-high dendrites

responded to the epidermal high-low Ten-m imbalance, realizing the predominantly posterior-oriented comb-like pattern of class I ddaE; in class IV ddaC, the low-level expression in the neurons and the epidermis ensures the relatively radial pattern of terminal branches. Thus my data of Ten-m provides mechanistic insights into how the differential expression of Ten-m contributes to producing the class-selective morphological traits.

Chapter 3

Discussion

Chapter 3. Discussion

In this study, I uncovered the programs of the two TFs that govern two distinct neuronal subtypes (Figure 60). I had speculated how divergent the Ab-directed and the Kn-directed transcriptional regulations would be, because the classes I and IV do indeed form arbors with distinct shapes and the sizes and execute distinct physiological functions, yet both belong to the same subfamily of sensory neurons (Grueber et al., 2002). Our study strongly suggests that both Ab- or Kn-specific targets together with common targets shape the dendrites of individual classes. Thus, most likely these partially overlapped transcriptional programs generate different gene expression and coordinated actions of these gene products form the class-specific dendrite morphologies.

3-1. Targets with a broad range of molecular functions execute dendritic arbor formation in a class-selective fashion

The transcriptional programs of my focus were predicted to be more specialized for controlling neuronal terminal differentiation at postmitotic stages, compared to those in which proneural genes, such as Asense and its vertebrate homolog Ascl1 (Mash1), regulate cell proliferation or cell cycle arrest and also promote differentiation (Castro et al., 2011; Southall and Brand, 2009). Indeed, predicted molecular functions of Ab and Kn target-coded proteins are diverse, ranging from transcriptional control to cell adhesion, membrane trafficking, Ca2+ entry, and cytoskeleton regulation. Table S4 includes many targets that are conserved across species and have eluded previous knockdown or mutant screenings of

dendrite morphogenesis (Gao et al., 1999; Parrish et al., 2006; Satoh et al., 2008; Ye et al., 2007; Zheng et al., 2008), with some exceptions such as BicD in class IV (Bianco et al., 2010) and an overexpression phenotype of Lola (Ou et al., 2008). Thus, the genes listed in this study potentially include a number of novel key regulators.

To sculpt dendrite arbors in a class-selective fashion, one naive hypothesis would be that there are differential requirements for target genes in individual classes. Consistent with this hypothesis, I found Ab target genes (e.g., *spin*) that were necessary for developing the small comb-like arbor in class I, but their normal amount may not be required for higher-order branching and extensive growth of class IV arbors. Likewise, some Kn targets, *CG14642* and *Imp*, play critical roles in developing the class IV arbor, but their knockdown did not cause severe defects in the class I arbor formation. Most likely, Ab controls transcription of the targets in class I neurons, as does Kn in class IV in normal development. It appears that molecular activities of these gene products have to be optimized in each class to define morphological parameters such as the branching complexity. This speculation is based on my observations that *spin* OE in class IV neurons decreased the number of terminal branches (Figure 40B) and that *Imp* knockdown and its OE provided a vivid contrast (Figure 37E and Figure 40C).

3-2. The comparisons uncovered three common features of the Ab and Kn transcriptional programs

Our genome-wide study showed that Ab and Kn had three features in common,

as summarized below: (1) In the entire genome, there was a strong correlation between the Ab BSs and the Kn BSs (Figure 28) and a large overlap of the bound genes (Figure 21B). (2) When confined to the BSs of target genes, those of either TF were enriched in RED type or state 3 chromatins that are annotated as enhancers or other regulatory elements of tissue specific genes, and this property was the most prominent with the BSs of the up-regulated target genes (Figure 33). One caveat of this result is that the chromatin types/states are defined on the basis of data sets of cultured cell lines, so it would be ideal to obtain neuronal class-specific data sets and depict chromatin landscapes of each class. (3) Every common target was regulated in the same direction (up-regulated or down-regulated) by Ab and Kn under my experimental conditions. These similarities may be a consequence of the fact that both classes belong to da neurons and their substantial portions of differentiation processes might be similar. Most likely, Ab in class I and Kn in class IV preferentially bind the same or distinct enhancers of common target genes and regulate their expression.

3-3. Quantitative differences in the expression level

Then how do these targets contribute to shaping dendrite arbors in the class-selective fashion? Our genome-wide study strongly supports the notion that the class selectors do indeed control transcription of target genes selectively. On the other hand, both TFs have chromatin features of the BSs in common and show the same directional (up or down) regulation of every common target. To explain these findings, I was intrigued by the possibility that some common

targets might be regulated by the two TFs in quantitatively differential fashions. As a precedent, Cut (Ct) is differentially expressed among the three classes (class II-IV; Figure 7), which controls formation of the different branching patterns and the growth of dendritic arbors of individual classes (Grueber et al., 2003). In this study, compelling data for the above hypothesis was obtained by my analyses of a common target, *Ten-m*. Its high-level expression in class I ddaE endowed its branches with the capability to respond to the decreasing level of Ten-m in the epidermis, thus setting the directional preference of branch sprouting (left, in Figure 59). In contrast, a much lower expression in class IV ddaC ensured the directing of terminal branches rather radially in the distal area of each arbor, where the overlying epidermal *Ten-m* expression is low (right, in Figure 59). These level-dependent roles of Ten-m could be related, or analogous to a role of mouse Ten-m3 in navigating Ten-m3-high retinal projections to the high target region (Figure 48; Leamey et al., 2007; Young and Leamey, 2009) and those of Tenurins in instructing synaptic partner matching in the *Drosophila* olfactory map (Figure 44; Hong et al., 2012). Most recently, a role of zebrafish Ten-m3 in shaping the connectivity of retinal ganglion cells has been reported (Antinucci et al., 2013). It awaits further study to reveal how the differential levels of Ten-m produce the class-selective directional properties of branch patterning, possibly by way of organization of cytoskeletons and membranes (Mosca et al., 2012).

Our other experimental results are also consistent with the critical role of the quantitative control of target gene expression. First, the amount of Lola, one common target-gene product, was higher in class I ddaE than class IV ddaC

in a wild type background (Figure 26). Second, results of knockdown and overexpression of *Imp* and *lola* indicate that their expression levels must be strictly controlled to determine the arbor complexity. Third, I had superficially puzzling findings about down-regulated targets (those with decreased expression upon *ab* or *kn* ME). In the narrowed-down list of Ab target genes (Table S4), 10 targets were down-regulated by *ab* ME, and their knockdown in class I (which expresses Ab endogenously) yielded obvious abnormal phenotypes. Ab may keep the transcription of the down-regulated targets weakly active, and does not totally shut down the expression; moreover, this low-level expression may be required for normal class I development. To test these hypotheses, what would be required is class-selective quantitative expression profiling, ideally at multiple developmental stages, including the onset of primary dendrite formation and a subsequent branch growing phase. Quite recently, class-I or class-IV specific expression profiling at a mature larval stage has been reported (Iyer et al., 2013).

3-4. Transcriptional regulation of Ab and Kn in concert with other TFs

85% or more of the bound genes were not identified as exclusively Ab and/or Kn-dependent genes; and it could be that Ab and Kn may be able to control transcription of some of those in conjunction with other TFs. Candidate bound genes of this group include Kn-bound genes *Ubx* and *abd-A*, that are silenced in class IV by PcG proteins, which showed a similar binding profile with Kn (Figure 33; Parrish et al., 2007), while an unknown transcriptional co-activator may drive expression of *turtle*, which is an Ab/Kn-bound gene necessary in class I and IV

(Long et al., 2009). Furthermore, with respect to physiological functions of proprioceptive class I and multi-modal nociceptive class IV (Figure 8-9), it should be mentioned that Gr28b encoding a bright blue light sensor was a Kn-bound gene (Table S3A). Misexpression of Ct in all da neurons and external sensory (es) neurons, which caused defects in dendritic morphology and axon pathfinding, severely disrupted larval crawling behavior (Hughes and Thomas, 2007). Therefore, Ab or Kn target genes that yielded strong loss-of-function phenotypes in dendrite arbor formation may also play roles in the physiological functions. Additional profiling data sets, such as that in the co-presence of Kn and Ct, will deepen my understanding of the intricate transcription codes, with the ultimate goal of identifying the molecular links between the codes and the diverse architectures of dendritic arbors and neuronal functions.

My genome-wide analyses illustrate how differentiating neurons at postmitotic stages employ unique and common repertoires of gene expression to produce the class-selective morphological traits. The underlying mechanisms operant in the neuronal subtypes may provide at least a subset of general principles that direct cell diversification throughout multicellular organisms.

Chapter 4

Materials and methods

Chapter 4. Materials and methods

4-1. *Drosophila* strains

I used *GAL4*$^{21\text{-}7}$ *UAS-mCD8:GFP* (Song et al., 2007), *UAS-abL* and *UAS-abS* (Sugimura et al., 2004), *UAS-Kn:HA* (Hattori et al., 2007), *GAL4*$^{2\text{-}21}$ *UAS-mCD8:GFP* (Grueber et al., 2003), *ppk-GAL4 UAS-mCD8:GFP* on the 2nd chromosome (Kimura et al., 2006) or on the 3rd chromosome (Grueber et al., 2007), *UAS-dicer2* and RNAi stocks (Vienna *Drosophila* RNAi Center), *UAS-spin-RFP* (gift from S. Sweeney and G. Davis), *UAS-Imp-SD* (Boylan et al., 2008) and *Imp*^{8} (Munro et al., 2006), *UAS-lolaL* (Spletter et al., 2007) and *FRT42D lola*^{C46} (Horiuchi et al., 2003), *NP6658*-GAL4 (*Ten-m-GAL4*; *Drosophila* Genomics Resource Center) *UAS-ten-m* (Mosca et al., 2012), *FRT82B pnr*^{VX6} and *arm-GAL4* (Bloomington Stock Center), *hh-GAL4* (Tanimoto et al., 2000), *ppk-CD4:tdGFP* and *ppk-CD4:tdTom* (Han et al., 2011) and sensory organ precursor (SOP)-FLP stocks (Matsubara et al., 2011). The GAL4/UAS system was used for targeted gene expression (Figure 61). Fly embryos and larvae were grown at 29 °C for RNAi and overexpression experiments and at 25°C for other experiments.

4-2. DamID

I expressed Ab or Kn, which had been fused with the Escherichia coli DNA adenine methyltransferase (Dam), at a very low, i.e. leaky, level in embryos in order to methylate GATC sequences adjacent to the BSs of the respective TFs. I

amplified methylated genomic fragments and hybridized them to tiling arrays. Data of four independent replicates of the arrays were processed to determine the representative BS profile (Figure 18).

To express Dam fusion proteins, I first constructed pUAST-NDam and pUAST-CDam plasmids by cloning the Dam-Myc sequence from pNDamMyc and pCMycDam (van Steensel et al., 2001), respectively, into the multiple cloning site of pUAST (Brand and Perrimon, 1993). Full-length coding sequences from *ab* and *kn* were amplified from cDNA clones RE25924 and RE03728, respectively, and cloned into pUASTNDam or pUASTCDam. *UAS* transgenic lines were generated and a reference stock *UAS-Dam* has been described previously (Choksi et al., 2006). These Dam fusion proteins were expressed in eye discs using *GMR-GAL4* (Bloomington 8605). On the basis of their subcellular localization and expression levels in comparison to those of Dam, *UAS-Abrupt:Dam* and *UAS-Dam:Knot* lines were selected for the following experiments.

I expressed the Dam fusion proteins in da neurons and examined dendrite phenotypes. Forced expression of Ab:Dam in classes II-IV neurons downsized and simplified their dendritic arbors, transforming them into class I-like, phenocopying misexpression of Ab (Sugimura et al., 2004); likewise, Dam:Kn expression in classes other than IV increased the complexity of their dendritic arbors, as Kn misexpression does (data not shown; Hattori et al., 2007). These results supported the assumption that each fusion protein bound to regulatory sequences of the presumptive target genes that I looked for.

For DamID, stage 17 embryos (17–20 h AEL) of the following genotypes were

collected: *yw*; *UAS-Dam/+*, *yw*; *UAS-Abrupt:Dam/+*, or *yw*; *UAS-Dam:Knot/+*. To express the Dam or the Dam fusion proteins at a leaky level, *GAL4* drivers were deliberately omitted from the expression protocol. DNA isolation, processing, and amplification were performed as described previously (Choksi et al., 2006). The DNA samples were labeled with Cy3 or Cy5 and hybridized to a custom whole-genome tiling array with 60-mer oligonucleotides spaced at ~300 bp intervals (Choksi et al., 2006), and four biological replicates were performed. Arrays were scanned and intensities were extracted (NimbleGen Systems). Log2 mean signal ratios of TF-Dam/Dam at individual spots were median scaled, and four binding profiles for each of Ab:Dam or Dam:Kn were obtained.

4-3. Analysis of DamID data

Scaled log2 ratios were preprocessed as previously described (Kind et al., 2008; Schwartz et al., 2006). The following formula was used to standardize variances of scaled log2 ratios of each replicate:

$Z = (X - \mu)/\sigma$

(X: scaled log2-ratio, μ: mean of scaled log2-ratio, σ: standard deviation of scaled log2-ratio).

The standardized log2-ratios of the four replicates (“Ab rep.1-rep.4 and Kn rep.1-rep.4” in Figure 18) were averaged and smoothed by using a 1400 bp window centered on each probe to correct for variability in probe annealing properties (“smoothed” in Figure 18). Within the Ab or Kn replicates, every profile was highly correlated with the other (Figure 19A and 19B); in contrast, this was not the case between the different TF replicates (Figure 19C).

Binding sites (BSs) were defined as follows: the distributions of the smoothed ratios were skewed towards positive values (raw distributions or “Raw” in Figure 20). All statistics falling below the mode (red lines in Figure 20) were used to estimate the left side of the null distribution (Schwartz et al., 2006); then the full null distribution was obtained by reflecting the left side of the null distribution onto the right side of the mode (van Steensel et al., 2003). The null distribution was subtracted from the raw distribution (“Raw – Null” in Figure 20C and 20D) and threshold values were set as 3σ of the null distribution (blue lines in Figure 20C and 20D). The regions with signal ratios above the thresholds were defined as BSs. Consequently, only 0.15% of estimated noise was included in the BSs. Bound genes were defined as follows: genes containing BSs were chosen; if a BS was located between two genes, I chose both (Figure 21A). The tool for presenting the binding profile and viewing genomic data sets was the University of California-Santa Cruz (UCSC) Genome Browser (e.g., Figure 17B; Fujita et al., 2011).

The number of bound genes of the following TFs are: 1,214 (Prospero), 1,082 (Asense), 1,243 (Snail), and 696 (Deadpan), as reported previously by DamID studies using *Drosophila* embryos (Choksi et al., 2006; Southall and Brand, 2009), although it should be noted that BSs and bound genes are defined somewhat differently from this study. In (Southall and Brand, 2009) and (Negre et al., 2011), bound genes are defined when a binding event occurs within 5kb (Asense, Snail, and Deadpan) or up to 1kb (Prospero) of the gene structure. On the other hand, I did not set a limit on the distance of the gene from the BS. This was because previous studies on cis-regulatory elements show that the distance

from BSs of TFs to their target genes is quite variable (Haeussler and Joly, 2011). Our Dam:Knot Dam ID experiment was validated at least by detecting BSs 1.7 kb upstream of *kn* itself, which are used for auto-regulation in muscles (Dubois et al., 2007). BSs identified by DamID have been shown to match those identified by chromatin immunoprecipitation (Song et al., 2004; Sun et al., 2003; Tolhuis et al., 2006) and by 3D microscopy data (Guelen et al., 2008; Pickersgill et al., 2006). I conducted de novo motif analysis of Ab and Kn BSs by using MEME-ChIP (Machanick and Bailey, 2011), Cistrome SeqPos/CEAS (Shin et al., 2009) and rGADEM (Li, 2009), but did not obtain consistent results between these algorithms (data not shown).

Custom Perl scripts, R package (http://www.R-project.org), and the Bioconductor package were used for data analysis in general including calculations of fold enrichments essentially as described previously (Negre et al., 2011). For making heat maps, heatmap.2 in the gplots package of R was used. The Kn BSs in this study and those from the modENCODE data were not tightly clustered (Figure 28), possibly due to a difference of developmental stage, and such examples are seen in a previous report (Negre et al., 2011).

4-4. Expression profiling of isolated da neurons

To complement my DamID analysis, I isolated da neurons from larvae using magnetic beads, prepared RNA basically as described (Iyer et al., 2009) with modifications, and obtained genome-wide expression profiles.

da neurons were isolated from larvae of three distinct genotypes: *+/GAL4$^{21\text{-}7}$ UAS-mCD8:GFP* (control), *+/GAL4$^{21\text{-}7}$ UAS-mCD8:GFP; UAS-abL/+*

(*ab* ME), and *UAS-knL:HA/GAL4*$^{21\text{-}7}$ *UAS-mCD8:GFP* (*kn* ME). *GAL4*$^{21\text{-}7}$drives gene expression exclusively in multidendritic sensory neurons, including all da classes (Figure 23C-23E'; Song et al., 2007), but its expression was not strong enough in embryos. Consequently, I isolated da neurons using magnetic beads from larvae and prepared RNA basically as described (Figure 23A; Iyer et al., 2009), with the following modifications: 1) I dissected wandering third instar larvae, inverted their body walls in ice-cold dissecting saline, and immediately transferred them into SM[active] medium on ice (Nagoshi et al., 2010). 2) Biotin-conjugated anti-mouse CD8a antibody (Ly-2 of eBioscience) and a 1 ml dounce tissue grinder (Wheaton) were used. 3) Cell solutions were triturated by using a flame-rounded Pasteur pipette followed by a flame-rounded 200-μl pipetter tip with filter, until most of the tissues were dissociated to single cells. RNA was purified from 80 larvae of each genotype, making three sets of RNA samples.

The RNA samples were amplified with a WT-Ovation Pico RNA Amplification System (NuGEN), labeled, hybridized to Affymetrix *Drosophila* Genome 2.0 Arrays by Takara Bio Inc., and data of triplicates were obtained. Raw Affymetrix .CEL files were preprocessed using RMA (Irizarry et al., 2003). The data was analyzed using the Bioconductor limma package (Smyth, 2004) with the arrayWeights function to detect differential gene expression. Statistical significance of the results was determined using a moderated eBayes t-test. The resulting P-values were adjusted using FDR (Benjamini and Hochberg, 1995). Probe sets were mapped to genes using the annotation available in FlyBase (r5.35). I defined instances with the adjusted P-values < 0.05 as significant

changes. I found that the *ppk* level was down-regulated (the log2(fold change) was -2.31) by *ab* ME as expected from previous studies (Hattori et al., 2007).

I examined the increase or the decrease in the expression levels of a subset of target genes by qPCR and/or immunohistochemistry (see also 4-10. immunohistochemistry). For qPCR, ReverTra Ace and Thunderbird (TOYOBO) were used according to the manufacturers' instructions. Out of the twenty genes, using *gapdh* or *rp49* as a reference, the cDNA levels of fourteen (*Ten-m*, *lola*, *pak3*, *tai*, *Ptp10D*, *spin*, *ssp4*, *hts*, *CG14642 CG31140*, *CG31431*, *Gap1*, *pnr*, and *RhoGAP19D*) were either increased or decreased as shown in the microarray data and the fold changes are indicated in Table S2. For the other six (*dOrai*/*Olf186-F*, *Imp*, *dlp*, *SK*, *sog*, and *CG30080*), cDNA was not amplified from the control sample, thus fold-change could not be calculated.

Although I planned expression profiling of *ab* or *kn* loss-of-function conditions, the *ab* mutant was early larval lethal and only a small fraction of *kn* homozygous mutant embryos survived to late embryonic stages, making collection of enough numbers of da neurons from the mutant larvae prohibitively difficult. I also attempted to knock down *ab* or *kn* by using drivers such as *GAL4*$^{2\text{-}21}$ for class I or *ppk-Gal4* for class IV; however, cellular phenotypes were much less dramatic than those of *ab* or *kn* mutant clones possibly due to late onset of *GAL4* expression. Nonetheless, I argue that target genes I identified in this study include those that are indeed transcriptionally regulated by Ab or Kn and contribute to dendrite morphogenesis under the control of Ab or Kn. Our supporting evidence is the following:

I confirmed that expression of *lola*, which is one of the up-regulated common

targets, was decreased in *ab* or *kn* mutant embryos, whereas it was increased in *ab* or *kn* ME/overexpression larvae (Figure 26).

ab ME or *kn* ME severely affected morphologies of dendritic arbors (Figure 23C-23E'), presumably due to altered expression levels of target genes. Out of the six up-regulated targets which I showed were required for class IV arbor formation, knockdowns of five of them significantly suppressed the *kn* ME class IV-like transformation phenotype of class I neurons (Figure 41; Table S4), supporting the idea that up-regulation of the Kn target genes that I identified contributed to the class IV-like transformation of class I neurons.

4-5. Databases

Throughout this study, genomic sequence coordinates of *Drosophila melanogaster* followed FlyBase genome Release 5.0 (McQuilton et al., 2012); and the reference gene list employed was FlyBase r5.35 containing a total of 15,191 genes. *Drosophila* modENCODE data (http://www.modencode.org/) and the genome-wide data of the chromatin signatures have been described (Filion et al., 2010; Kharchenko et al., 2010; Negre et al., 2011).

4-6. Functional Annotation Classification of Genes using Gene Ontology

For this clustering, an overrepresentation analysis for Gene Ontology (GO) entries was carried out. To this end, a Fisher's test was employed as implemented in the DAVID Bioinformatics Resource (Dennis et al., 2003). As a reference gene list, all genes from FlyBase r5.35 entries were used. Results are presented by either P-values that were adjusted using Benjamini-Hochberg's

multiple testing correction method (Figure 29) or enrichment score (Figure 25; Huang da et al., 2009).

4-7. Public database access of microarray data

The raw and processed data for the DamID- binding experiments and the expression profiling experiments described here are available on the GEO public database (http://www.ncbi.nlm.nih.gov/projects/geo/). The accession numbers are as follows: DamID data sets—GSE38659. Expression profiling—GSE38660.

4-8. Imaging dendritic trees, in situ hybridization

Protocols of single cell labeling (MARCM; Figure 62), imaging, quantitative analysis of the images, immunohistochemistry, and in situ hybridization were essentially as described (Hattori et al., 2007; Matsubara et al.; Yamamoto et al., 2006). Images were acquired from wandering 3rd instar wandering larvae unless described otherwise.

4-9. RNAi

Using the list of the target genes, I conducted a small-scale in situ hybridization screening and found that probes for genes with no GO annotation gave signals in embryos barely above the limit of sensitivity of my experimental conditions (data not shown). Thus, I selected 103 genes on the basis of GO terms and performed a primary RNAi screening. 32 genes exhibited morphological defects in dendritic arbors of class I and/or IV when knocked down. Out of these 32, I conducted a secondary RNAi screening using available transgenic stocks of

dsRNA targeted to other sequences; and I also examined the effects of overexpression of 11 genes whose UAS strains have been published. The *GAL4* drivers employed were *GAL4*$^{2\text{-}21}$ *UAS-mCD8:GFP* for class I and *ppk-Gal4 UAS-mCD8:GFP* on the 2nd chromosome for class IV. The RNAi efficacy of *lola* or *Ten-m* was assessed and verified by the reduction of antibody staining (Figure 36F-36G', 36J, and 52C-52D'). In knocking down or overexpressing each gene, 6-15 pairs of the class I neurons (ddaD and ddaE) and 3-15 class IV ddaC were observed, phenotypes were searched visually, and then quantitatively analyzed (Figure 36-37, and Figure 40).

To examine the effects of knockdowns of *ab* target genes on *ab* misexpression-induced transformation of the class IV dendritic arbor, I attempted to co-express *ab* and dsRNA of Ab target genes in class IV (for a purpose analogous to that of Figure 41). However, none of the class IV-selective *GAL4* drivers tested worked together with *ab* misexpression (Sugimura et al., 2004). Those were *ppk-Gal4*, *stj-GAL4(Ly et al., 2008)*, *GAL4*$^{4\text{-}77}$ (Emoto et al., 2004), and *Gr28b.c-GAL4* (Xiang et al., 2010). This was most likely because ectopic expression of *ab* shuts down promoters where *GAL4*-containig vectors are inserted (Hattori et al., 2007).

To knock down *Ten-m* in adjacent tissues such as epidermis, I examined expression patterns in several GAL4 drivers previously described (Parrish et al., 2009). I found that (1) *arm-GAL4* expression was high in epidermis and a subset of muscles, (2) *69B-GAL4* expression in epidermis was variable from one hemi-segment to another and sometimes it was absent in epidermis overlaying da neurons of the dorsal cluster (that was why I did not use

69B-GAL4 in this study), and (3) very low-level expression of *arm-GAL4* was detected in some ddaC-ddaE and that of *69B*-GAL4 was in ddaC, whereas *hh-GAL4* expression was detected in none of the da neurons (data not shown).

4-10. Immunohistochemistry

Antibodies employed for immunohistochemistry include anti-GFP (1:100, B2 of Santa Cruz; 1:500, Molecular Probe), anti-Lola (1:100; Giniger et al., 1994), anti-Ten-m (mAb 113, 1:100; mAb 20, 1:1000; Baumgartner et al., 1994; Levine et al., 1994), and Alexa Fluor 488- or Cy3-conjugated anti-HRP (1:200; Jackson ImmunoResearch). I followed (Grueber et al., 2003) for quantification of Lola signals (Figure 26D-26G and 36J). For quantification of mCD8:GFP signals in epidermis (Figure 49B'), I drew an epidermal region of interest (ROI) 10 μm in diameter, which did not include dendrites, and calculated the intensity per pixel. From each dorsal cluster, three ROIs were chosen, and each data point in Figure 49D represents an average pixel intensity of each ROI.

Other antibodies employed for immunohistochemistry were anti-Spin (1:250; Sweeney and Davis, 2002), anti-IMP (1:8000; Adolph et al., 2009), anti-Pak3 (1:1000; Bahri et al., 2010), and anti-Tai (1:2000; Bai et al., 2000). In contrast to restricted nuclear localization of Lola, the other proteins were distributed in both cell bodies and dendritic branches, making quantitative comparisons between genotypes difficult.

4-11. Statistical tests

The statistical tests employed are one-way ANOVA and HSD *post-hoc* test or

Wilcoxon-Mann-Whitney test, and KaleidaGraph (Synergy Software) was used for the calculations. Circular statistics and rose plots were generated in Oriana 4 (Kovach Computing Service) and PAST (Hammer, 2001). The frequency of observations in rose plots is represented by the area of each wedge.

Acknowledgements

First I would like to thank my advisor, Tadashi Uemura. I appreciate all his contributions of time, ideas, and supports to making my Ph.D. experience productive and stimulating. I also thank Kaoru Sugimura, Daisuke Satoh, and Tadao Usui for their invaluable assistance. Without their guidance and encouragement, I could never finish my PhD work.

I thank very much Katsuhiko Shirahige, Takehiko Itoh for their critical advices for bioinformatics; Kohei Shimono for his SOP-FLP reagents; members of Uemura's lab for discussion; and Yukiko Miyake, Kumiko Shimizu, Jyunko Mizukoshi, Kanae Oki and Mayumi Futamata for their technical assistance.

The reagents, genomic datasets, and/or facilities were provided by the *Drosophila* Genetic Resource Center at Kyoto Institute of Technology, the NIG stock center, the Bloomington Stock Center, Vienna *Drosophila* RNAi Center, the TRiP at Harvard Medical School, the Developmental Studies Hybridoma Bank at the University of Iowa, the *Drosophila* Genomics Resource Center (DGRC), FlyBase, modENCODE, Y.N. Jan, C. Han, S. Hayashi, H. Wada, S. Yonehara, Y. Kobayashi, T. Aigaki, D. St Johnston, A. Nose, E. Giniger, G. Davis, N. Harden, S. Adolph, D. Montell. L. Luo, T. Mosca, S. Baumgartner, and R. Wides. I also thank A.H. Brand, T.D. Southall, B. van Steensel, N.M. Luscombe, J.M. Vaquerizas, K. White, M. Ebisuya, T. Yamamoto, Y. Natsume, Y. Shinkai, M. Suyama and E. Nagoshi for advice on informatics or cell isolation and/or related reagents; J. Hejna for polishing the manuscript. I was funded by the Japan Society for the Promotion of Science fellowship for three years.

My time at Kyoto was made enjoyable considerably due to the many friends and groups that became a part of my life. I am grateful for time spent with members in Uemura Lab and other Labs. I also thank Akaimi preschool for offering childcare and opportunities for interaction with other families.

Lastly, I would like to thank my family for all their support and encouragement. I thank my parents who supported me in all my pursuits and took care of my daughter by staying in Kyoto for about one year. I thank my husband's parents who also helped my husband and me. Most of all, for my daughter and my husband whose faithful supports and encouragements are so appreciated. Thank you.

This doctoral dissertation is based on the following scientific paper.

Yukako Hattori, Tadao Usui, Daisuke Satoh, Sanefumi Moriyama,
Kohei Shimono, Takehiko Itoh, Katsuhiko Shirahige, and Tadashi Uemura
"Sensory-Neuron Subtype-Specific Transcriptional Programs
Controlling Dendrite Morphogenesis:
Genome-wide Analysis of Abrupt and Knot/Collier"
Developmental Cell, Volume 27, Issue 5, Pages 530–544, 2013
http://dx.doi.org/10.1016/j.devcel.2013.10.024
http://www.cell.com/developmental-cell/abstract/S1534-5807%2813%2900641-2

Figures

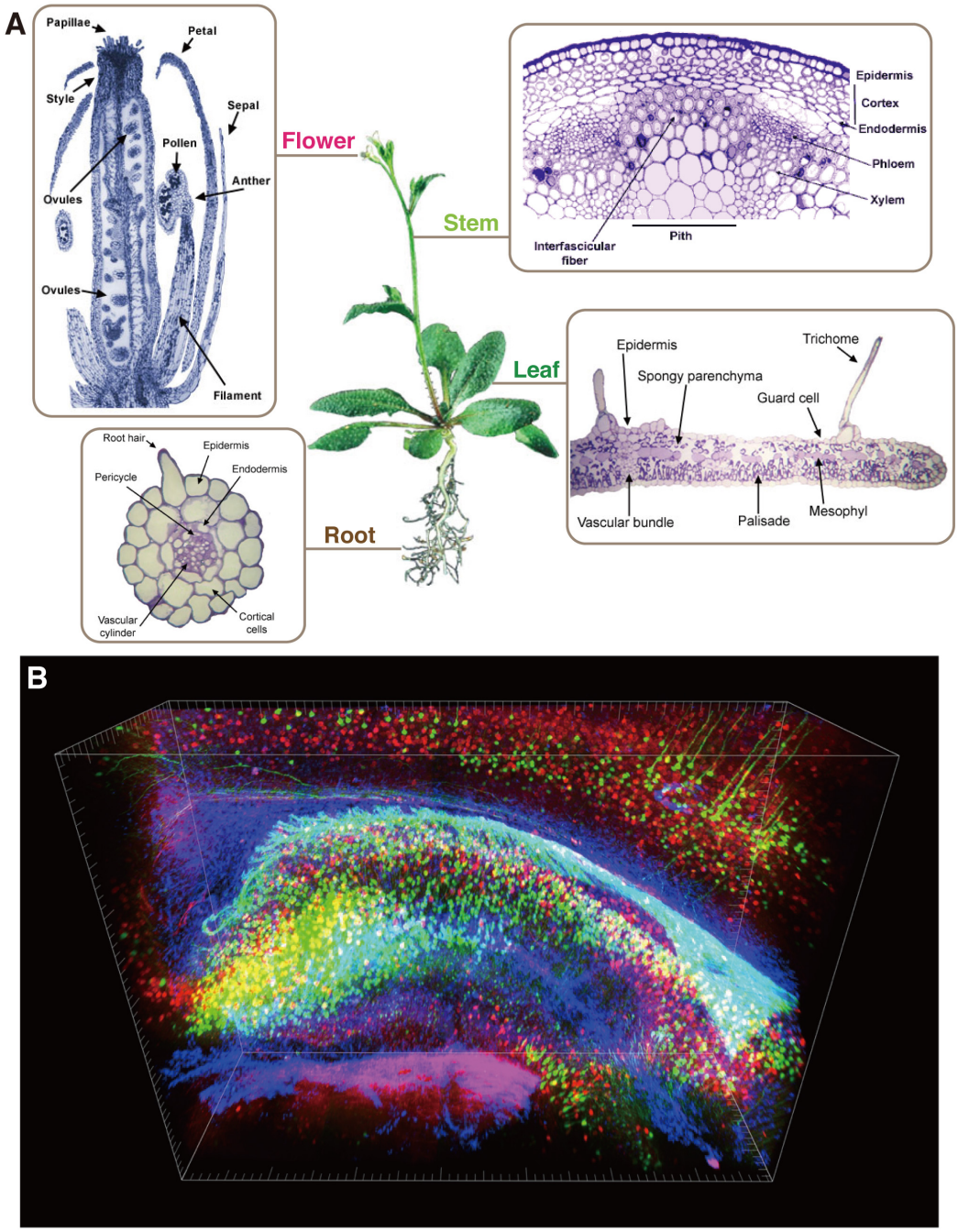

Figure 1. Various cell types in individual organs

(A) The variety of cell types in a dicotyledonous plant is shown in the images of the cross sections of the major organs (flower, stem, leaf, and root) of Arabidopsis. Images are adapted from http://www.ccrc.uga.edu/ ~mao/ultrast/Utext.htm.

(B) Neurons in a mouse brain. Three-dimensional view of stained hippocampus showing fluorescent-expressing neurons (green), connecting interneurons (red) and supporting glia (blue). Adapted from Shen (2013).

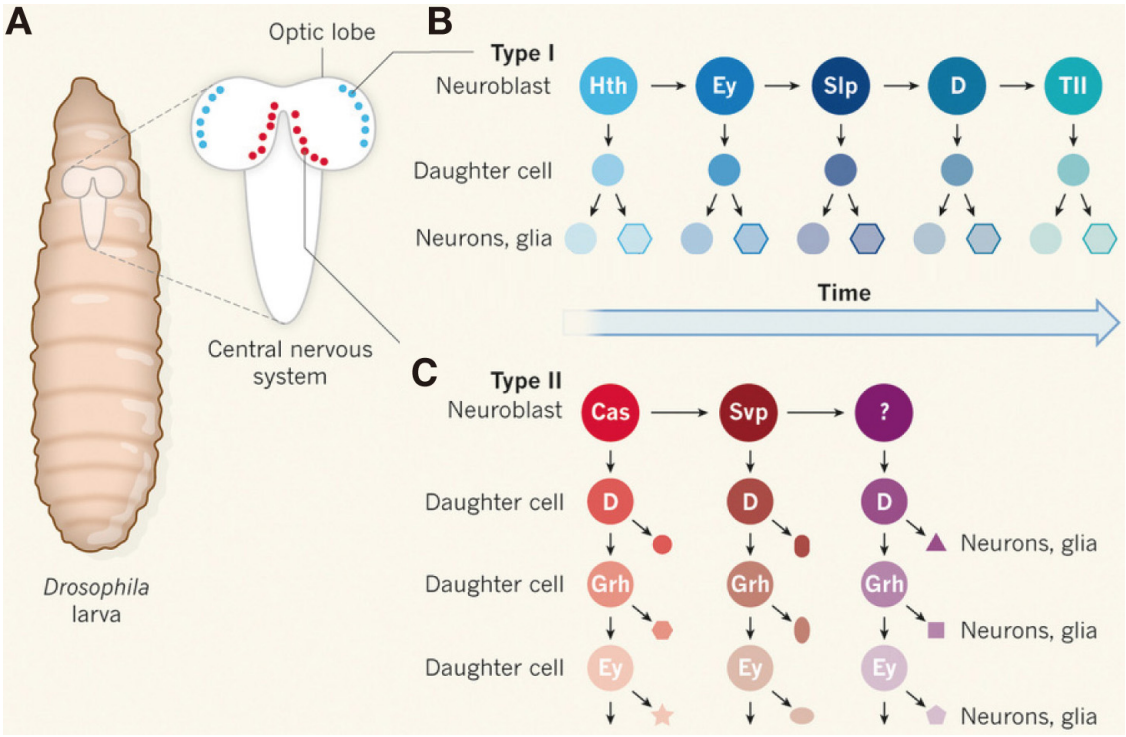

Figure 2. Transcription factors in neural stem cells and daughter cells generate different cell types

(A-C) Neuroblasts (neural stem cells) in the central nervous system of *Drosophila* larvae are divided into type I (which have daughter cells that divide once) and type II (which have daughter cells that divide several times).

(B) The temporal progression of type I neuroblasts is controlled by the expression of a cascade of transcription factors, such as Hth and Ey, which results in generation of different types of neuronal and glial cells.

(C) In type II lineages, separate cascades occur in two main branches: one in the neuroblast itself and one in each daughter branch. This allows for the generation of even greater diversity in cell types originating from a single neuroblast. Adapted from Thor (2013).

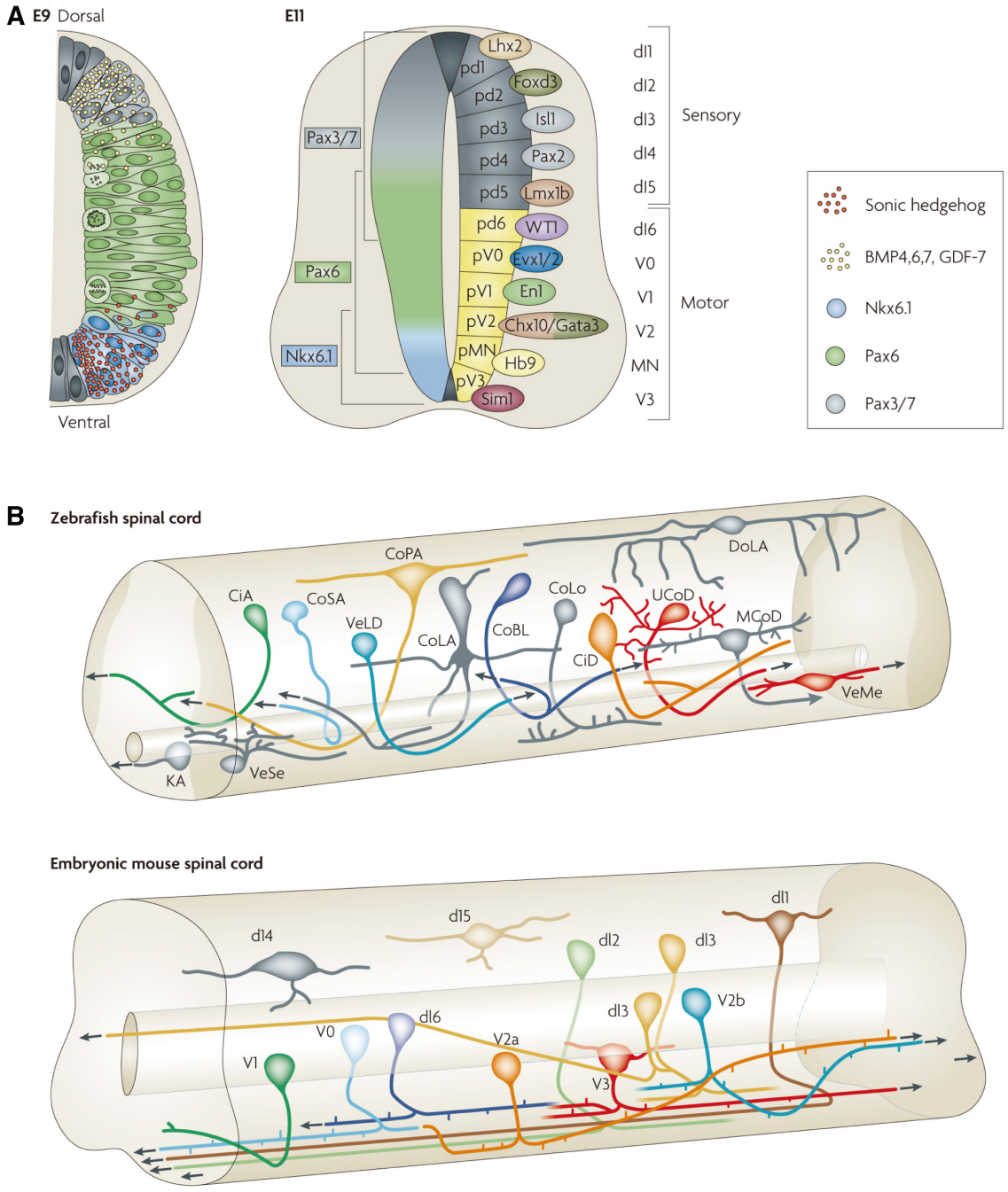

Figure 3. Postmitotic transcription factors and interneurons in the spinal cord

(A) Schematic cross-sections through the developing mouse spinal cord. At embryonic day 9 (E9), a gradient of Sonic hedgehog (red) and bone morphogenetic proteins (BMPs) and growth differentiation factor 7 (GDF-7; yellow) provide instructive positional signals to dividing progenitors. This leads to the restricted activation of patterning factors. At E11, eleven early classes of postmitotic neuron are present in the spinal cord. Some of the postmitotic transcription factors that serve to identify each of the eleven populations are indicated.

(B) Identified spinal interneurons in the embryonic mouse and zebrafish spinal cord. Similar neuronal cell types are present. Adapted from Goulding (2009).

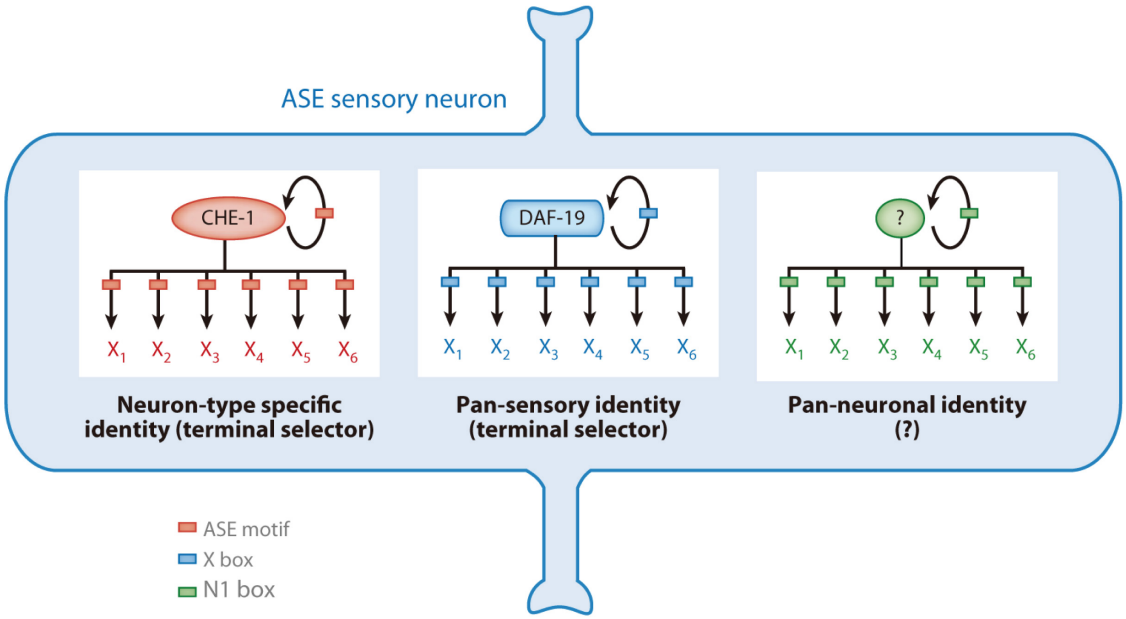

Figure 4. Terminal selectors of neuronal differentiation

Terminal selectors of the C. elegans ciliated gustatory neuron class ASE. A terminal selector CHE-1 controls ASE-specific identity features, and DAF-19 controls expression of the core components of the ciliated structures of the ASE (as well as all other sensory neurons). Adapted from Hobert (2011).

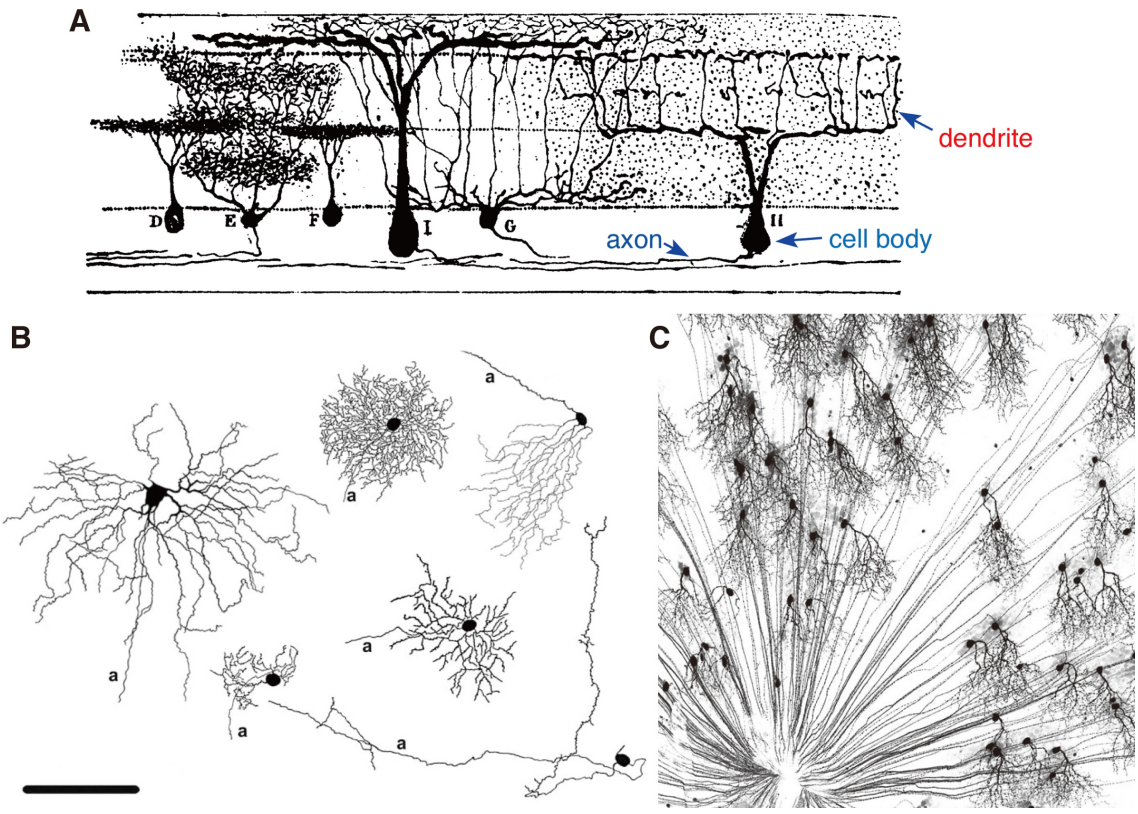

Figure 5. Diverse dendritic branching pattern of retinal ganglion cells

(A and B) Diverse dendritic branching pattern of ganglion cell subtypes in the retina of the spotted lizard (A) and the mouse (B). a, axon. Bar: 100 μm.

(C) Micrograph of a whole-mounted retina. A structurally unique subset of retinal ganglion cells are labeled in this preparation.

Part A, B, and C are adapted from Ramón y Cajal (1911), Volgyi et al. (2009), and Kim et al. (2008), respectively.

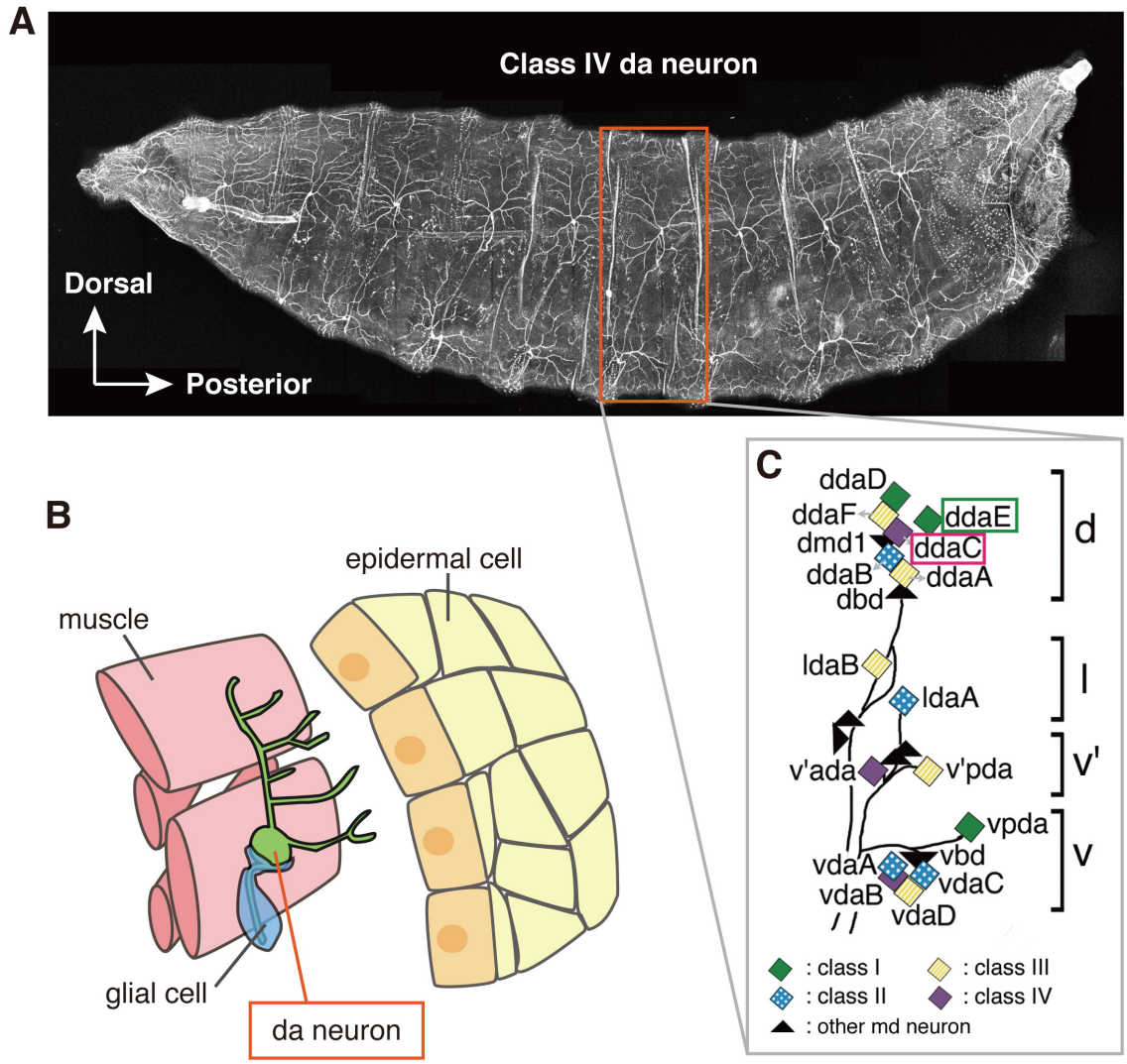

Figure 6. *Drosophila melanogaster* dendritic arborization (da) neurons

(A) A lateral view of a *D. melanogaster* larva with its dendritic arborization neurons labelled with green fluorescent protein. Anterior is left and dorsal is up in this and all subsequent figures. Image courtesy of Dr. Tadao Usui.

(B) A diagram that illustrates spatial arrangements of epidermal cells, muscles, a peripheral glial cell, and a ddaE.

(C) A diagram of positions of multidendritic (md) neurons in an abdominal hemisegment of the *Drosophila* embryonic and larval PNS. Diamonds represent individual dendritic arborization (da) neurons; and triangles, other types of md neurons. Besides all da neurons, only two bipolar dendrite neurons (dbd and vbd) and dmd1 are indicated for simplicity. d, l, v', and v represent dorsal, lateral, ventral prime, and ventral clusters, respectively. Each class of the da neurons is differently colored. Black lines represent fascicles of axons that extend from the neuronal cell bodies. I mainly focused on class I neuron ddaE (green box) and class IV neuron ddaC (magenta box) in the dorsal cluster.

Part B and C are adapted from Yamamoto et al. (2006) and Sugimura et al. (2004), respectively.

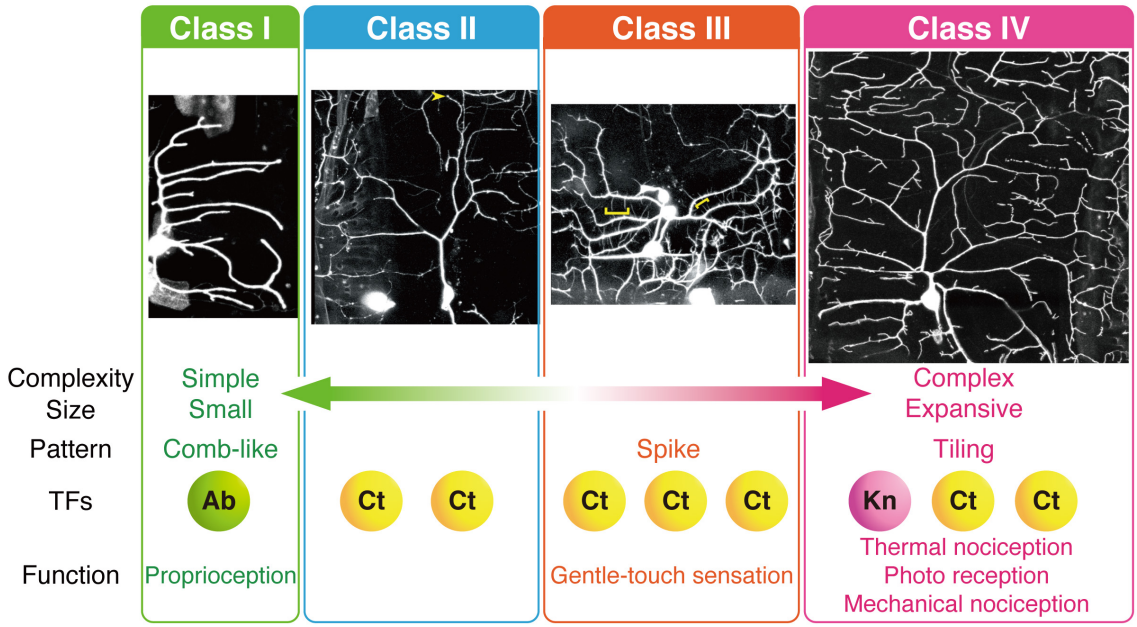

Figure 7. The four classes of da neurons

Dendrite morphologies of class I-IV da neurons, the relative levels of expression of the transcription factors (TFs), Cut (Ct), Abrupt (Ab), and Knot (Kn), in these neurons, and their physiological functions. da neurons are classified into classes I-IV in order of increasing territory size and/or branching complexity. The four classes of da neuron are distinguishable by their class-specific dendritic morphology: dorsal class I neurons have simple comb-like small dendrites, whereas class II neurons have more symmetrically bifurcating dendritic arbors. Class III neurons have numerous spiked protrusions. Class IV neurons develop complicated, expansive, and radial pattern of dendrites. Image courtesy of Dr. Kaoru Sugimura.

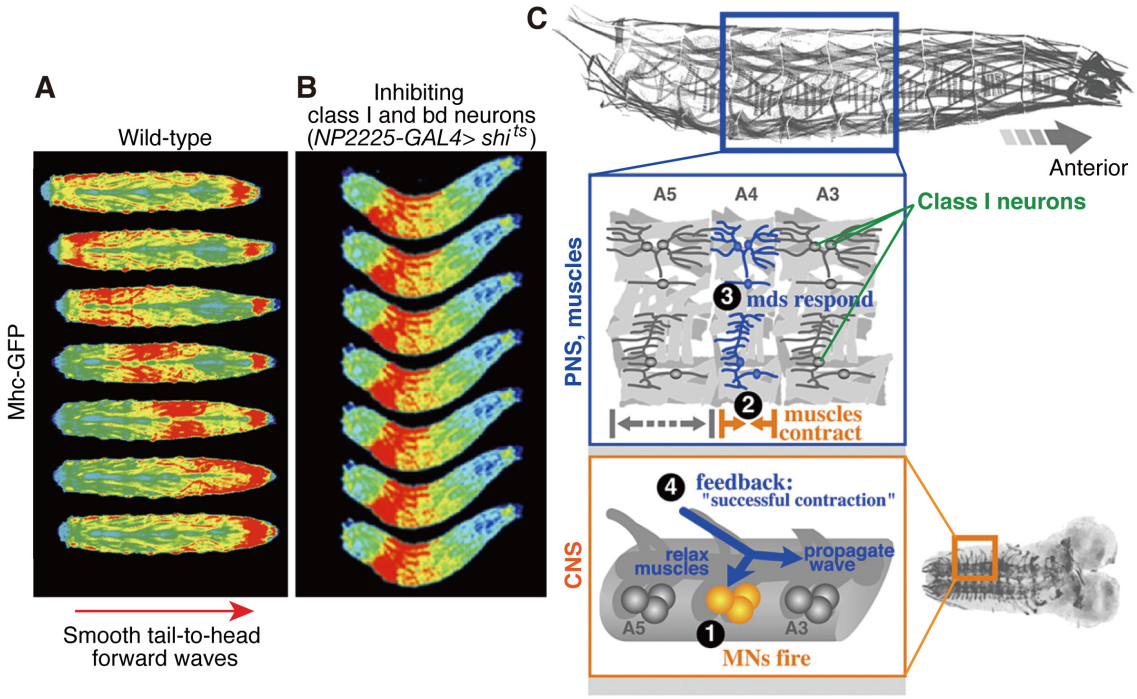

Figure 8. Class I neurons contribute to proprioception

(A and B) By inhibiting subsets of neurons in the PNS, two classes of multidendritic neurons are shown to play a major role in larval crawling.

(A) Wild-type larva with Mhc-GFP labeled muscles, crawling from left to right. A single wave of peristaltic contraction is shown. Images are false-colored: areas of highest muscle contraction and highest GFP-intensity are red, while the most relaxed areas are blue.

(B) Inhibiting just the bipolar dendrite (bd) and class I neurons with *NP2225-Gal4* driving *UAS-shi^{ts}* produces defective crawling with slow, tight waves.

(C) The bipolar dendrites and class I mds send a feedback signal to the CNS that keeps the contraction wave progressing quickly, allowing smooth forward movement. Adapted from Hughes and Thomas (2007).

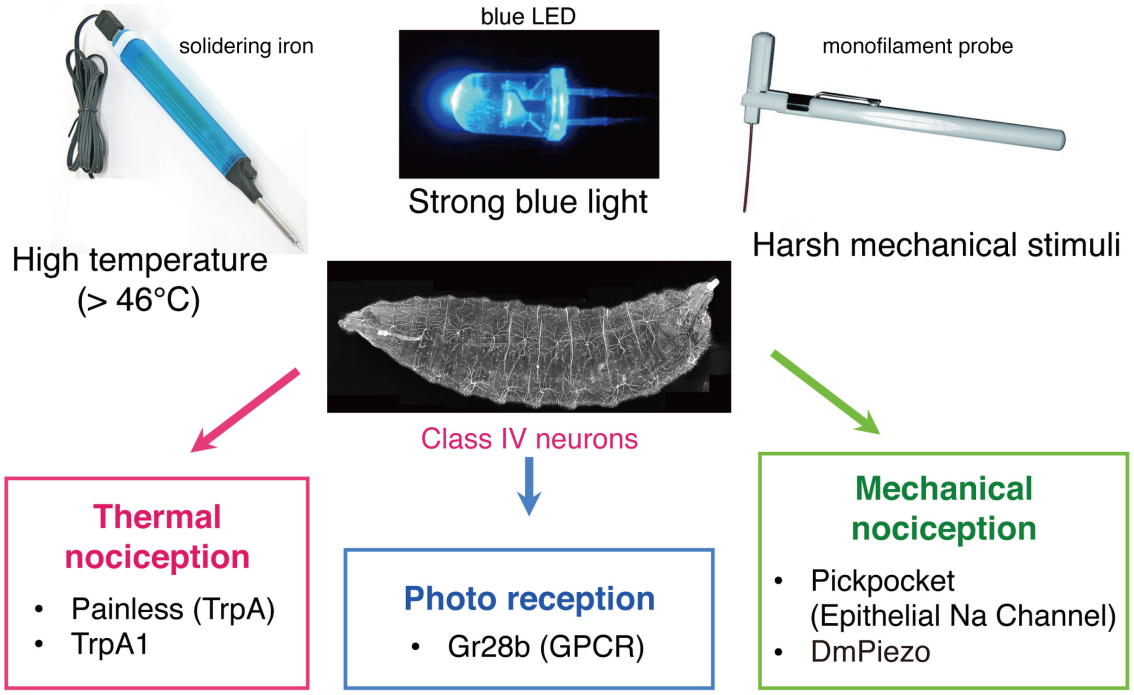

Figure 9. Physiological functions of class IV neurons
Class IV neurons are somatosensory nociceptors and display polymodal responses to three kinds of noxious stimuli (heat, light, and mechanical forces) and provoke specific avoidance behaviors: Noxious thermal and mechanical stimuli induce the corkscrew-like rolling behavior (Hwang et al., 2007; Kim et al., 2012b; Tracey et al., 2003), whereas short-wavelength light inputs elicit the directional shift of locomotion (Xiang et al., 2010). It is shown that these distinct outputs are directed by the information processing of Class IV neurons themselves. Channels involved in the nociceptive behaviors are indicated in boxes. Text and figure courtesy of Dr. Tadao Usui. Images are modified from http://www.donya.jp /item/15078.html; http://www.berchtold-shop.de/en/miscellaneous /608-monofilament.html; http://ledshoppe.com/Product/led/LE1015.htm.

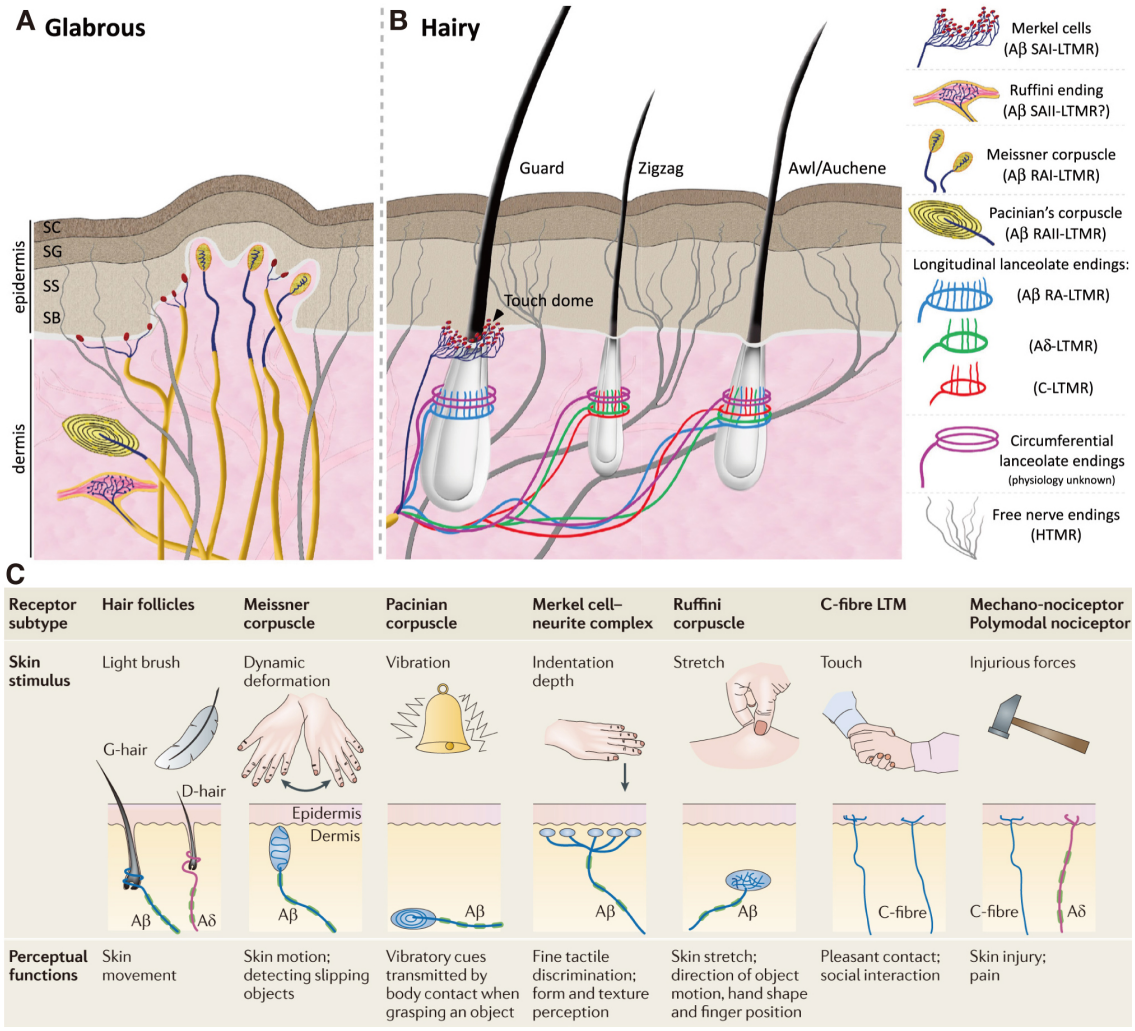

Figure 10. The organization of mechanoreceptors in skin

Innocuous and noxious touch information is processed by both glabrous hairless (A) and hairy (B) skin.

(A) In glabrous skin, innocuous touch is mediated by four types of mechanoreceptors.

(B) In hairy skin, tactile stimuli are transduced through three types of hair follicles. Note stereotyped architectures of the endings. Adapted from Abraira and Ginty (2013) and see more details in it.

(C) Cutaneous mechanosensory neurons differentiate into many functionally distinct subtypes — each of which is thought to transduce specific kinds of mechanical stimuli. This pertains to the detection of innocuous and noxious mechanical information that underlies our senses of touch and pain. Adapted from Delmas et al. (2011).

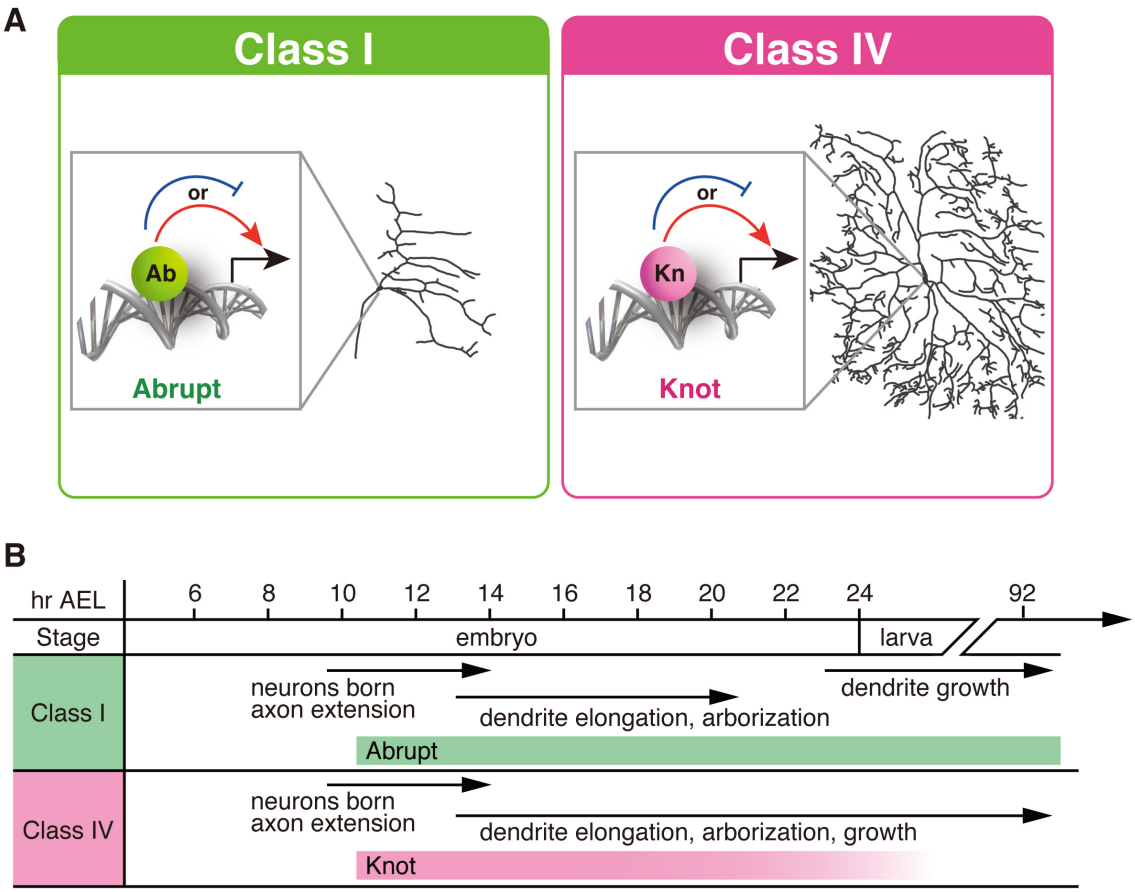

Figure 11. Abrupt and Knot are selectively expressed in class I and IV, respectively

(A) Selective expression of transcription factors (TFs) in class I and class IV da neurons.

(B) Timeline of development of class I and IV da neurons after egg laying (AEL). Adapted from Yamamoto et al. (2006). Class I neurons and class IV neurons employ distinct strategies of dendritic arbor formation. Class I neurons almost cease branching at the end of embryogenesis and keep growing preexisting branches in larvae, while class IV neurons continue to elaborate higher-order branches throughout larval stages. Bars represent the temporal expression profiles of Ab and Kn. Kn was not detected at the 3rd instar wandering larval stage (Shimono et al., 2009). A series of loss- or gain-of-function conditions of Ab or Kn do not dramatically affect the expression of the other respective TF in the embryo, providing no strong evidence for an epistatic relationship between these two TFs (Hattori et al., 2007).

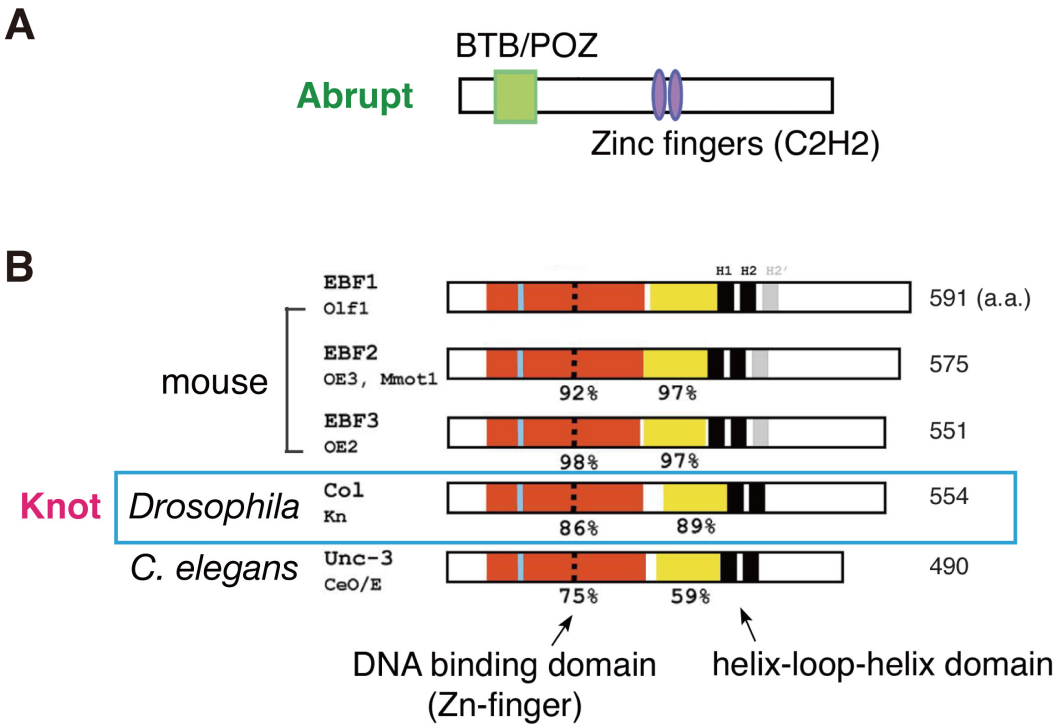

Figure 12. Structures of Abrupt and Knot

(A) Structure of Abrupt. Adapted from Sugimura et al. (2004).

(B) Schematic representation and alignment of representative members of the COE protein family. The DNA-binding domain is in red. A second highly conserved region, whose precise function remains to be established, is shown in yellow. The HLH motif is represented by two separate black boxes. Percentages of identity are given between EBF1 and each other protein. Adapted from Dubois and Vincent (2001).

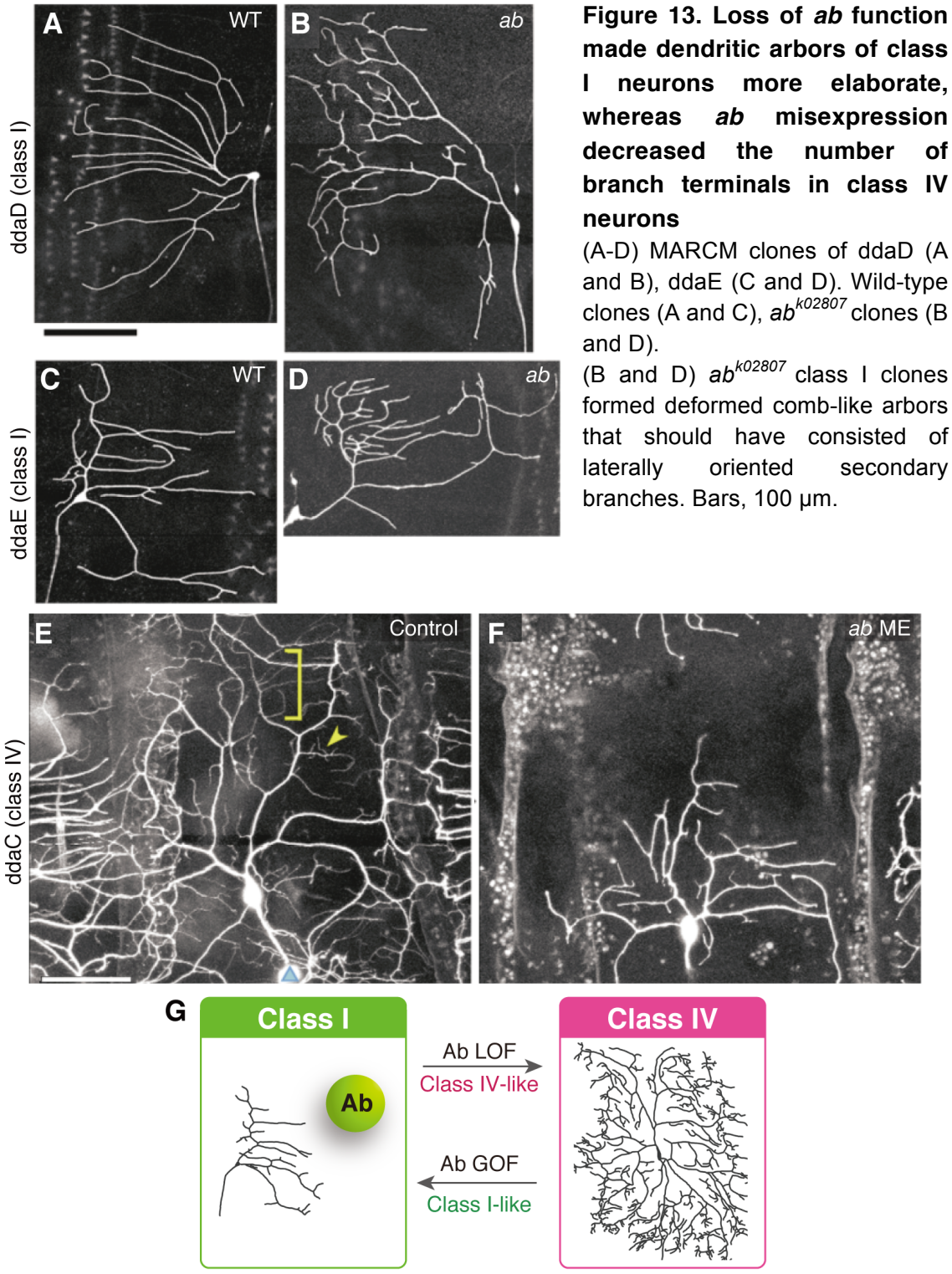

Figure 13. Loss of *ab* function made dendritic arbors of class I neurons more elaborate, whereas *ab* misexpression decreased the number of branch terminals in class IV neurons

(A-D) MARCM clones of ddaD (A and B), ddaE (C and D). Wild-type clones (A and C), ab^{k02807} clones (B and D).

(B and D) ab^{k02807} class I clones formed deformed comb-like arbors that should have consisted of laterally oriented secondary branches. Bars, 100 μm.

(E and F) Single-cell analysis of the class IV neuron, ddaC, by cell ablation. Control ddaC at 62 hr AEL (E) and ddaC at 63 hr AEL that misexpressed *ab* (F). In the middle hemisegment in each panel, all the dorsal da neurons except for ddaC had been ablated at 16-18 hr AEL and the remaining ddaCs were imaged. Bar, 50 μm. Adapted from Sugimura et al. (2004).

(G) Summary of the results. LOF: loss of function. GOF: gain of function.

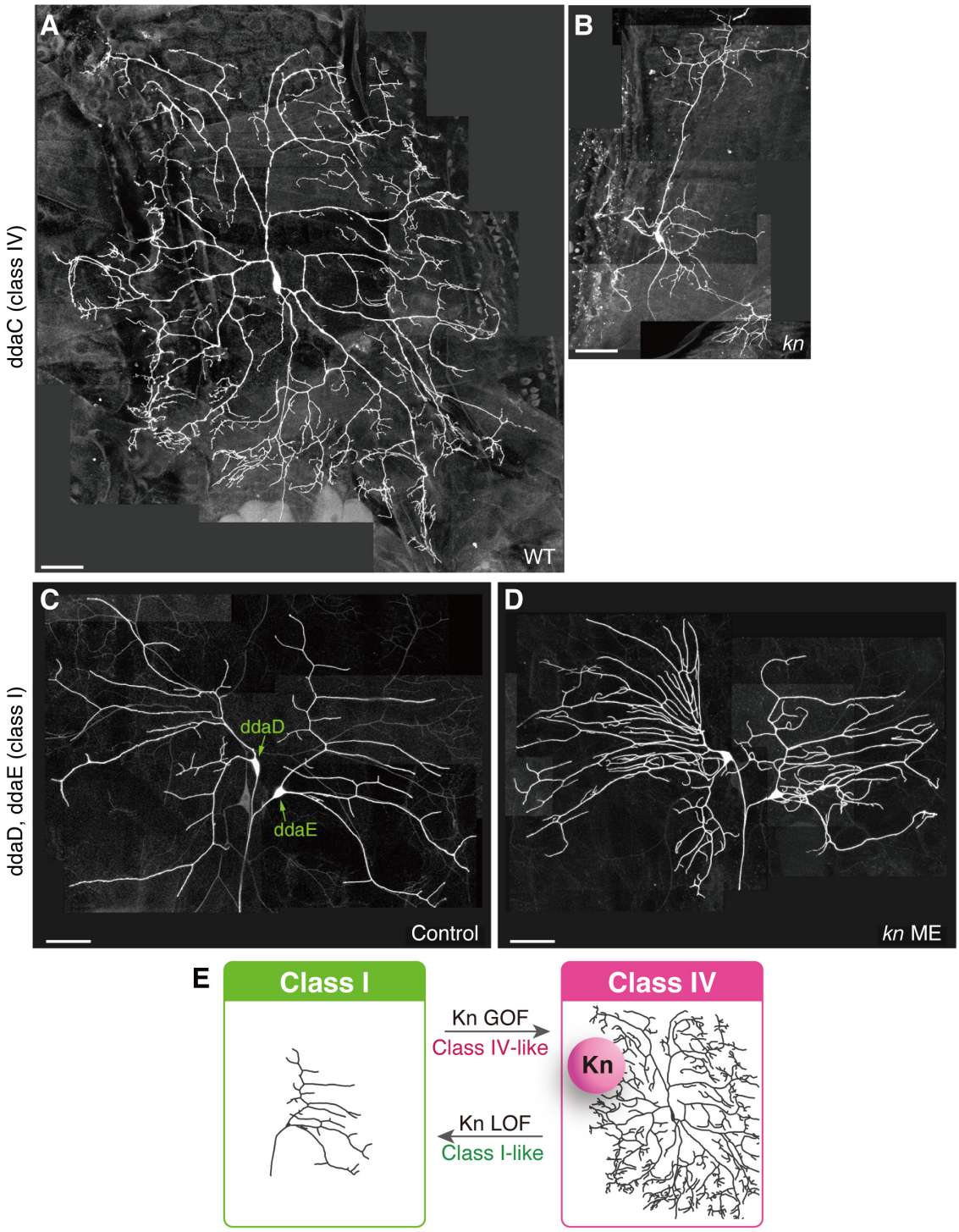

Figure 14. Loss of *kn* function made dendritic arbors of class IV neurons less elaborate and downsized them, whereas *kn* misexpression increased the number of branch terminals in class I neurons

Wild-type (A) and kn^{KN4} MARCM clones (B) of class IV ddaC.

(C and D) Images of control class I da neurons ddaD and ddaE (C) and the neurons that ectopically expressed *kn* (D). Stages of larvae are wandering 3rd instar.

(E) Summary of the results. GOF: gain of function. LOF: loss of function. Bars, 50 μm.

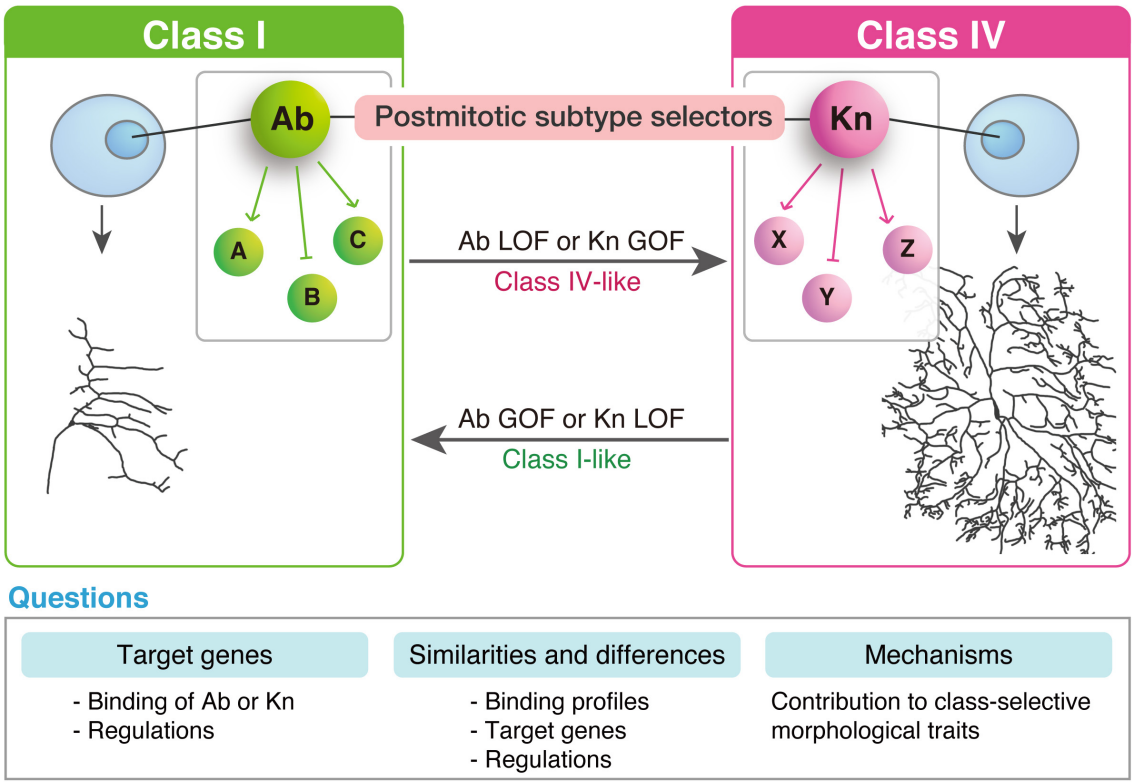

Figure 15. Genome-wide analysis of Abrupt and Knot in vivo

Ab and Kn act as selectors of distinct dendritic arbor morphologies of class I and IV, respectively. I focused on transcriptional programs of Ab and Kn. I searched for target genes of Ab and/or Kn, and compared these two transcriptional programs to better understand how each transcription factor regulates class-selective differentiation and how target genes contribute to producing the class-selective morphological traits.

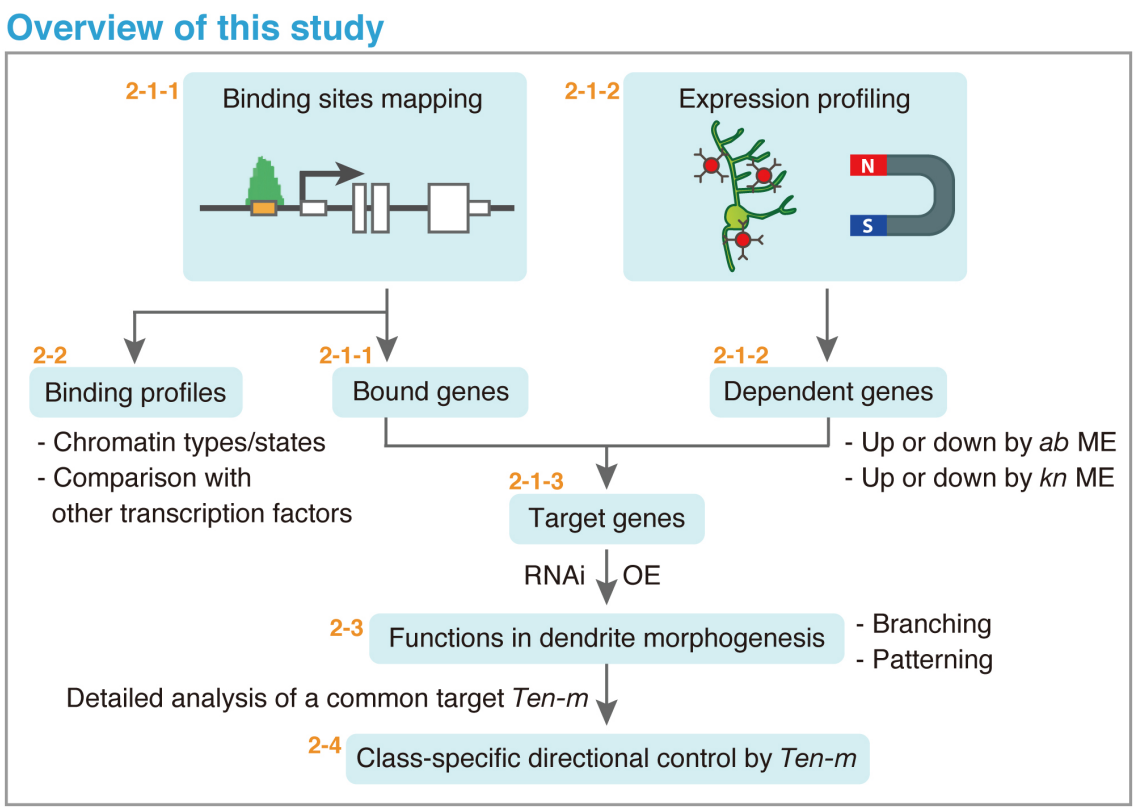

Figure 16. Overview of this study
A schematic diagram of genome-wide analysis of Abrupt and Knot in vivo.
ME: misexpression. OE: overexpression.
Section numbers corresponding to individual steps are indicated.

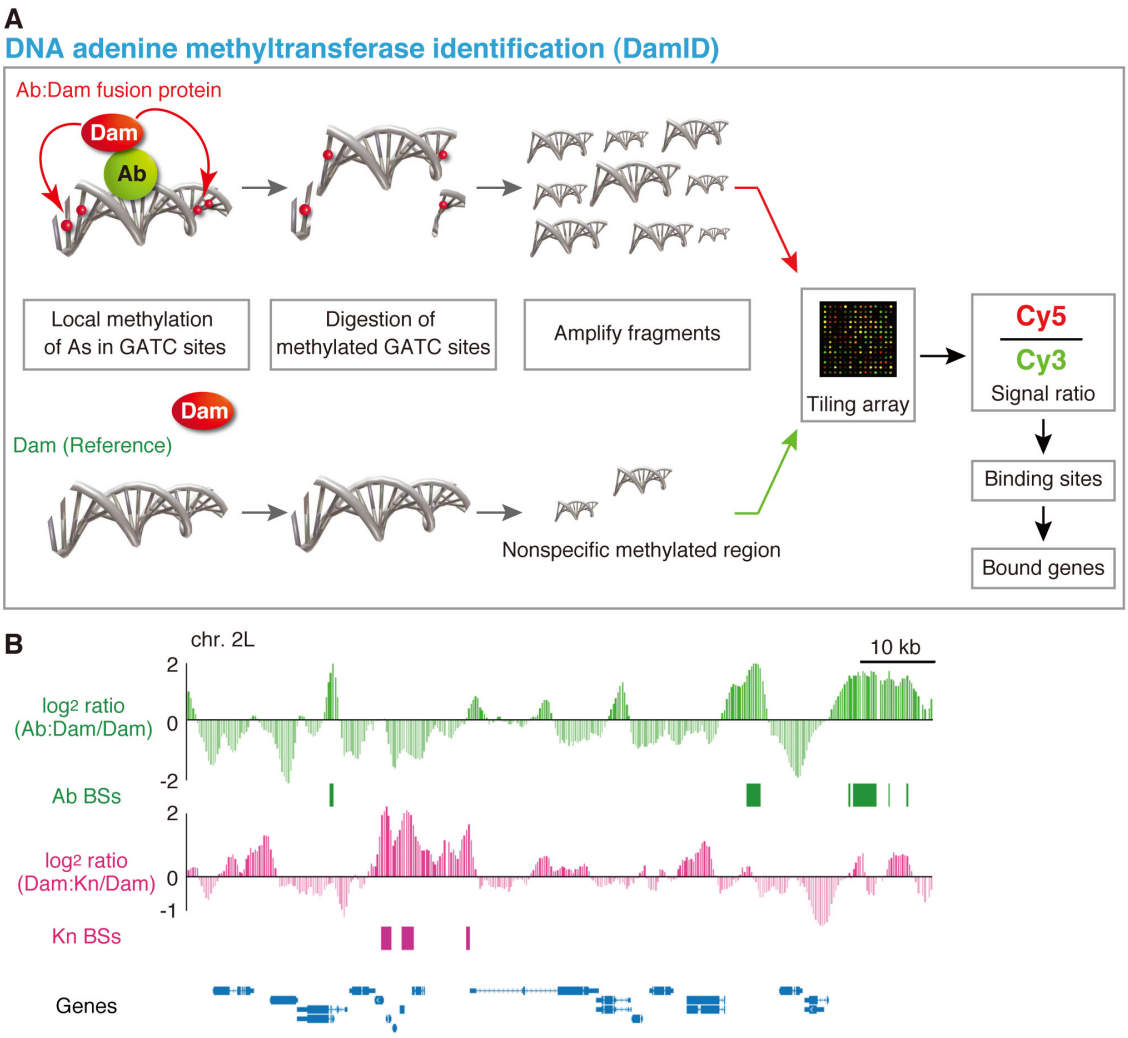

Figure 17. Genome-wide mapping of Ab and Kn binding sites and identification of the target genes

(A) A schematic diagram of the DamID technique. Abrupt or Knot is fused to an Escherichia coli adenine methyltransferase (Dam), and the fusion protein is expressed in vivo. The DNA-binding protein targets the fusion protein to its native binding sites, and the Dam methylates local adenine residues in the sequence GATC. The sequences near the binding site are thereby marked with a unique methylation tag, over approximately 2–5 kilobase pairs (kb). The tagged sequences can be isolated after digestion with a methylation-sensitive restriction enzyme. These digested fragments are amplified and detected on tiling arrays.

(B) Examples of DamID data of Ab (green) and Kn (magenta). The 393-494 kb region of chromosome 2L is shown. Bar heights are proportional to averages of standardized log2-transformed ratios of intensities (see details 4-3. Analysis of DamID data and Figure 18). Boxes indicate binding sites of each TF (Ab BS and Kn BS).

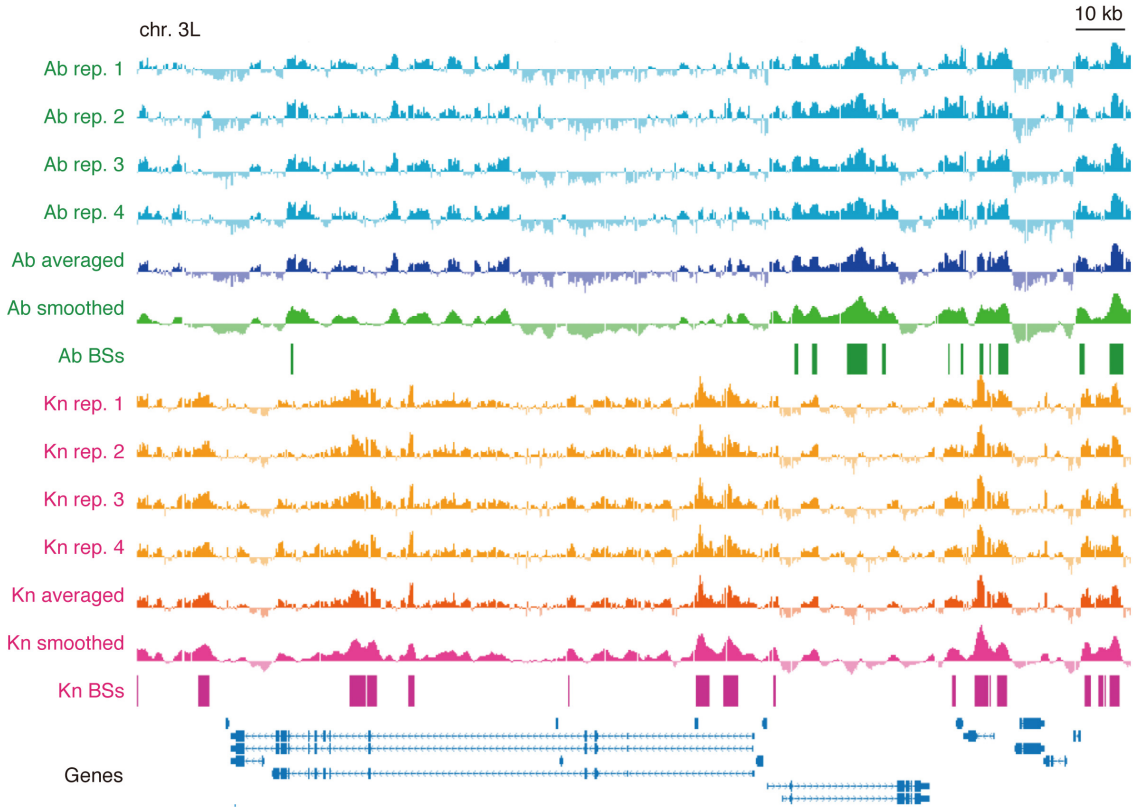

Figure 18. DamID data

DamID profiles of Ab and Kn in the 415-618 kb region of chromosome 3L. Shown from the top are standardized log2-ratios of four biological replicates, averaged log2-ratios, smoothened log2-ratios, binding sites, and genes.

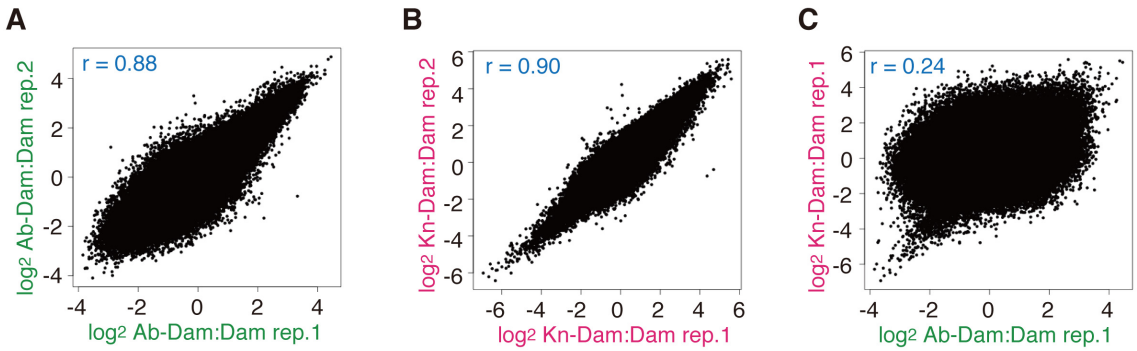

Figure 19. Correlations of the Ab or Kn replicates

Pairwise plots of standardized log2-ratios at individual spots of Ab replicate 1 vs. Ab replicate 2 (A), Kn replicate 1 vs. Kn replicate 2 (B), Ab replicate 1 vs. Kn replicate 1 (C). Each correlation coefficient is indicated.

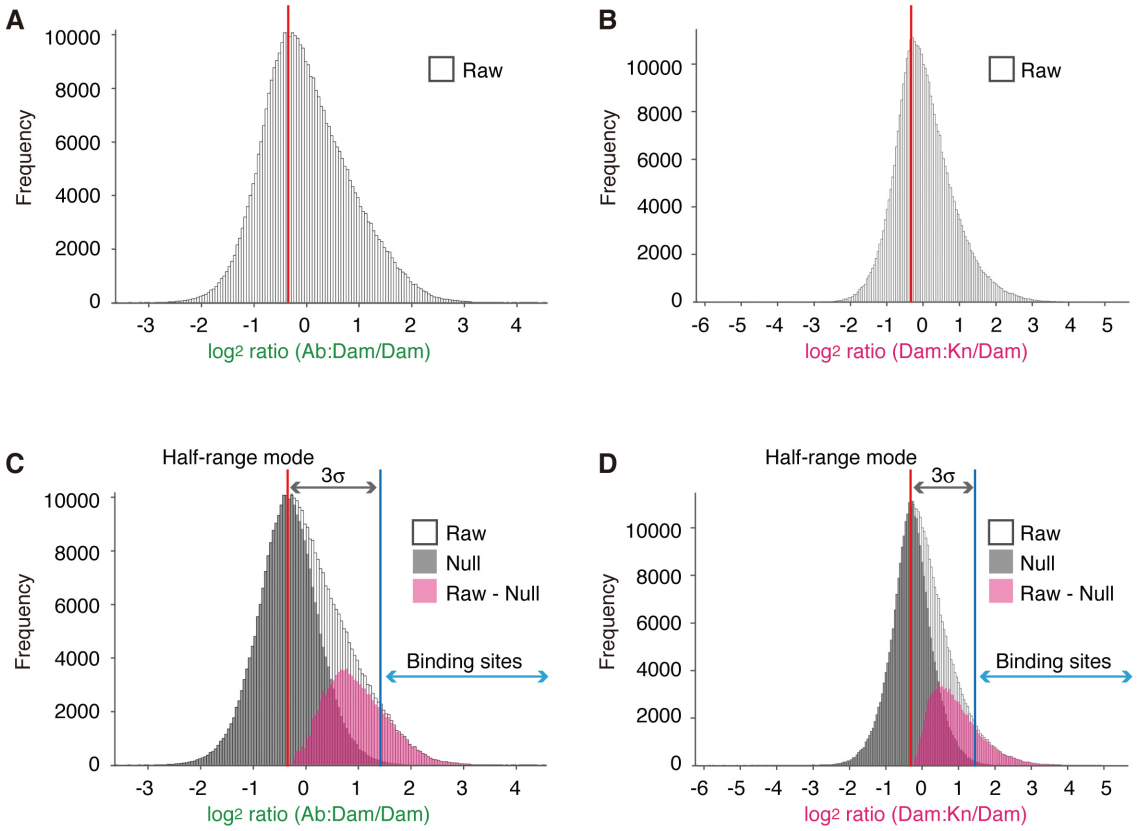

Figure 20. Distributions of averaged log2-ratios of my DamID analyses and definition of binding sites

(A and B) Raw distributions of averaged log2-ratios of Ab (A) and Kn (B).

(C and D) Binding sites were defined by subtracting null distributions (Null) from the raw distributions (Raw). Red lines indicate the modes; and blue lines, 3σ of the null distribution (threshold values). Binding sites (BSs) were defined as follows: the distributions of the smoothed ratios were skewed towards positive values (raw distributions or "Raw"). All statistics falling below the mode (red lines) were used to estimate the left side of the null distribution (Schwartz et al., 2006); then the full null distribution was obtained by reflecting the left side of the null distribution onto the right side of the mode (van Steensel et al., 2003). The null distribution was subtracted from the raw distribution ("Raw – Null" in C and D) and threshold values were set as 3σ of the null distribution (blue lines in C and D). The regions with signal ratios above the thresholds were defined as BSs. Consequently, only 0.15% of estimated noise was included in the BSs.

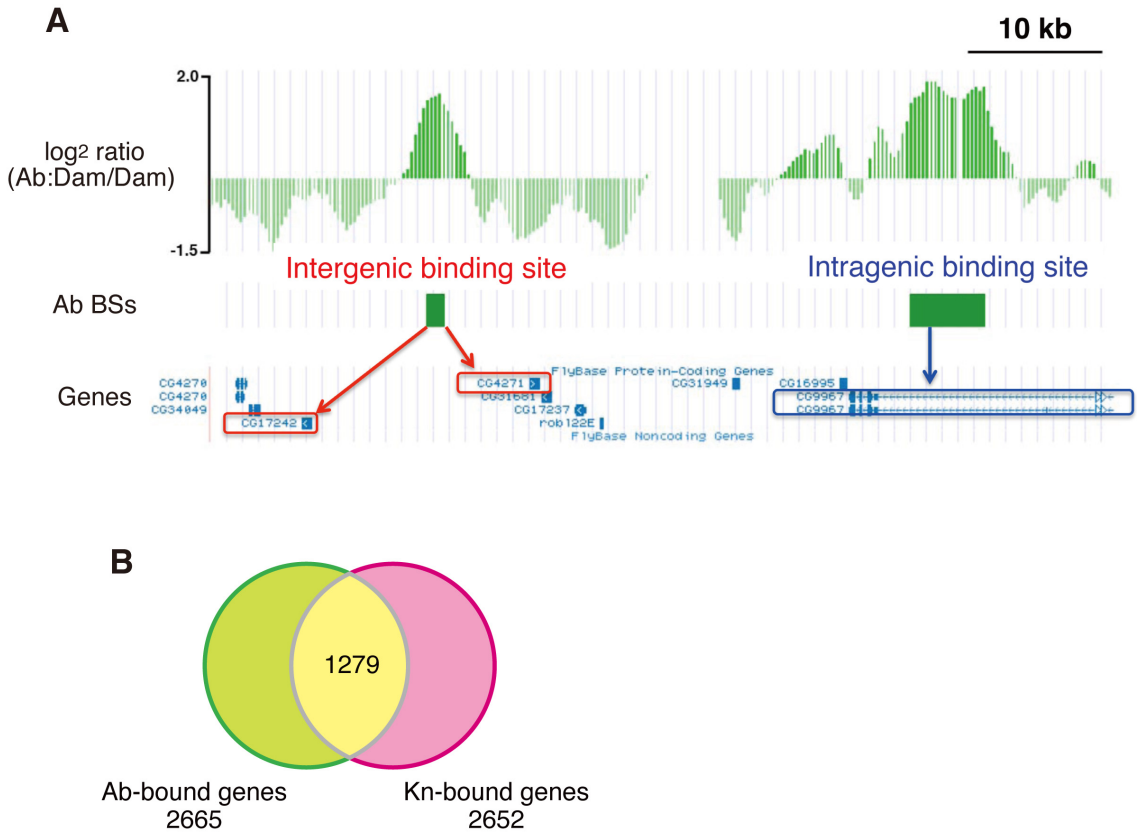

Figure 21. Definition of bound genes and the overlap between the Ab- and Kn-bound genes

(A) Definition of bound genes. If a binding site is located between two genes, I chose both as bound genes. Genes containing binding sites inside were also chosen. I did not set a limit on the distance of the gene from the BS. This was because previous studies on cis-regulatory elements show that the distance from BSs of TFs to their target genes is quite variable (Haeussler and Joly, 2011).

(B) Venn diagram showing the overlap between the bound genes of the TFs.

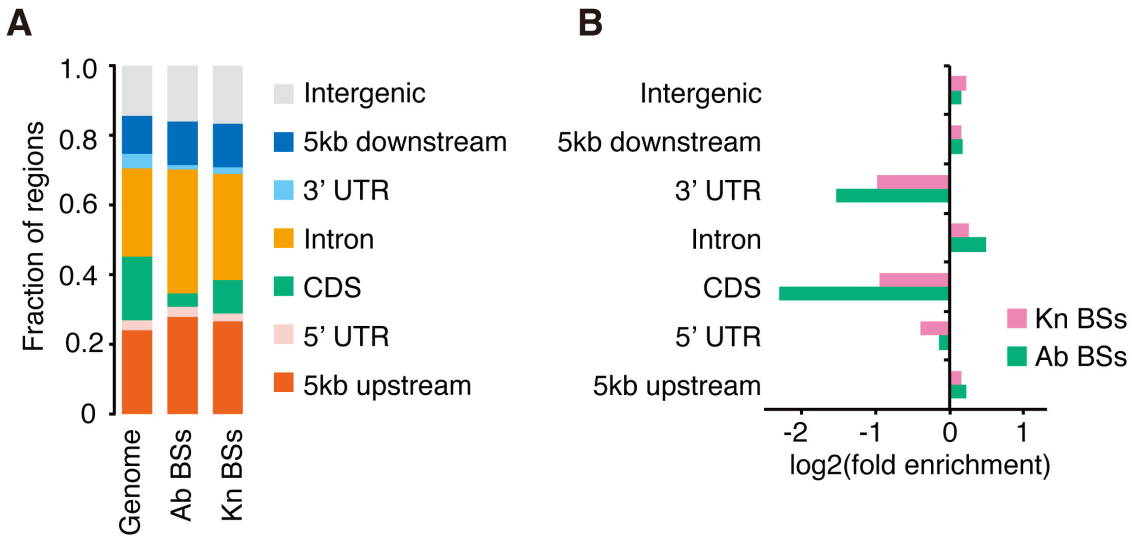

Figure 22. Distributions of the BSs in the *Drosophila* genome, classified into seven regions

Shown are fractions of BSs in individual regions (A) and enrichments/depletions of individual regions in the Ab or Kn BSs relative to those regions in the genome (B).
UTR: untranslated region; CDS: coding sequence.

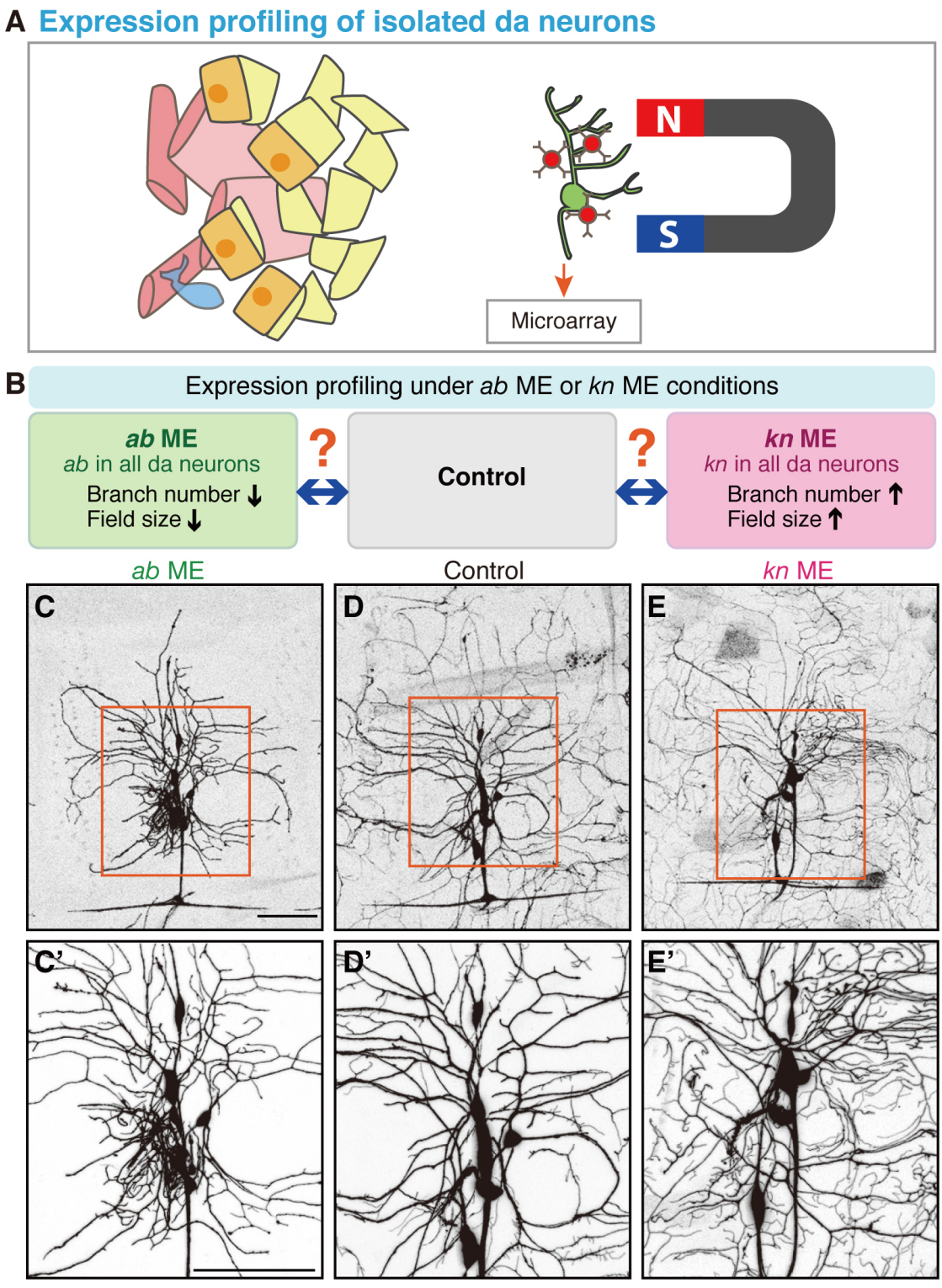

Figure 23. Expression profiling of isolated da neurons under ab or kn misexpression

(A-B) A schematic diagram of the expression profiling of isolated da neurons under *ab* or *kn* ectopic expression in all classes of da neurons (designated as misexpression or ME for

simplicity). After dissociating larval body walls, mCD8:GFP-expressing da neurons were isolated by using anti-CD8 antibody-coated magnetic beads and RNA was prepared.
(C-E') Effects of *ab* or *kn* ME on dendrite arbor formation. Dendritic arbors of all da neurons became downsized and simplified in the case of *ab* ME (Sugimura et al., 2004), or more complicated with *kn* ME (Hattori et al., 2007), than the control arbor (C and C'). Images of dorsal clusters of 3rd instar larvae of *+/GAL4$^{21-7}$ UAS-mCD8:GFP* (C and C'; control), *+/ GAL4$^{21-7}$ UAS-mCD8:GFP; UAS-abL/+* (D and D'; *ab* ME), and *UAS-knL:HA/GAL4$^{21-7}$ UAS-mCD8:GFP* (E and E'; *kn* ME). C'-E' are high-power images of boxed areas of C-E. Bars, 100 μm.

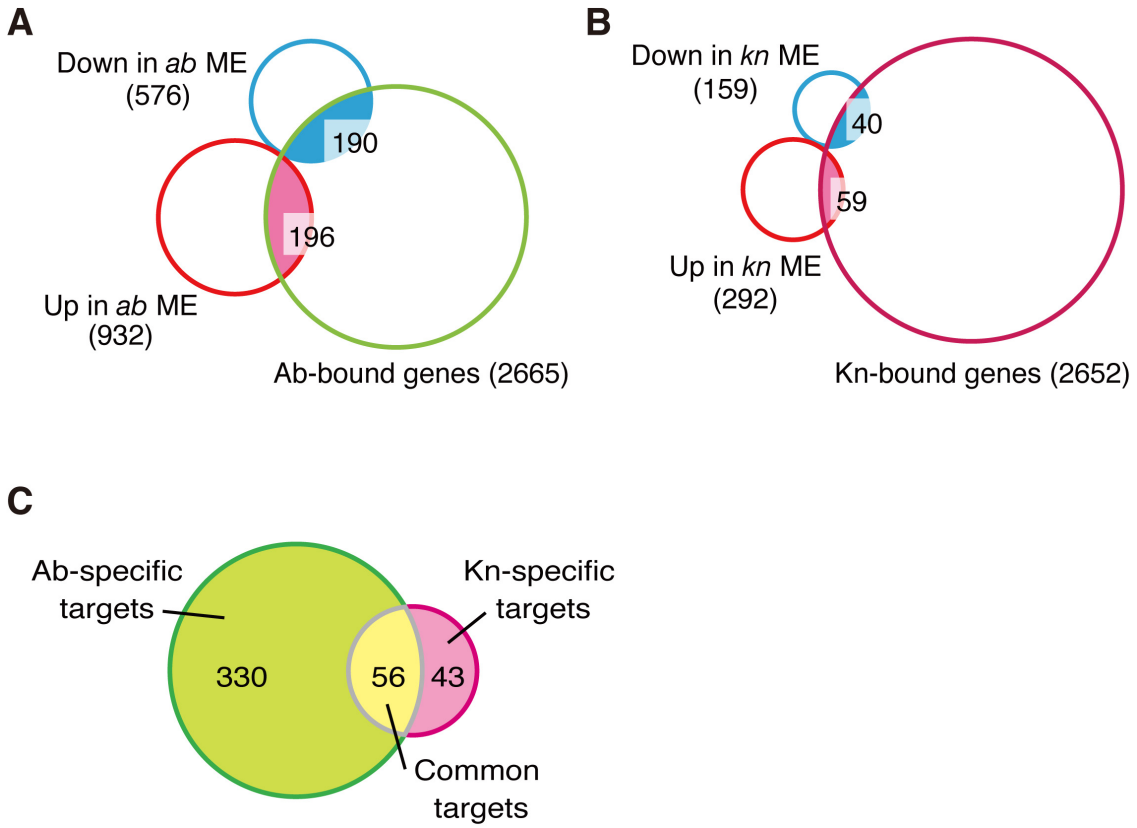

Figure 24. Identification of the target genes

(A and B) Venn diagrams showing the overlaps between the TF-bound genes and TF-dependent genes that were either up-regulated (Up) or down-regulated (Down) by *ab* ME (A) or *kn* ME (B).

(C) Intersection of the dual genome-wide profiling defined 386 Ab target genes (196+190 in "A") and 99 Kn target genes (59+40 in "B"), out of which 56 genes are common. Note my designations of Ab-specific targets, Kn-specific targets, and common targets. The Ab targets and the Kn targets comprise just 26% and 22%, respectively, of the TF-dependent genes (386/1508 and 99/451, respectively). Such small or even smaller overlaps in the dual genome-wide profiling (the binding and the expression) have been documented in studies of Foxp3 and Ascl1 in mice (Castro et al., 2011; Zheng et al., 2007).

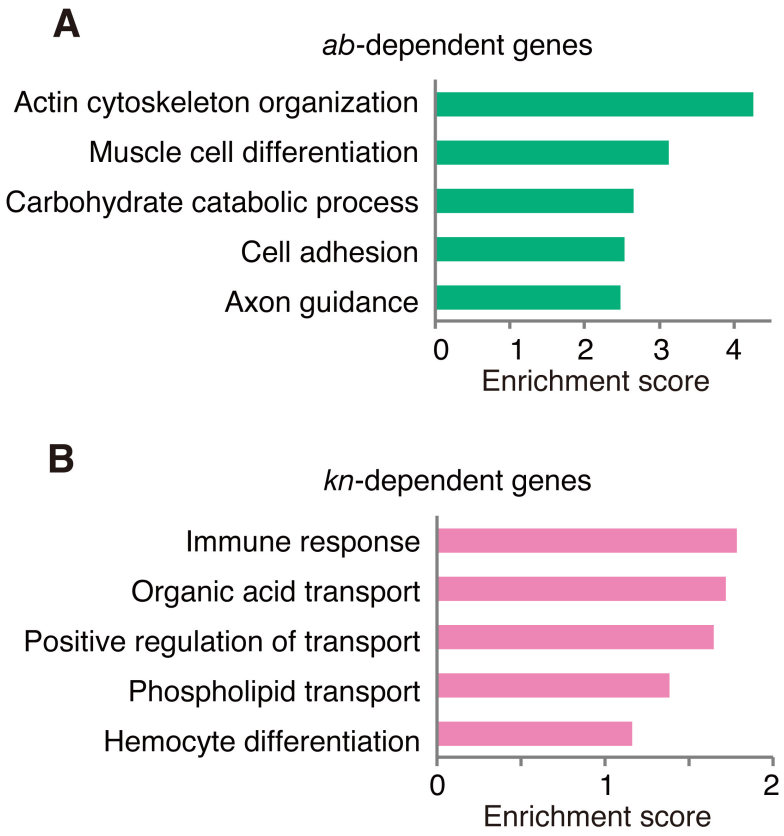

Figure 25. GO clusters enriched in Ab- or Kn-dependent genes
The top five gene ontology (GO) clusters enriched in Ab- (A) or Kn-dependent genes (B) in biological process category by enrichment score.

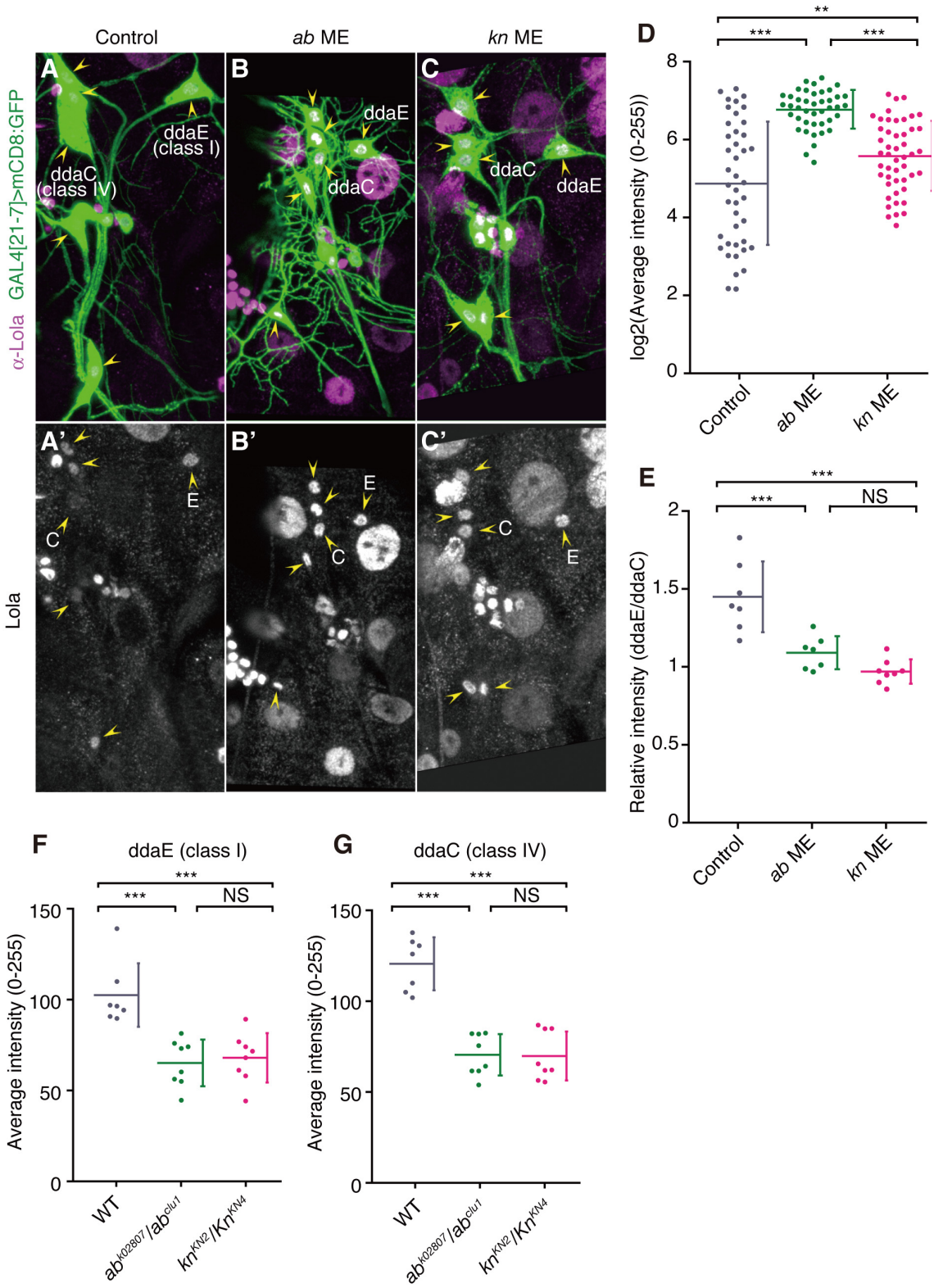

Figure 26. Lola levels under ME or loss of function of *ab* or *kn*

(A-E) Elevated antibody staining for the product of a common target gene *lola* under *ab* ME and *kn* ME conditions. Representative images of the staining in the control (A, A'), *ab* ME (B,

B'), and *kn* ME (C, C') da neurons in wandering larvae. Images of the marker GFP (green in A, B, and C) and Lola (magenta in A, B, and C; A', B', and C'). Nuclei and cell bodies of da neurons are indicated by yellow arrowheads. *ab* ME downsizes dendritic arbors of class II-IV da neurons (Li et al., 2004; Sugimura et al., 2004), increasing the density of branches in the region proximal to the cell bodies (see Figure 23C and 23C').

(D) The elevation of the Lola signal was validated by statistical analysis of log2-transformed signal intensities of immunostaining. ** $P < 0.01$, *** $P < 0.001$ (one-way ANOVA and HSD *post-hoc* test). The distribution of the intensity was broader in the control neurons than in the ME neurons, and I wondered whether this might be due to differential expression of Lola between the da classes.

(E) In fact, the Lola signal in class IV ddaC was significantly weaker than in the class I ddaE control, as shown by the ratios of signal intensity of ddaE to that of ddaC in the same hemisegment.

(F-G) The Lola signal of class I ddaE (F) or class IV ddaC (G) in *ab* or *kn* mutants was significantly weaker than that in the wild-type embryos. ** $P < 0.01$, *** $P < 0.001$ (one-way ANOVA and HSD *post-hoc* test). The wild-type, ab^{k02807}/ab^{clu1} or kn^{KN2}/kn^{KN4} embryos were stained for Lola and a pan-neuronal marker Elav. The level of Lola, but not Elav, was reduced in the mutants (data not shown).

Actual P values are as follows:

(D) < 0.0001 (Cont. vs. *ab* ME), 0.0071 (Cont. vs. *kn* ME), and < 0.0001 (*ab* ME vs. Kn ME)

(E) 0.0007 (Cont. vs. *ab* ME), < .0001 (Cont. vs. *kn* ME), and 0.283 (*ab* ME vs. *kn* ME)

(F) 0.0002 (WT vs. *ab*), 0.0005 (WT vs. *kn*), and 0.9219 (*ab* vs. *kn*)

(G) < 0.0001 (WT vs. *ab*), < 0.0001 (WT vs. *kn*), and 0.9944 (*ab* vs. *kn*)

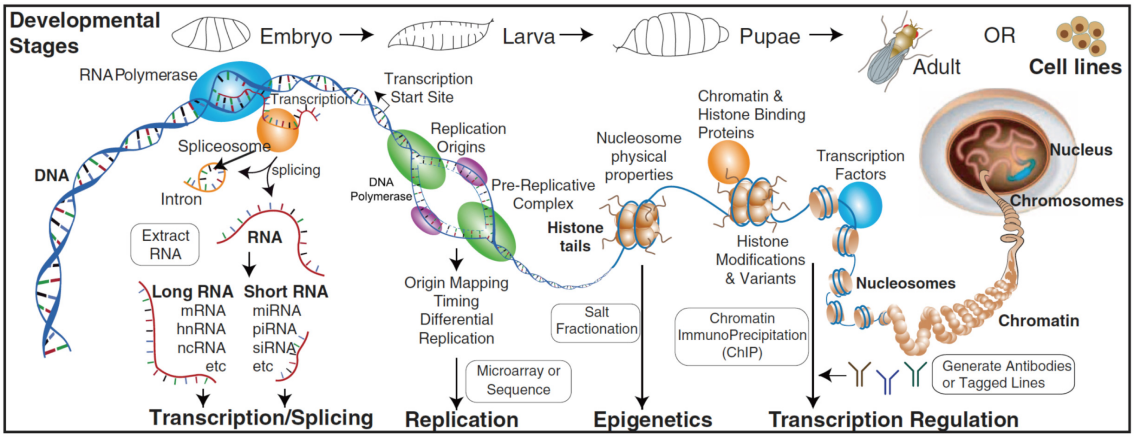

- The model organism Encyclopedia of DNA Elements (modENCODE) project
- More than 700 data sets (RNA-seq, ChIP-chip/seq, tiling array, genomic DNA sequencing)
- Chromatin signatures characteristic of functional elements

Figure 27. Overview of *Drosophila* modENCODE data sets

To gain insight into how genomic information is translated into cellular and developmental programs, the *Drosophila* model organism Encyclopedia of DNA Elements (modENCODE) project is comprehensively mapping of chromatin features such as transcripts, histone modifications, and transcription factors across a developmental time course and in multiple cell lines. Adapted from Roy et al. (2010).

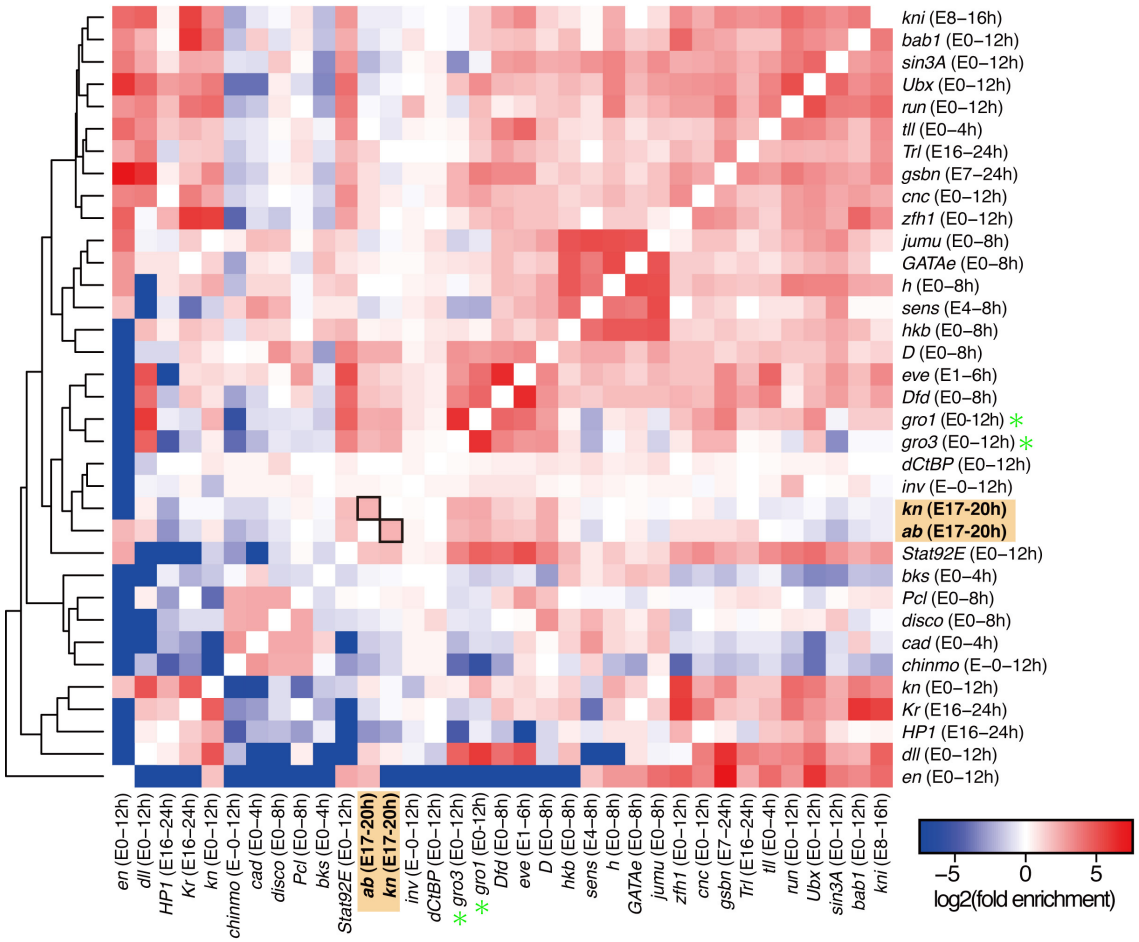

Figure 28. Overlaps of the Ab- or Kn-binding sites

Pairwise comparisons of HOT-subtracted BSs of TFs are indicated (HOT: high occupancy target regions or hotspots). Enrichments/depletions are color-coded by fold enrichment. The data sets are from the modENCODE consortium, except for the two of this study (orange boxes) that are located close-by in this clustering (highlighted by black frames; the correlation index of Ab with Kn was 2.2). *gro1* and *gro3* are technical replicates (green asterisks).

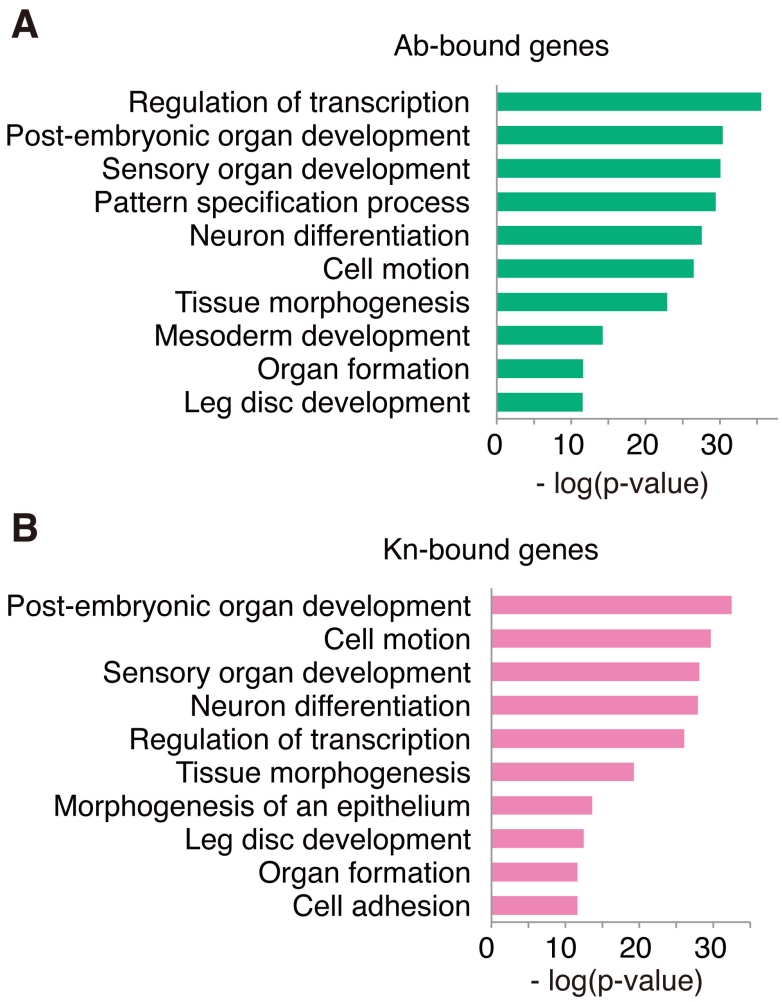

Figure 29. GO clusters enriched in Ab- or Kn-bound genes

The top ten gene ontology (GO) clusters enriched in Ab- (A) or Kn-bound genes (B) in biological process categories, ranked by p-value. Each GO cluster was represented by one GO term in the cluster.

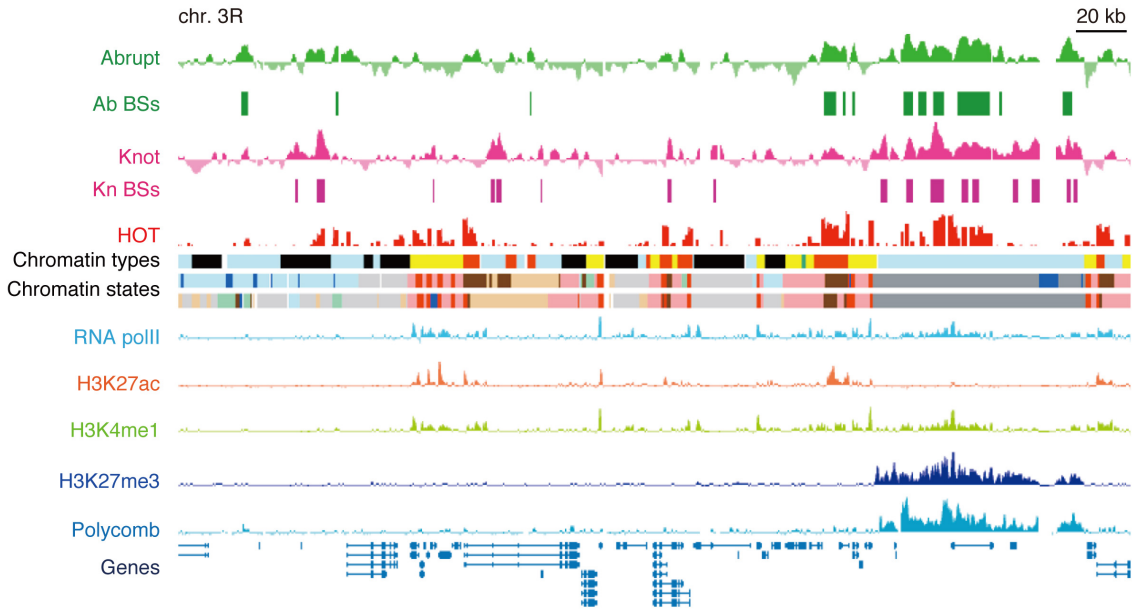

Figure 30. Binding profiles of Ab or Kn with chromatin features

Examples of DamID profiles of Ab or Kn, distributions of Ab BSs, Kn BSs, and HOT regions (Negre et al., 2011), chromatin types (Filion et al., 2010), chromatin states (Kharchenko et al., 2010) in BG3 cells (upper track) and those in S2 cells (lower track), and distributions of four chromatin marks (Negre et al., 2011) and Polycomb (Kwong et al., 2008) at embryonic stage. The 501-1002 kb region of chromosome 3R is shown.

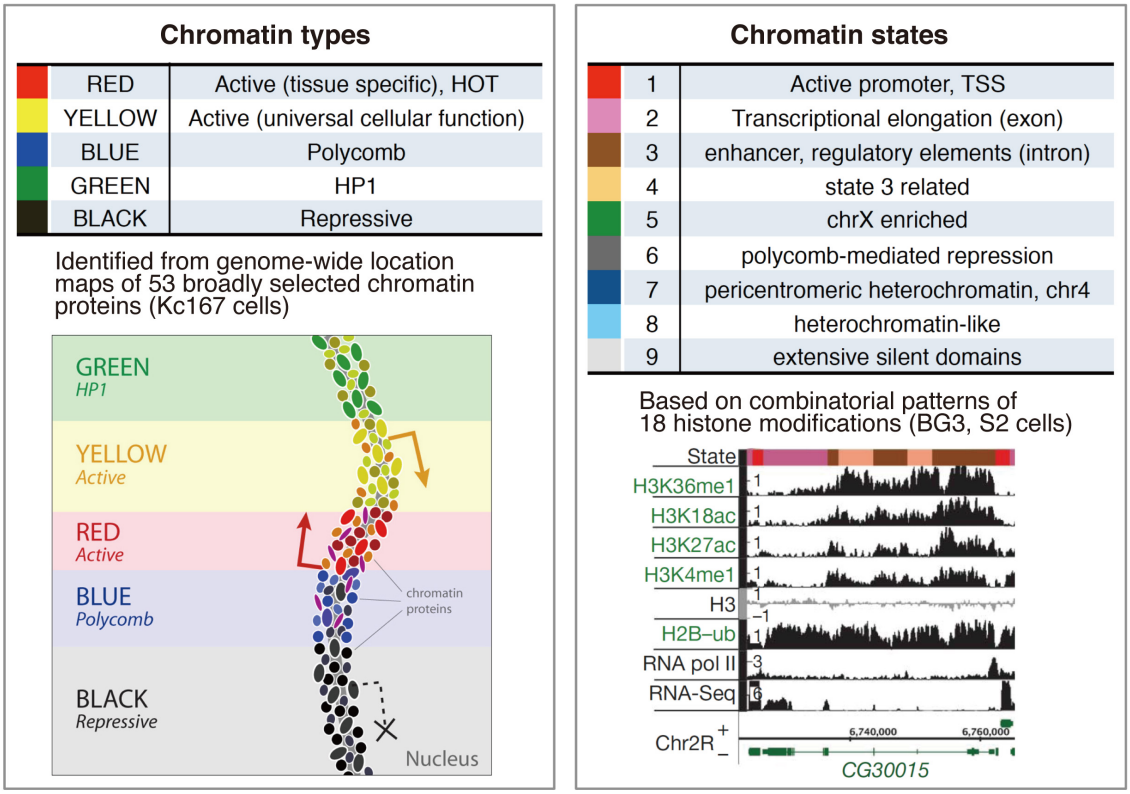

Figure 31. Chromatin types and states

Chromatin features of the *Drosophila* genome have been classified into five “chromatin types” defined by DamID analysis (Filion et al., 2010) or nine “chromatin states” defined by ChIP-chip (Kharchenko et al., 2010). Adapted from Filion et al. (2010); Kharchenko et al. (2010).

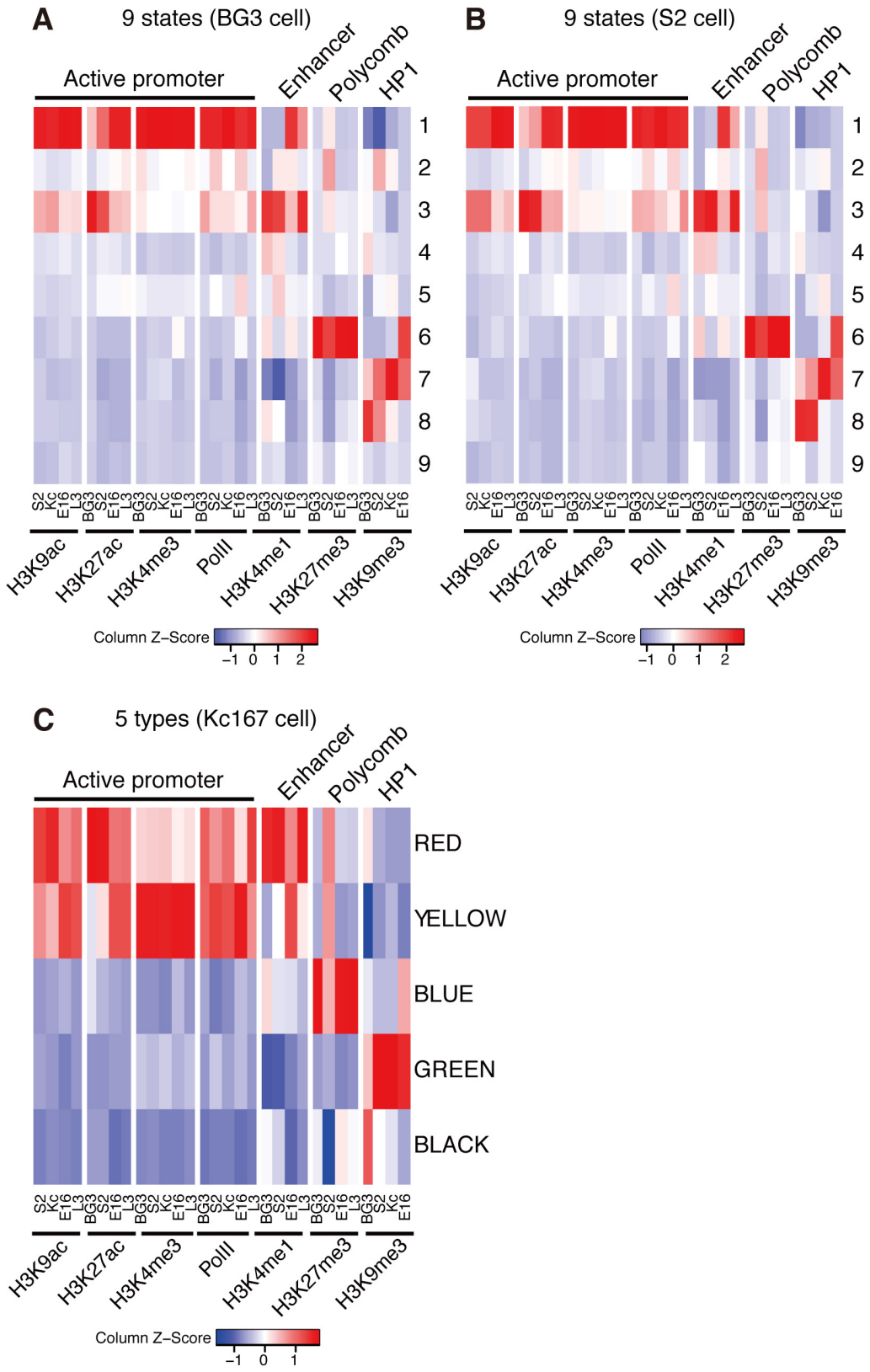

Figure 32. Chromatin features in whole animals (E16 and L3) and in cultured cell lines (BG3 and S2)

I confirmed that the combinatorial patterns of enrichments or paucities of the markers (such as those shown in Figure 30) are basically conserved among the cell lines, embryos that I used for DamID, and third-instar larvae from which I isolated da neurons for the expression profiling. One caveat of this result is that the chromatin types/states are defined on the basis of data sets of cultured cell lines, so it would be ideal to obtain neuronal class-specific data sets and respective chromatin landscapes for each class. Nine chromatin states were defined on the basis of data sets of the BG3 cell line, whereas five chromatin types were defined on the basis of those of the Kc167 cell line. Markers for chromatin features are indicated at the bottom. E16: embryonic stage (16–20 h AEL); L3: 3rd instar larval stage. For each sample (each column), enrichments or depletions of the markers in individual chromatin states (A and B) and types (C) are analyzed essentially as in Figure 33, and color-coded by Z-score. The data sets are from the modENCODE consortium (Negre et al., 2011). The combinatorial patterns of the markers, such as H3K4me3 for active promoters, are conserved among the cell lines, E16, and L3.

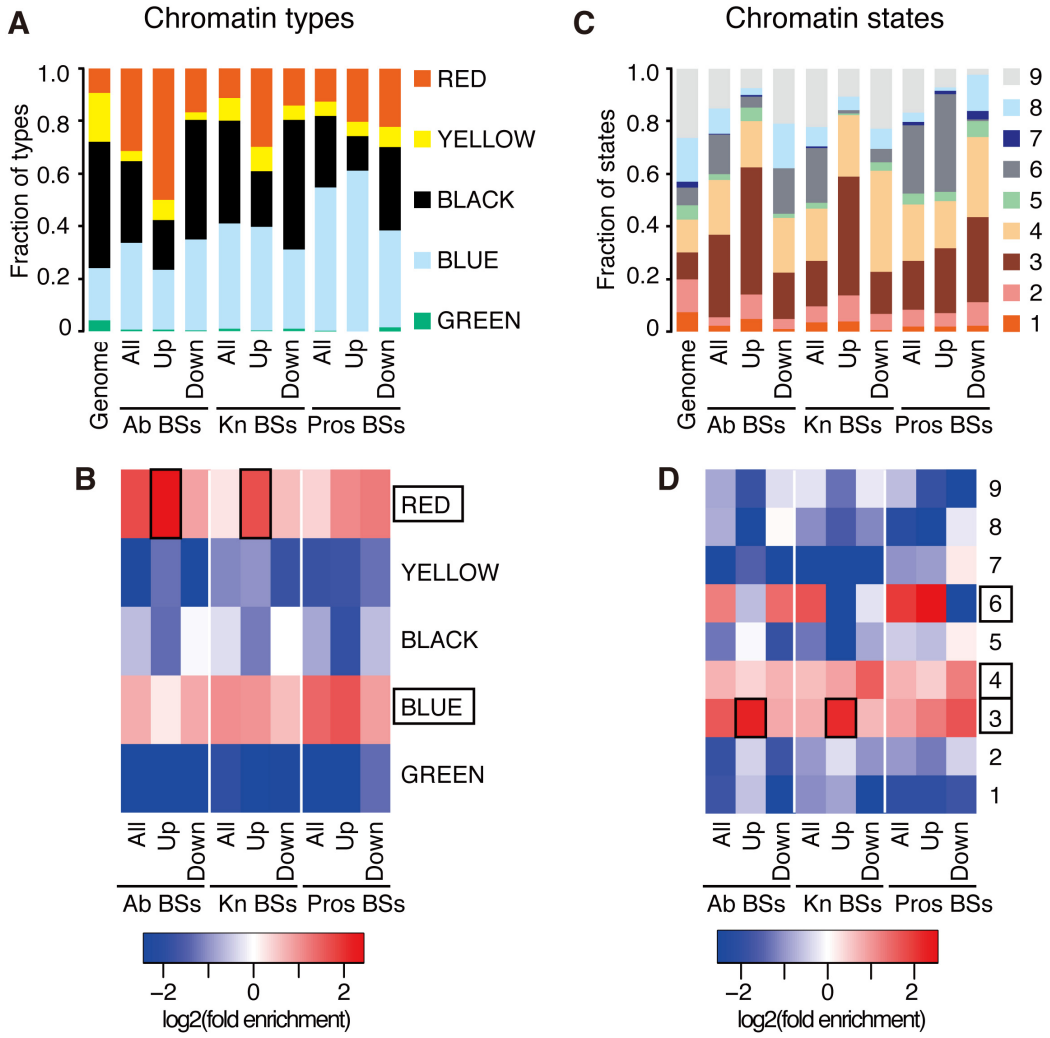

Figure 33. Enrichment of Ab or Kn binding sites in tissue-specific enhancers and Polycomb chromatin

BSs of Ab, Kn, or Pros were sorted into chromatin types that are defined by the data sets of KC167 cells (A and B) or chromatin states that are defined by those of BG3 cells (C and D), and each fraction is shown (A and C). Enrichments/depletions of fractions of individual chromatin types or states are calculated relative to those in the genome and color-coded by fold enrichment (B, D). The data of Pros BSs are derived from Table S1 and S3 of Choksi et al. (2006). Lower limits of the depletion were set to negative values of the maximum enrichment. All: all of the BSs; Up: BSs associated with up-regulated target genes (up-regulated in *ab* ME or *kn* ME, down-regulated in *pros* mutants); and Down: BSs associated with down-regulated target genes (down-regulated in *ab* ME or *kn* ME, up-regulated in *pros* mutants). Most noticeably, RED type chromatin includes 50.0% of the BSs of Ab up-regulated targets (A), and its enrichment is 5.4 fold (red boxes with black frames in “B”). Prominent selectivity was also manifested by the large fractions of UP of the Ab and Kn BSs in state 3 chromatin that is classified into enhancers and intronic regulatory elements (red boxes with black frames; Kharchenko et al., 2010), being consistent with the enrichment of the DamID BSs in introns (Figure 22).

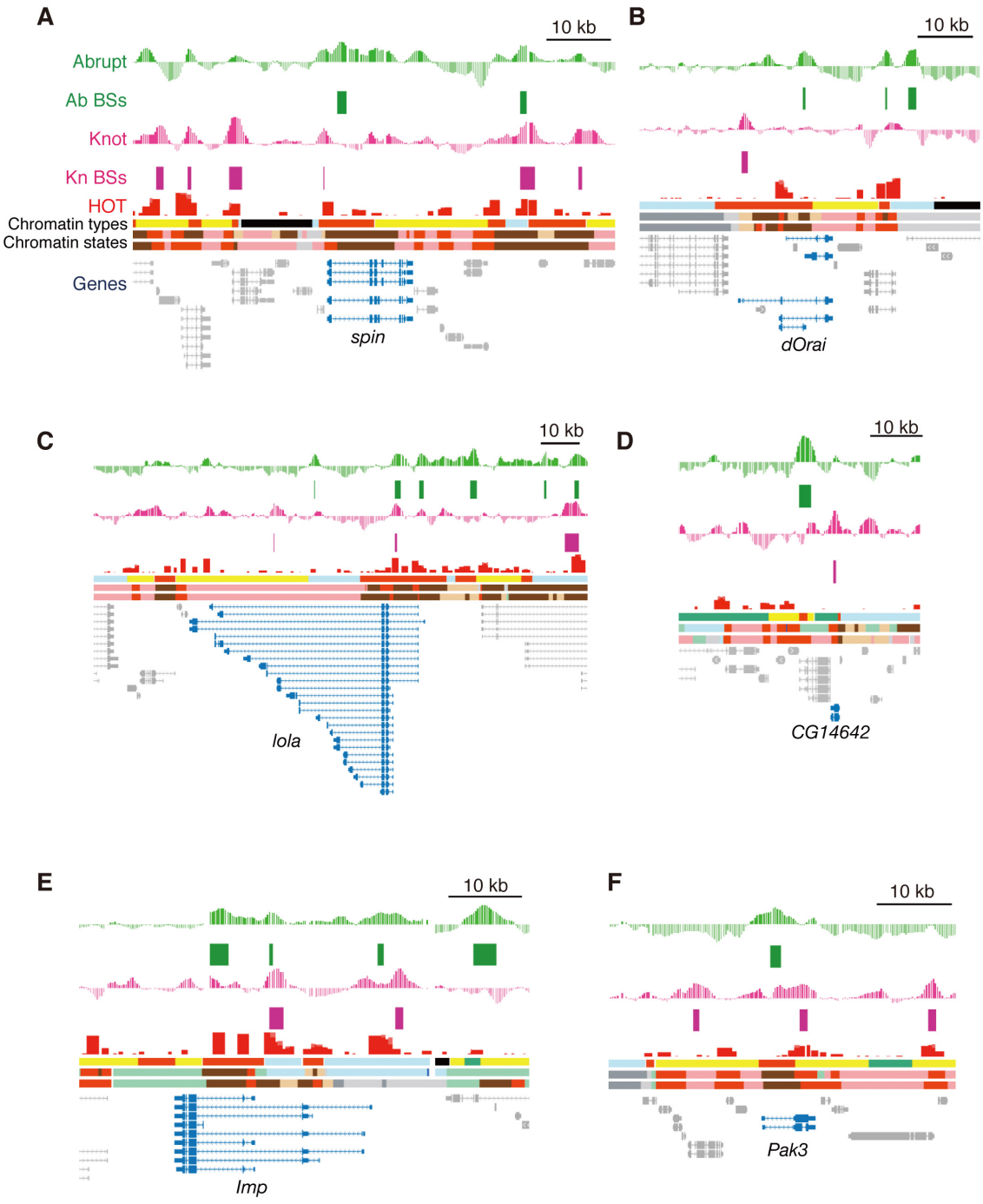

Figure 34. TF binding profiles and chromatin signatures around target genes
DamID profiles of Ab or Kn, distributions of Ab BSs, Kn BSs, and HOT regions, chromatin types, chromatin states, and genes near *spin* (A), *dOrai* (B), *lola* (C), *CG14642* (D), *Imp* (E), *Pak3* (F).

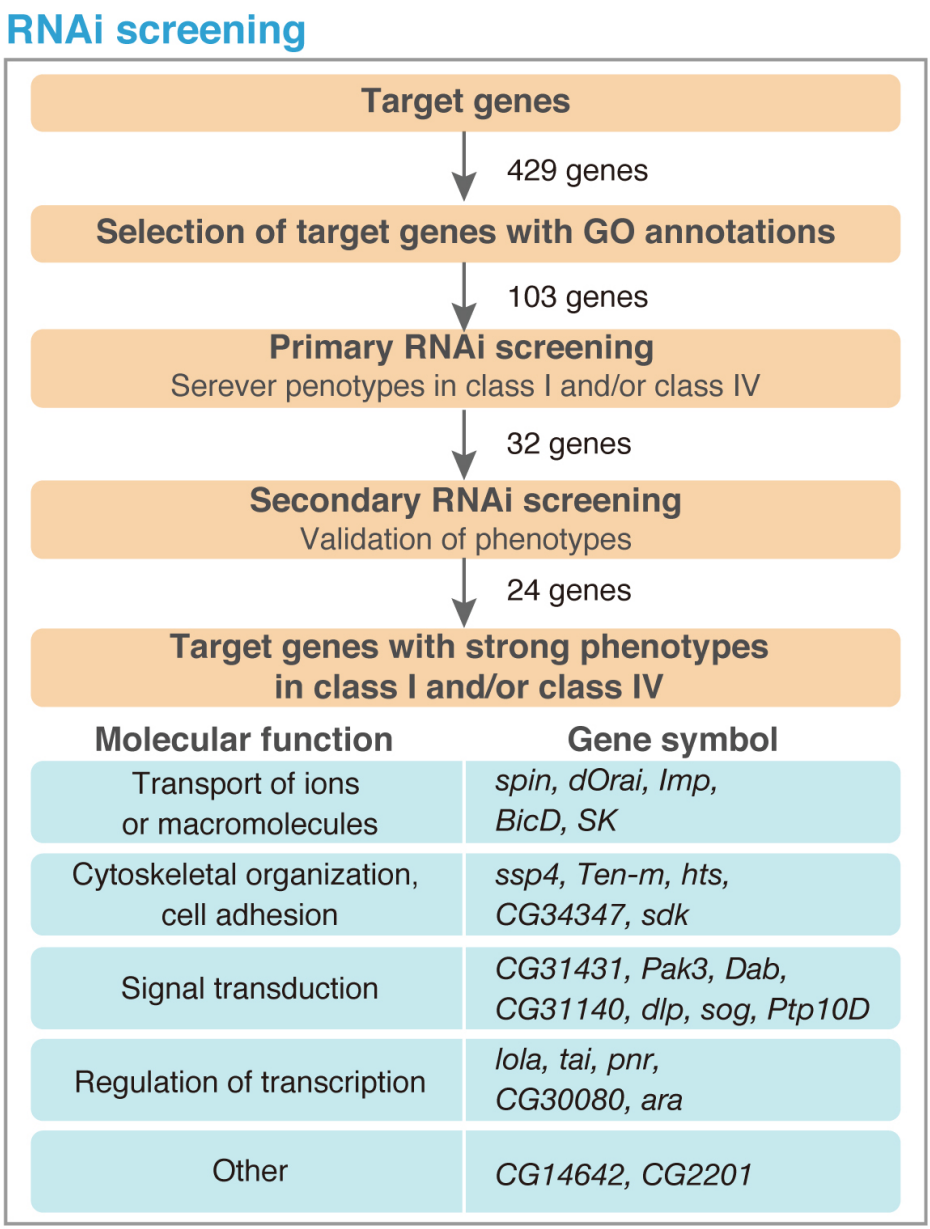

Figure 35. Overview of RNAi screening

Using the list of the target genes, I conducted a small-scale in situ hybridization screening and found that probes for genes with no GO annotation gave signals in embryos barely above the limit of sensitivity of my experimental conditions (data not shown). Thus, I selected 103 genes on the basis of GO terms and performed a primary RNAi screening. 32 genes exhibited morphological defects in dendritic arbors of class I and/or IV when knocked down. Out of these 32, I conducted a secondary RNAi screening using available transgenic stocks of dsRNA targeted to other sequences. 24 target genes had strong knockdown phenotypes, which were validated with two distinct dsRNA sequences. Many of these targets have eluded previous mutant screenings, and they can be categorized into 5 molecular functions (blue boxes).

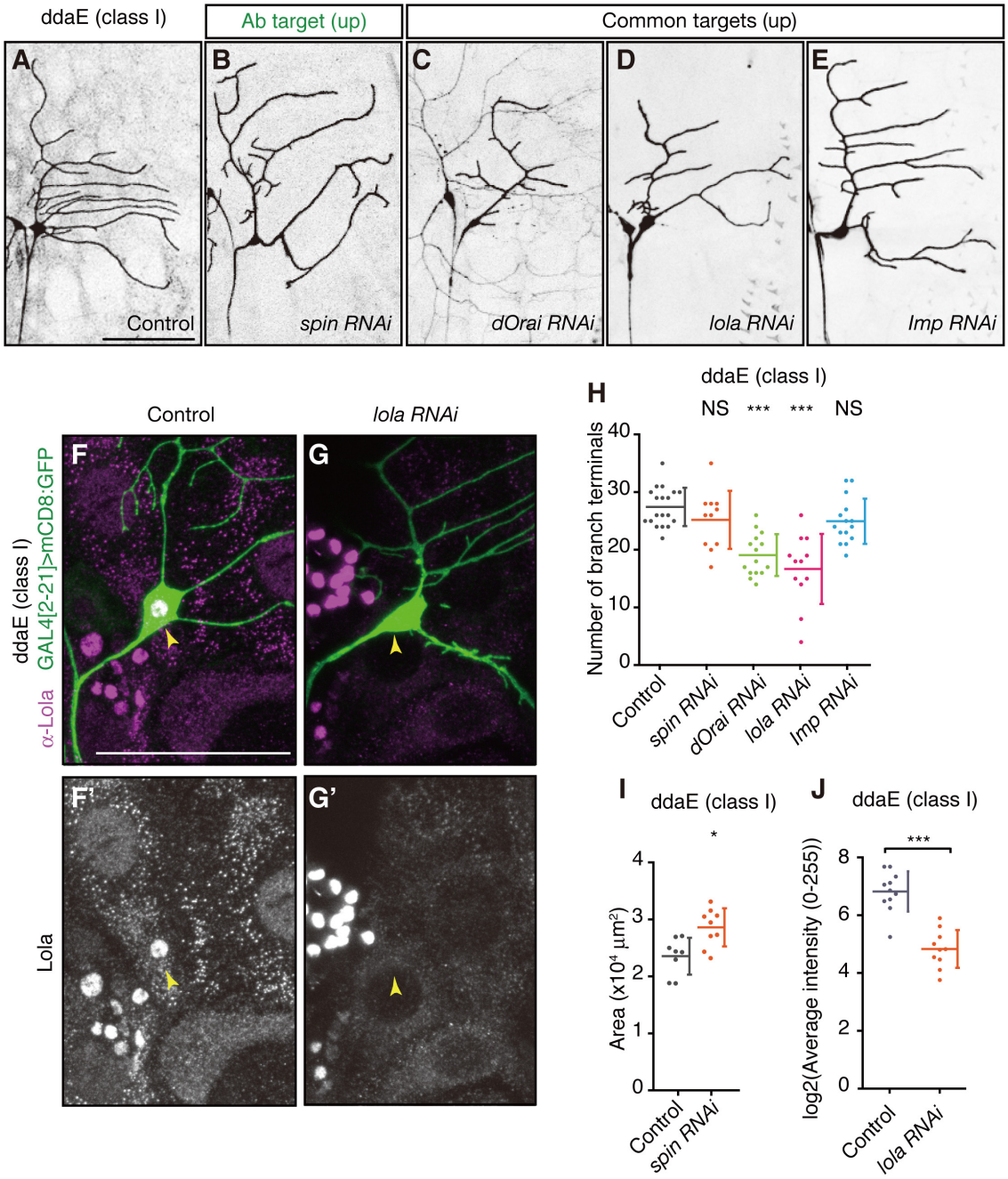

Figure 36. Effects of knockdown of target genes on dendrite morphogenesis of class I neuron ddaE

(A-E) Images of class I neuron ddaE. Control (A), *spin-RNAi* (B), *dOrai-RNAi* (C), *lola-RNAi* (D), and *Imp-RNAi* (E).

(H-I) Quantitative analyses. The terminal number (H) and the size (I) of the ddaE arbor. Error bars indicate the mean ± s.d. * $P < 0.05$, *** $P < 0.001$. NS: Statistically not significant ($P > 0.05$). (H) One-way ANOVA and HSD *post-hoc* test. (I) Wilcoxon-Mann-Whitney test. Bar, 100 µm.

(F-G' and J) Knockdown of *lola* was confirmed by the reduced immunohistochemical signals in ddaE. Representative images of the staining in the control (F and F'), and *lola-RNAi* (G

and G') class I neuron ddaE in wandering larvae. Images of the marker GFP (green in F and G) and Lola (magenta in F and G; F' and G'). Cell bodies of class I neuron ddaE are marked by arrowheads.
(J) The reduction of the Lola signal was validated by statistical analysis of log2-transformed signal intensities of immunostaining. *** $P < 0.001$ (Wilcoxon-Mann-Whitney test). Bar, 50 µm.
Relevant genotypes are *UAS-dicer2/+; GAL4$^{2-21}$ UAS-mCD8:GFP/+*(A),
UAS-dicer2/+; GAL4$^{2-21}$ UAS-mCD8:GFP/UAS-spin-RNAi(TRiP27702) (B),
UAS-dicer2/+; GAL4$^{2-21}$ UAS-mCD8:GFP/UAS-dOrai-RNAi(VDRC12221) (C),
UAS-dicer2/+; GAL4$^{2-21}$ UAS-mCD8:GFP/UAS-lola-RNAi(VDRC101925) (D),
UAS-dicer2/+; GAL4$^{2-21}$ UAS-mCD8:GFP/UAS-Imp-RNAi(VDRC20321) (E).
Actual P values are as follows: 0.9456, < 0.0001, < 0.0001, and 0.8374 (H, from left to right), 0.0111 (I), 0.0002 (J).

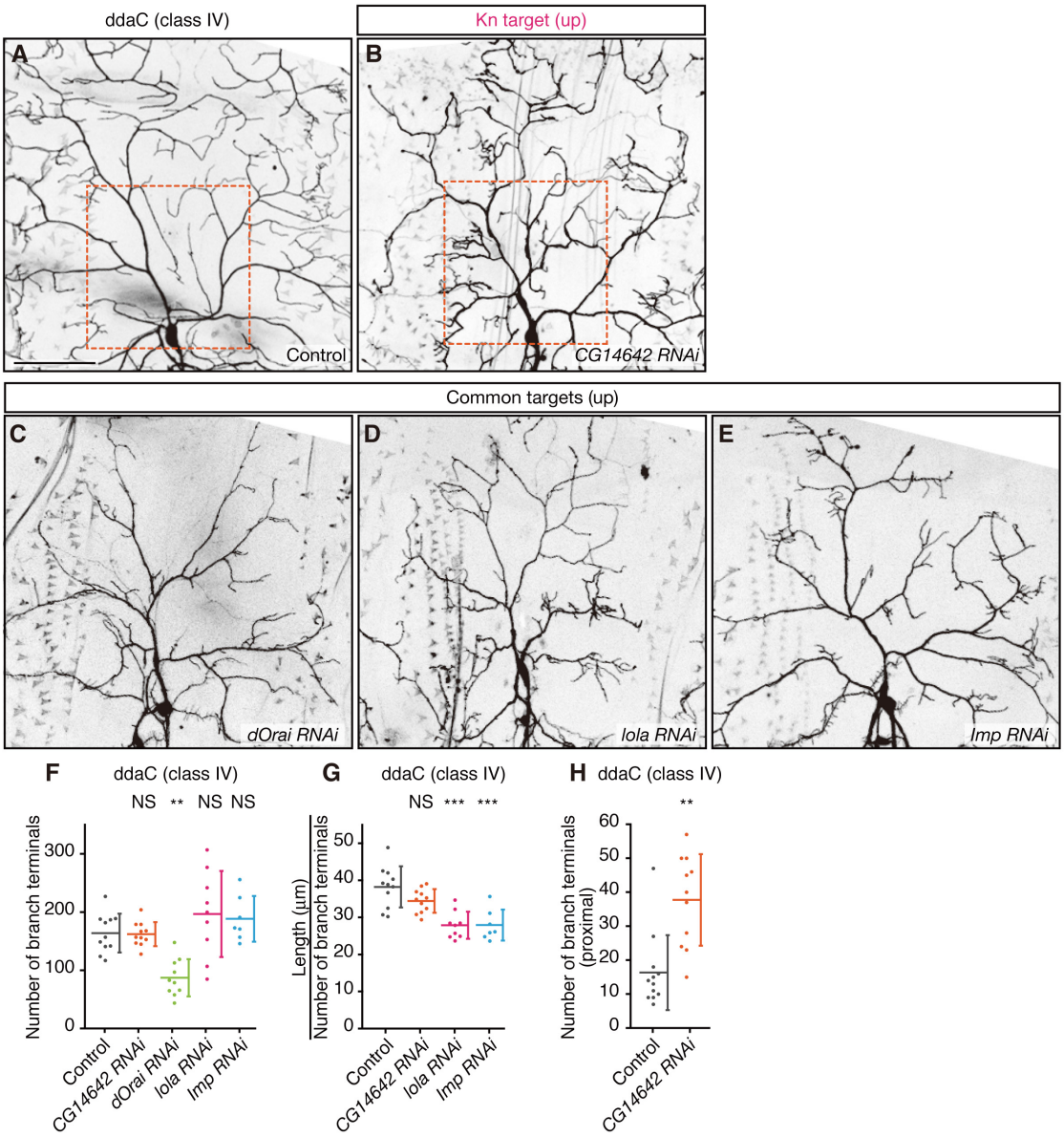

Figure 37. Effects of knockdown of target genes on dendrite morphogenesis of class IV ddaC

(A-E) Images of class IV ddaC. Control (A), *CG14642-RNAi* (B), *dOrai-RNAi* (C), *Iola-RNAi* (D), and *Imp-RNAi* (E). (F-H) Quantitative analyses. The terminal number (F), cumulative branch length divided by the terminal number (G) of the dorsal side, and the terminal number of the proximal region (H; the boxed 200μm x 200μm regions in A and B) of the ddaC arbor. Error bars indicate the mean ± s.d. ** $P < 0.01$, *** $P < 0.001$. NS: Statistically not significant ($P > 0.05$). (F and G) One-way ANOVA and HSD *post-hoc* test. (H) Wilcoxon-Mann-Whitney test. Bar, 100 μm. Relevant genotypes are *ppk-GAL4 UAS-mCD8:GFP/+; UAS-dicer2/+* (A), *ppk-GAL4 UAS-mCD8:GFP/+; UAS-dicer2/UAS-CG14642-RNAi (VDRC14047)* (B), *ppk-GAL4 UAS-mCD8:GFP/+; UAS-dicer2/UAS-dOrai-RNAi (VDRC12221)* (C), *ppk-GAL4 UAS-mCD8:GFP/+; UAS-dicer2/UAS-Iola-RNAi (VDRC 101925)* (D), *ppk-GAL4 UAS-mCD8:GFP/+; UAS-dicer2/UAS-Imp-RNAi (VDRC20321)* (E). Actual P values are as follows: 1, 0.0014, 0.4345, and 0.7542 (F, from left to right), 0.1827, < 0.0001, and 0.0001(G, from left to right), 0.0013 (H).

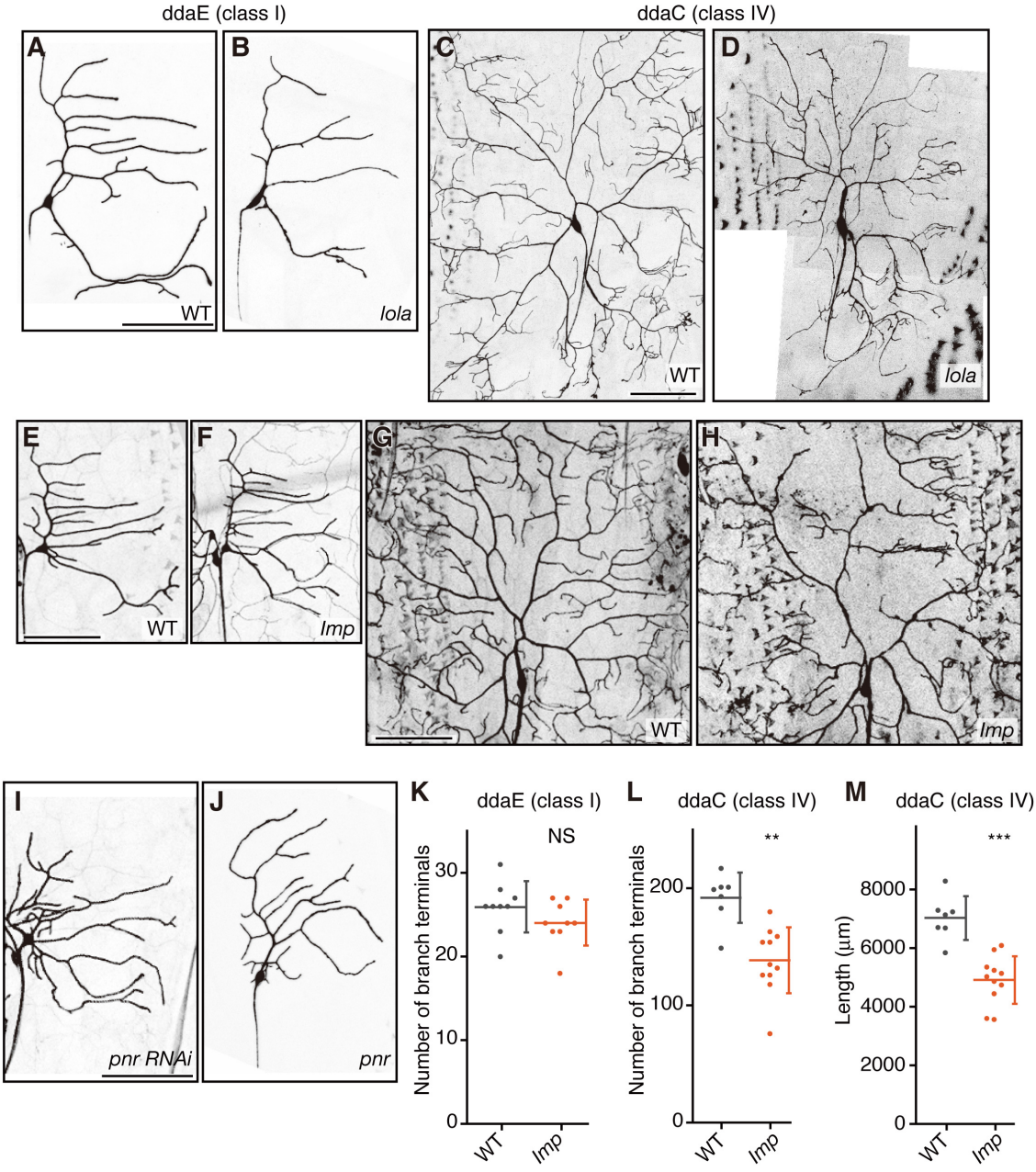

Figure 38. Phenotypes of mutant clones, da neurons in mutants, or knockdowns
(A-D) MARCM analysis.
(A and C) Control clones of class I ddaE and class IV ddaC, respectively.
(B and D) *lola* clones.
Relevant clone genotypes are *hs-FLP, elav-Gal4 UAS-mCD8:GFP/SOP-FLP*$^{\#42}$*; FRT42D* (A and C) and *hs-FLP, elav-Gal4 UAS-mCD8:GFP/SOP-FLP*$^{\#42}$*; FRT42D lola*^{C46} (B and D).
(E-H, K-M) ddaE and ddaC in the wild type (E and G, respectively) and in the *Imp*^{8} mutant (F and H, respectively).
(K-M) Quantitative analyses. The terminal number of the ddaE arbor (K). The terminal number (L), cumulative branch length (M) of the dorsal side of the ddaC arbor.
Relevant genotypes are *+/Y; +; +/GAL4*$^{2\text{-}21}$ *UAS-mCD8:GFP* (E), *Imp*^{8} */Y; +; +/GAL4*$^{2\text{-}21}$

UAS-mCD8:GFP (F), *+/Y; +; +/ppk-GAL4 UAS-mCD8:GFP* (G), *Imp^{8} /Y; +; +/ ppk-GAL4 UAS-mCD8:GFP* (H).
(I) Representative *pnr*-knockdown ddaE (*UAS-dicer2/UAS-pnr-RNAi (VDRC 101522); GAL4$^{2\text{-}21}$ UAS-mCD8:GFP/+*). (J) *pnr* mutant clone (*hs-FLP UAS-mCD8:GFP/+; Gal4$^{109(2)80}$ UAS-mCD8:GFP SOP-FLP$^{\#73}$/+; FRT82B pnr^{VX6}*).
** $P < 0.01$, *** $P < 0.001$ (Wilcoxon-Mann-Whitney test). NS: Statistically not significant ($P > 0.05$). Actual P values are 0.2087 (K), 0.0028 (L), 0.0003 (M).

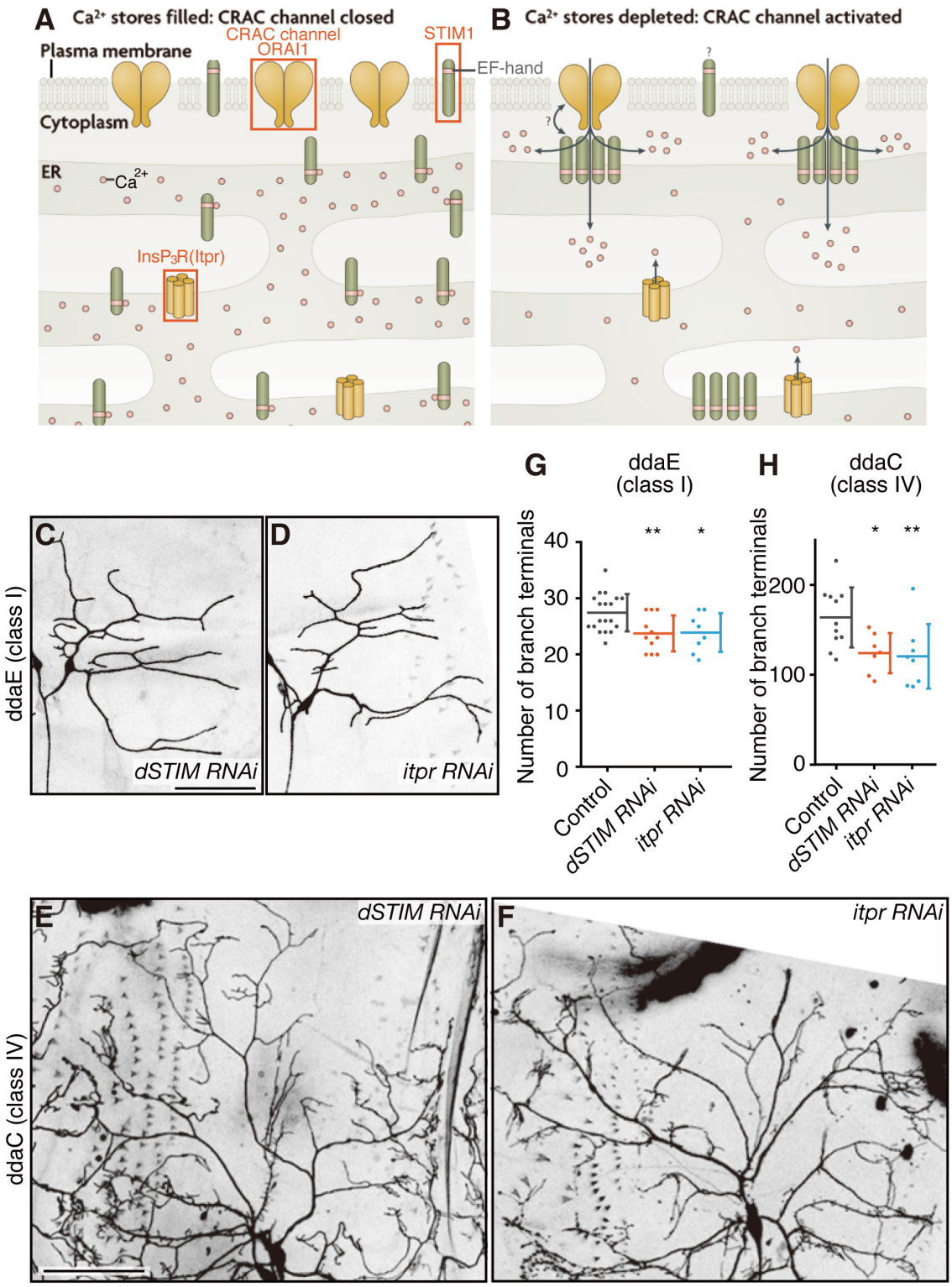

Figure 39. Effects of *dSTIM*- or *itpr*-knockdown in class I and class IV neurons
(A and B) Gating of Ca^{2+} release-activated Ca^{2+} (CRAC) channels. Cell surface receptor stimulation activates two closely coupled components of 'Ca2+ toolkit'; the inositol 1,4,5-trisphosphate receptors (InsP3R; Itpr) followed by CRAC channels. InsP3Rs rapidly release Ca2+ from intracellular stores such as the endoplasmic reticulum (ER) while CRAC

channels (Orai) function to replenish ER stores from the extracellular milieu and contribute to a longer-term Ca2+ signal. Several reports have established that Ca^{2+} depletion of ER stores is sensed by STIM (stromal interaction molecule), an ER membrane protein, which upon store Ca^{2+} depletion oligomerizes in the ER, translocates close to the plasma membrane and organizes the Orai channel into clusters to bring about store operated Ca^{2+} entry.

(C-H) *dSTIM*-knockdown ddaE and ddaC (C and E, respectively) and *itpr*-knockdown ddaE and ddaC (D and F, respectively).

(G and H) Quantitative analyses. The terminal number of the ddaE arbor (G) and that of the dorsal side of the ddaC arbor (H).

Relevant genotypes are *UAS-dicer2/+; GAL4$^{2\text{-}21}$ UAS-mCD8:GFP/UAS-dSTIM-RNAi (TRiP27263)* (C), *UAS-dicer2/+; GAL4$^{2\text{-}21}$ UAS-mCD8:GFP/UAS-itpr-RNAi (VDRC 6484)* (D), *ppk-GAL4 UAS-mCD8:GFP/+; UAS-dicer2/ UAS-dSTIM-RNAi (TRiP27263)* (E), and *ppk-GAL4 UAS-mCD8:GFP/+; UAS-dicer2/UAS-itpr-RNAi (VDRC 6484)* (F).

* $P < 0.05$, ** $P < 0.01$ (One-way ANOVA and HSD *post-hoc* test). Actual P values are 0.0154 and 0.0404 (G, from left to right), 0.0413 and 0.0194 (H, from left to right).

Part A and B are modified from Agrawal et al. (2010); Feske (2007).

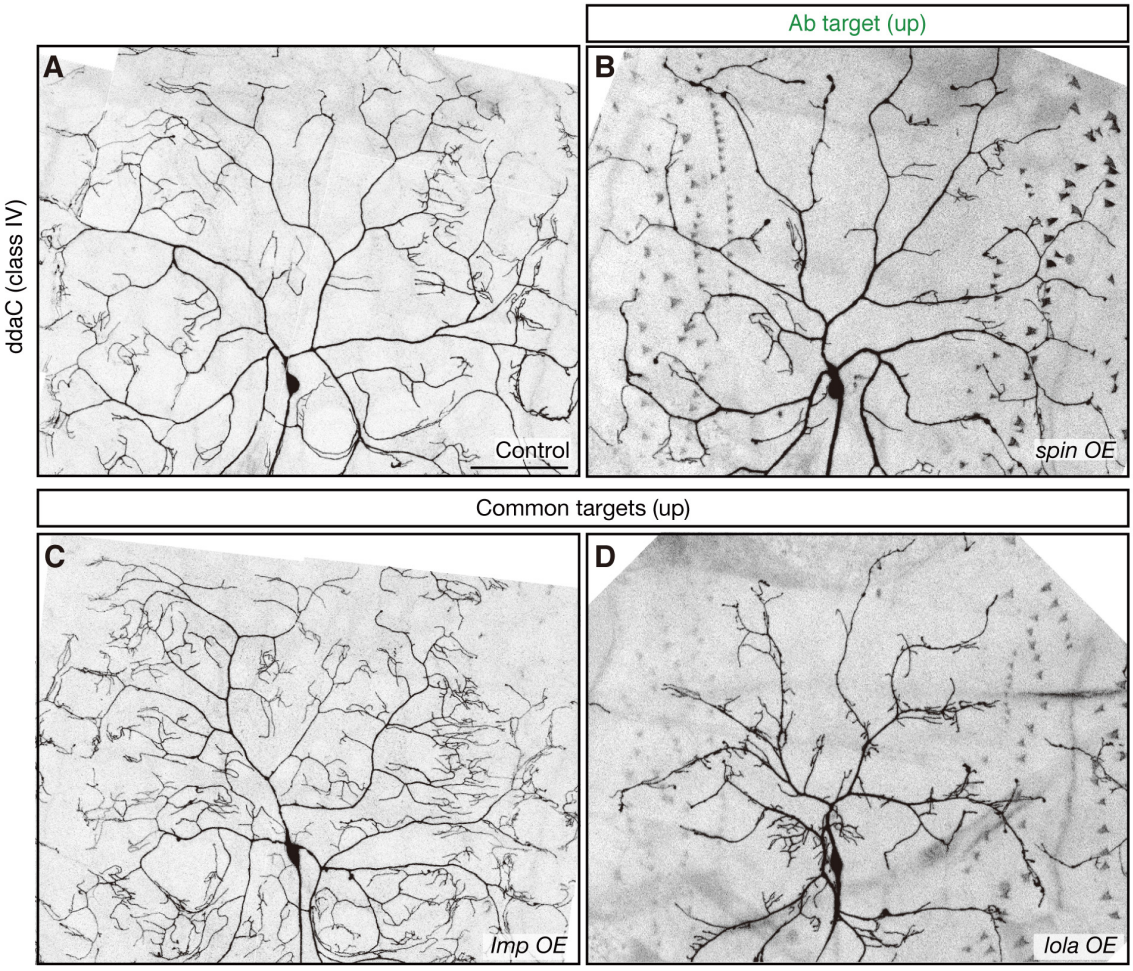

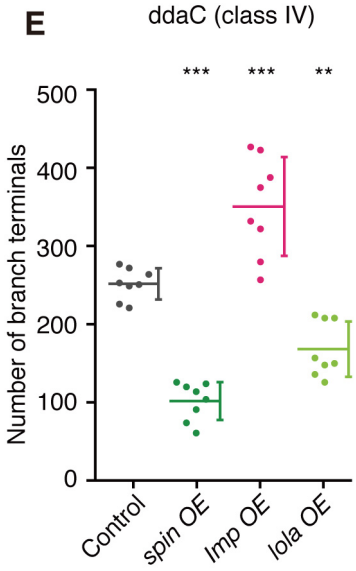

Figure 40. Effects of overexpression of target genes on class IV

(A-D) Images of class IV ddaC. Control (A), *spin*-overexpression (B), *Imp*-overexpression (C), and *lola*-overexpression (D). Bars, 100 µm.

Relevant genotypes are *ppk-GAL4 UAS-mCD8:GFP/+* (A), *ppk-GAL4 UAS-mCD8:GFP/UAS-spin-RFP* (B), *ppk-GAL4 UAS-mCD8:GFP/UAS-Imp-SD* (C), *ppk-GAL4 UAS-mCD8:GFP/UAS-lolaL* (D).

(E) Quantification of terminal numbers of the dorsal side of the ddaC arbor. Error bars indicate the mean ± s.d. * $P < 0.05$, ** $P < 0.01$, *** $P < 0.001$ (one-way ANOVA and HSD *post-hoc* test). Actual P values are as follows: from left to right, < 0.0001, 0.0004, and 0.0035.

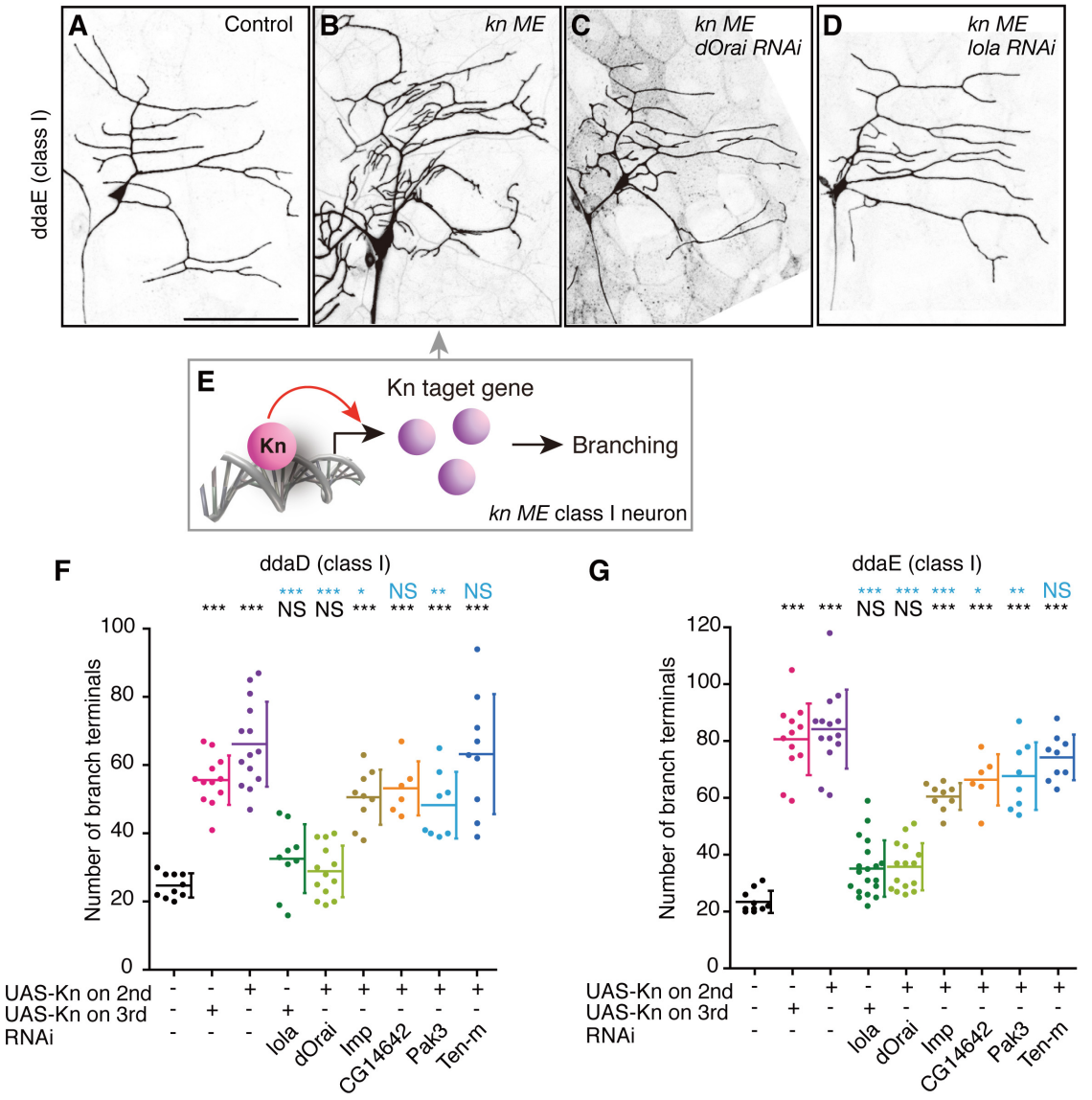

Figure 41. Effects of knockdown of target genes on Kn misexpression-induced transformation

Images of control (A), *kn*-misexpressing (B), *kn* and *dOrai*-dsRNA expressing (C), and *kn* and *lola*-dsRNA expressing (D) class I ddaE.

Misexpression of Kn in class I neurons increases the number of higher-order branches and deforms the comb shape (B), which I designate as a class IV-like transformation (Hattori et al., 2007). I assumed that up-regulation of the Kn target genes most likely contributed to this class IV-like transformation (E). To verify this hypothesis, I misexpressed Kn in class I neurons with concurrent knockdown of individual Kn target genes (C, D, F, and G).

(F and G) Quantitative analyses of the number of branch termini per cell of class I ddaD (F) and ddaE (G) of the indicated genotypes. Most notably, knockdown of *lola* or *dOrai* restored the class IV-like arbor to normal class I with respect to both the branch number and the comb-like shape.

Error bars indicate the mean ± s.d. * $P < 0.05$, ** $P < 0.01$, *** $P < 0.001$ (one-way ANOVA and HSD *post-hoc* test). Black asterisks indicate statistically significant differences from the

control (leftmost dataset), and blue asterisks from the *kn*-misexpressing neuron (the second or third from the left). NS: Statistically not significant ($P > 0.05$).
Actual P values are as follows: < 0.0001, < 0.0001, 0.7452, 0.9867, < 0.0001, < 0.0001, 0.0001, and < 0.0001 (Black in F, from left to right), < 0.0001, < 0.0001, 0.0141, 0.1856, 0.004, and 0.9989 (Blue in F, from left to right), < 0.0001, < 0.0001, 0.078, 0.0732, < 0.0001, < 0.0001, < 0.0001, and < 0.0001 (Black in G, from left to right), 0001, < 0.0001, < 0.0001, 0.0118, 0.0092, and 0.3349 (Blue in G, from left to right).
Bars, 100 μm. Relevant genotypes are *UAS-dicer2/+; GAL4$^{2-21}$ UAS-mCD8:GFP/+* (A), *UAS-dicer2/UAS-Kn:HA; GAL4$^{2-21}$ UAS-mCD8:GFP/+* (B), *UAS-dicer2/UAS-Kn:HA; GAL4$^{2-21}$ UAS-mCD8:GFP/UAS-dOrai -RNAi (VDRC12221)* (C), *UAS-dicer2/UAS-lola-RNAi (VDRC101925); GAL4$^{2-21}$ UAS-mCD8:GFP/UAS-Kn:HA* (D).
Due to a technical difficulty, I was unable to address the relevance of the Ab targets in the Ab misexpression-induced context (see 4-9. RNAi).

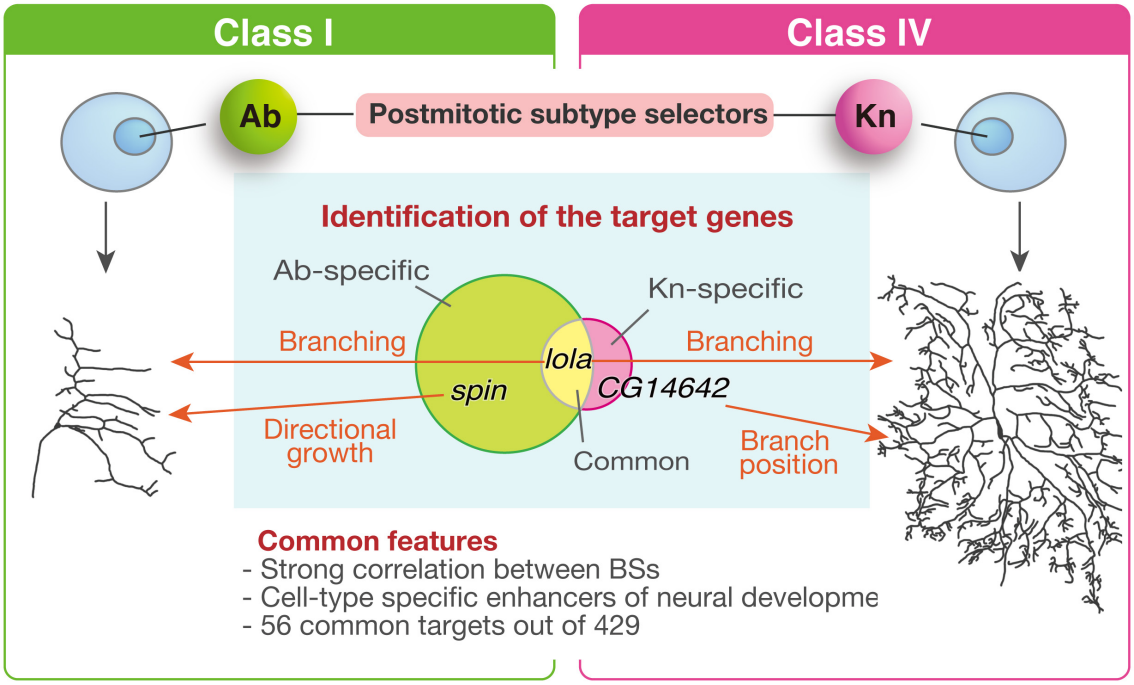

Figure 42. Summary of genome-wide analysis of Ab and Kn

The results identified a group of target genes that were bound and transcriptionally regulated by either key TF, and contributed to morphological diversification of the two classes of neurons. Our genome-wide study strongly supports the notion that the class selectors do indeed control transcription of some target genes selectively. On the other hands, the BSs of both TFs are enriched in cell-type specific enhancers, and they show the same directional regulation of the every common target.

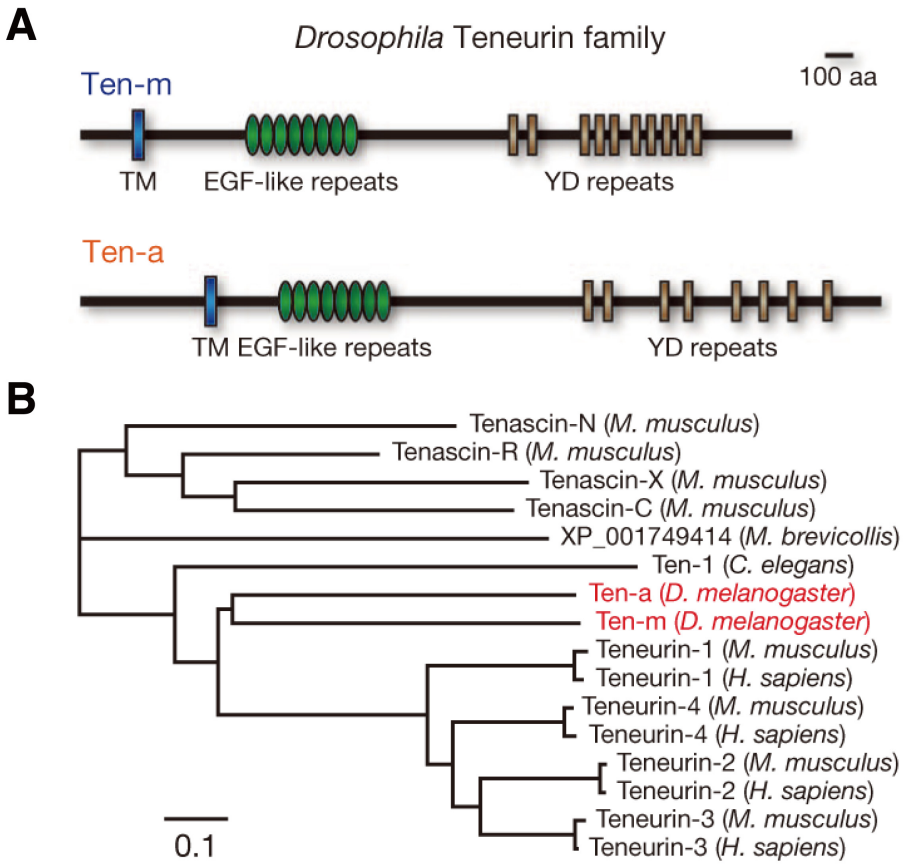

Figure 43. *Drosophila* Teneurins
(A) Domain composition of *Drosophila* Ten-m. aa, amino acids; TM, transmembrane domain. (B) Phylogeny of the *Drosophila* Teneurins (Ten-m and Ten-a) and related proteins in other species. Branch lengths represent units of substitutions per site of the sequence alignment. Adapted from Hong et al. (2012).

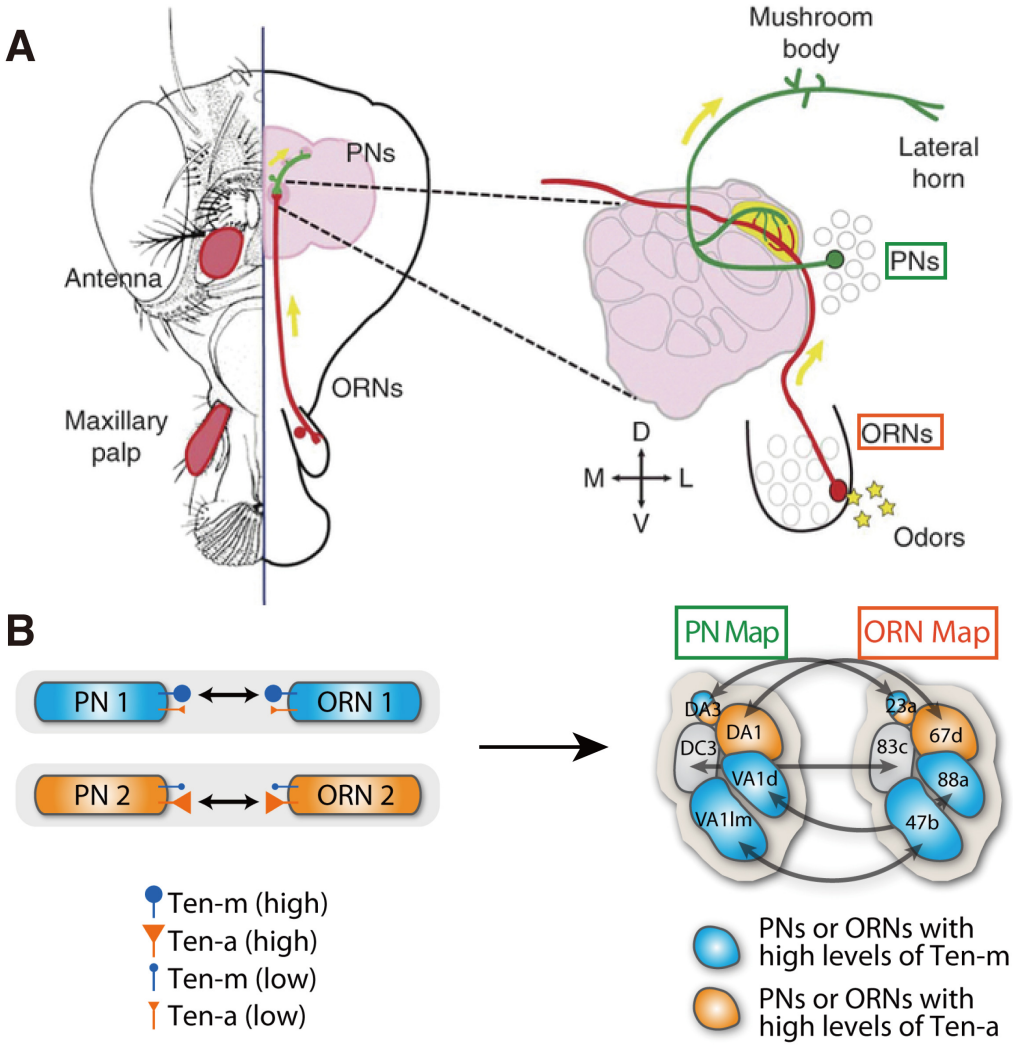

Figure 44. Teneurins is instruct synaptic partner matching in an olfactory map

(A) Schematic of the *Drosophila* olfactory system. Olfactory receptor neurons (ORNs, red) and projection neurons (PNs, green) target their axons and dendrites to genetically pre-specified target glomeruli (yellow) to generate one-to-one neural connections in the antennal lobe.

(B) Teneurins are required for PN–ORN matching. Ten-m and Ten-a are highly expressed in selective matching pairs of ORN and PN classes. Left panel: high-level expression of Ten-m or Ten-a promotes homophilic attraction between partner PN dendrites and ORN axons. Right panel: the homophilic attractions contribute to the PN–ORN matching.

Blue, Ten-m high; orange, Ten-a high.

Part A and B are adapted from Sekine et al. (2013) and Hong et al. (2012), respectively.

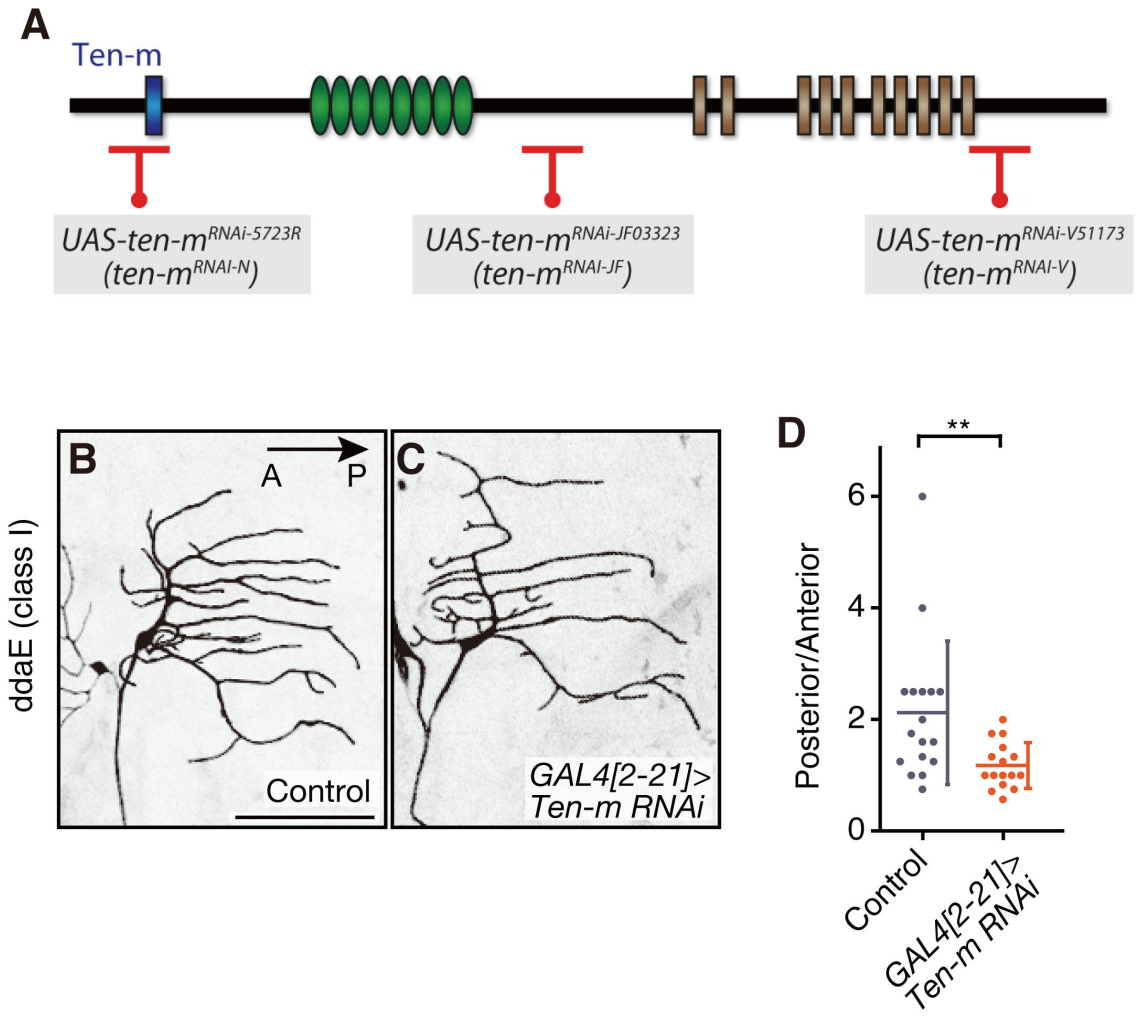

Figure 45. *Ten-m* knockdown phenotypes of class I ddaE

(A) Schematic showing the recognition sites of the *ten-m* RNAi constructs. Multiple RNAi lines targeting *ten-m* were collected and examined (see 4-9. RNAi). Adapted from Hong et al. (2012).

(B-D) Phenotypes of class I neuron ddaE when *Ten-m* was knocked down by using *GAL4[2-21]* (C). (B) Control. Arrow represents the anterior-posterior axis.

(D) Quantitative analysis. The ratio of the number of posterior-directed secondary branches to the number of anterior-directed secondary branches was plotted. Error bars indicate the mean ± s.d. ** $P < 0.01$ (Wilcoxon-Mann-Whitney test; actual P value is 0.0055).

Relevant genotypes are *UAS-dicer2/+; GAL4$^{2-21}$ UAS-mCD8:GFP/+* (B), *UAS-dicer2/+; GAL4$^{2-21}$ UAS-mCD8:GFP/UAS-Ten-m-RNAi (VDRC51173)* (C).

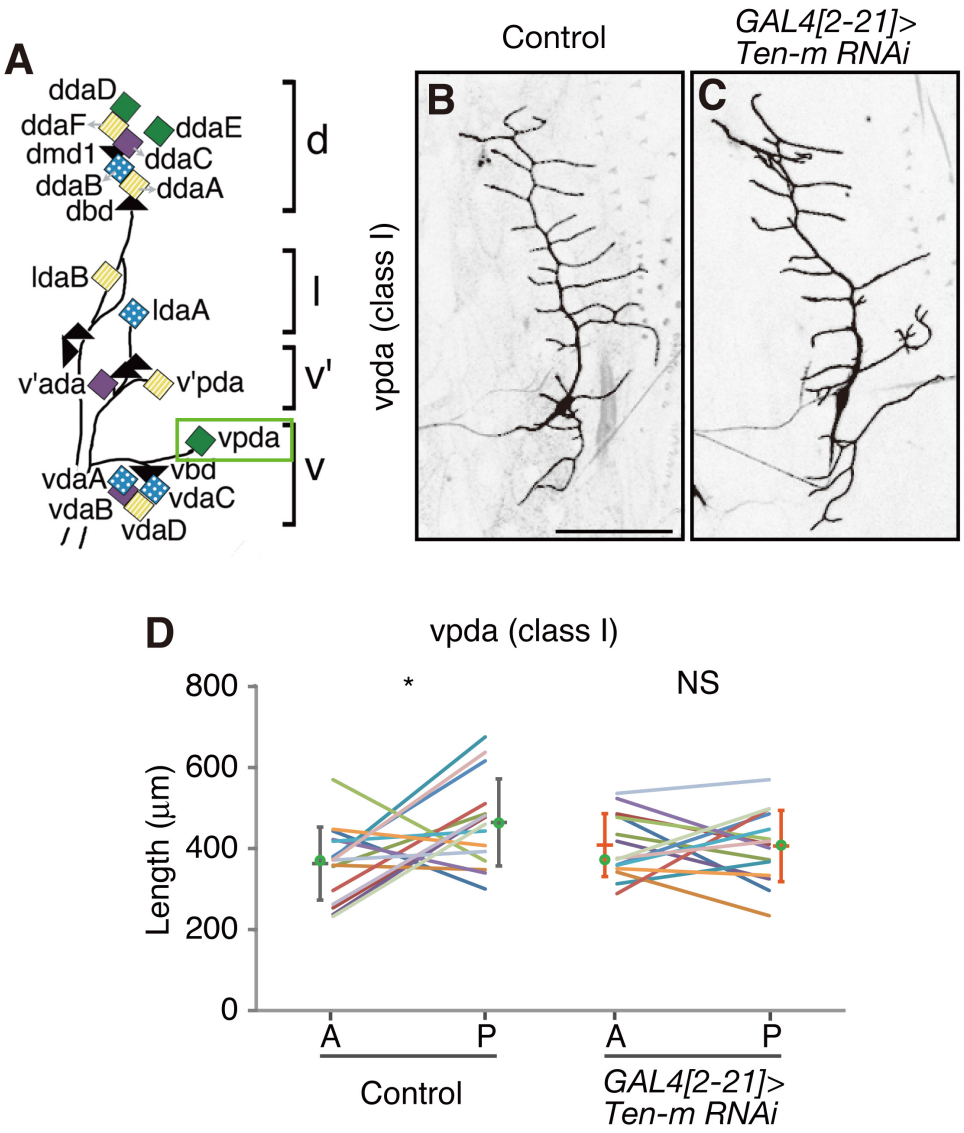

Figure 46. *Ten-m* knockdown phenotypes of class I vpda

(A) A diagram of positions of multidendritic neurons, including class I neuron vpda (green box). (B) Control class I neuron vpda. (C) vpda when *Ten-m* was knocked down by using *GAL4[2-21]*. (D) Quantitative analysis. Length of individual branches anterior (A) to or posterior (P) to dorsally-oriented primary ones was measured and then the total length of A or P branches was plotted. Line segments identify the values from individual neurons. Median values are marked by green points. Error bars indicate the mean (horizontal bar) ± s.d. * $P < 0.05$ (Wilcoxon matched pairs test). Actual P values are 0.0250 (Control) and 0.8904 (*Ten-m RNAi*).

The P-directed growth preference was lost by the knockdown (NS). When the ratio of the number of anterior-directed secondary branches to the number of posterior-directed secondary branches was compared (as I did for ddaE in Figure 45D), the difference was not statistically significant (data not shown). Relevant genotypes are *UAS-dicer2/+; GAL4$^{2-21}$ UAS-mCD8:GFP/+* (A) and *UAS-dicer2/+; GAL4$^{2-21}$ UAS-mCD8:GFP /UAS-Ten-m-RNAi (VDRC51173)* (B). Bars, 100 µm.

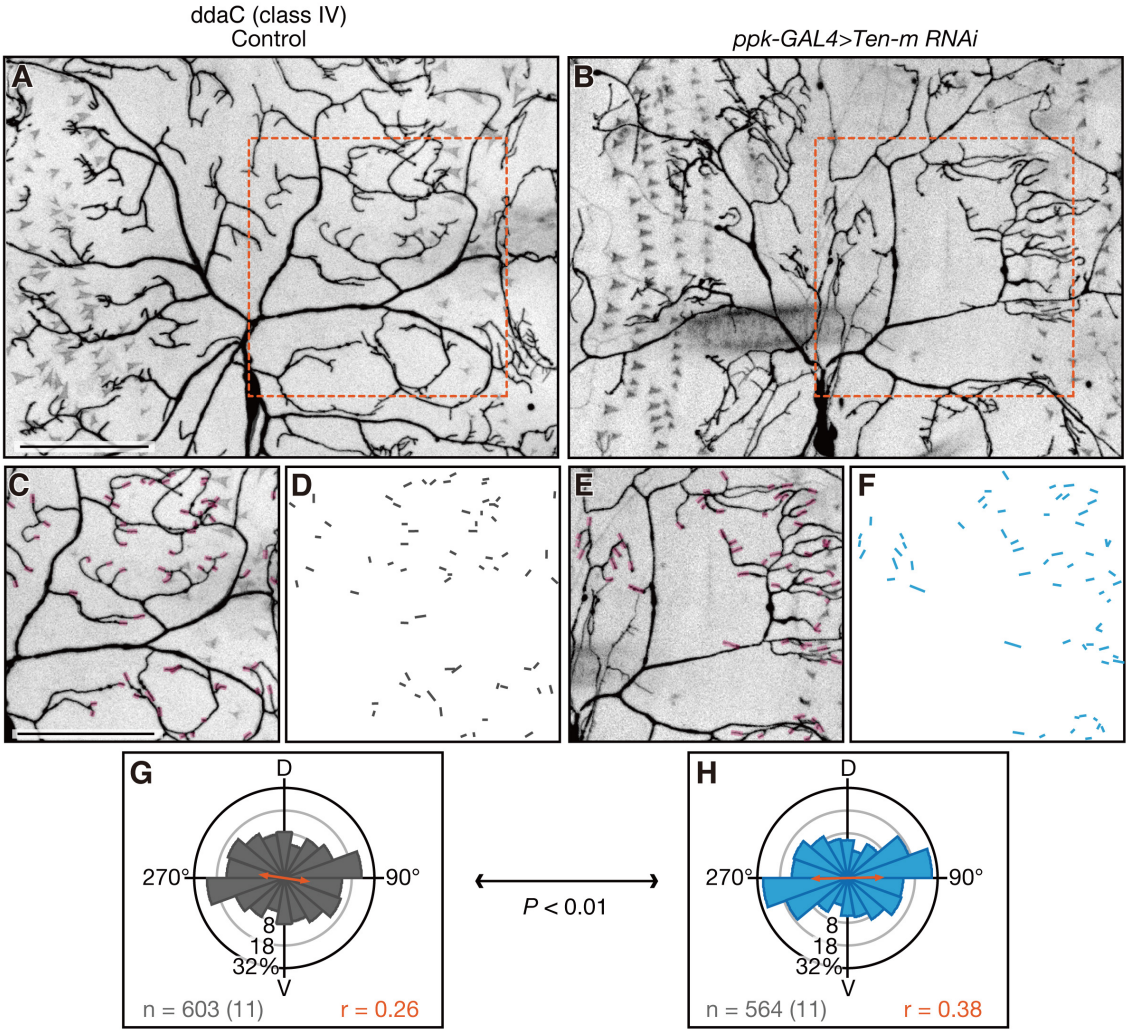

Figure 47. Effects of *Ten-m* knockdown in class IV ddaC on orientation distributions of its branch termini

Images of class IV ddaC when *Ten-m* was knocked down by using *ppk-GAL4* (B, E, and F). (A, C, and D) Control.

(C-F) High-power images of boxed areas in A and B. Orientations of branch termini are defined by short line segments, which trace termini to 5-10 μm-distant intra-branch points (D and F). Bars, 100 μm.

(G and H) Orientation distributions of branch termini. In each rose diagram, angles are classed into 9 bins (20° for each bin) and visualized in a point symmetry manner. Data of individual genotypes were collected from 200μm x 200μm boxed areas in A and B. Indicated at a lower left-hand corner of each rose diagram are the number of branch termini and the number of neurons from which the data were collected (in parentheses). The lengths of the mean vector (orange arrows) are indicated (r). Knockdowns significantly biased the orientation distribution (Mardia-Watson-Wheeler test; actual P value is 0.0058).

Relevant genotypes are *ppk-GAL4 UAS-mCD8:GFP/+; UAS-dicer2/+* (A, C, D, and G), *ppk-GAL4 UAS-mCD8:GFP/+; UAS-dicer2/UAS-Ten-m-RNAi (VDRC51173)* (B, E, F, and H).

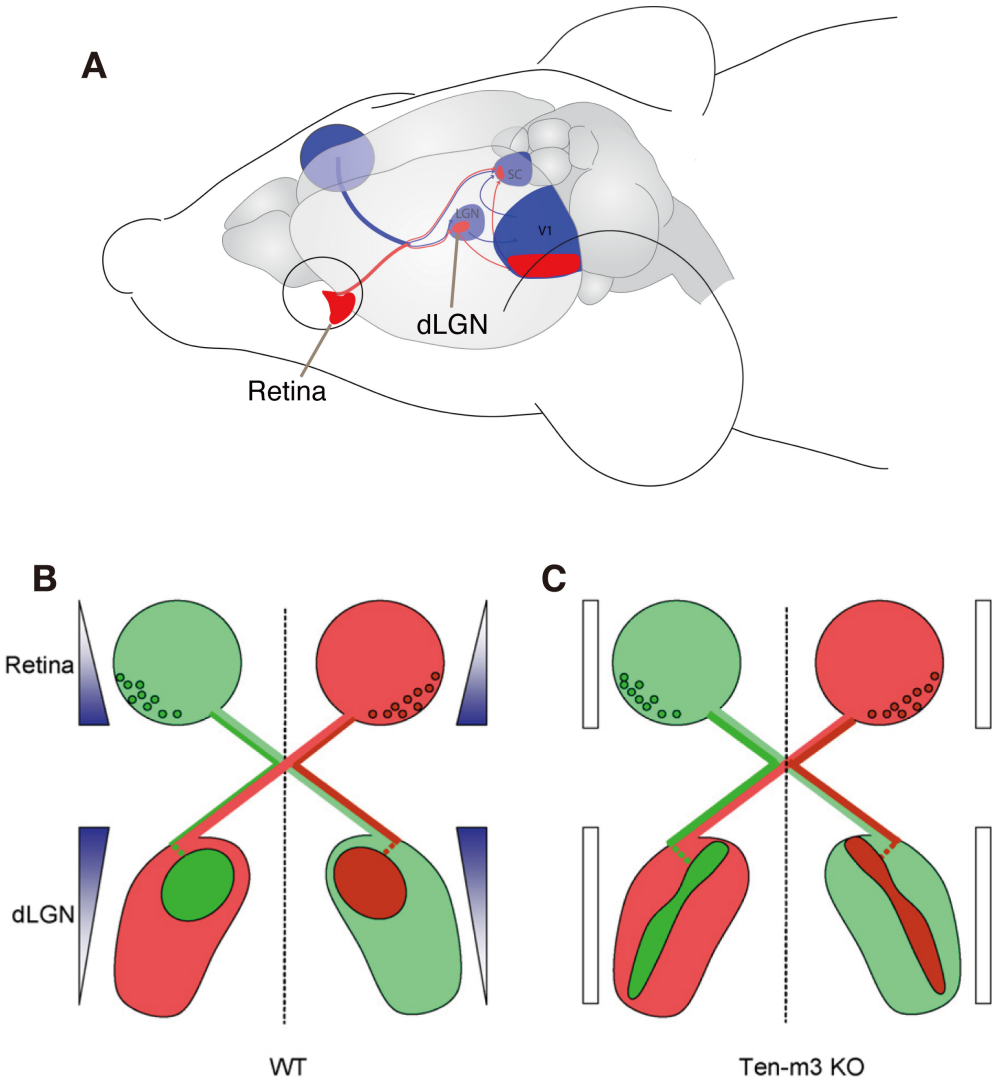

Figure 48. Function of Ten-m3 in retinal mapping

(A) A schematic diagram of the main visual system circuitry in the mouse. dLGN: dorsal lateral geniculate nucleus. Adapted from Wilks et al. (2013).

(B and C) Schematic diagram depicting expression gradient of Ten-m3 in WT retina and dLGN (B), and alterations in retinal mapping seen in Ten-m3 knockouts (KOs; C). Small darker green and red circles indicate position of the ipsilaterally projecting retinal ganglion cells, and darker green and red lines show their terminations.

(B) The ipsilateral axons expressing high levels of Ten-m3 normally map to a region of high expression in the WT dLGN.

(C). In Ten-m3 KOs, ipsilaterally projecting retinal ganglion cells originate from the same region of retina, but they are spread along the entire dorso–ventral axis of the nucleus. Dotted line represents midline. Dorsal is to the top. Adapted from Young and Leamey (2009).

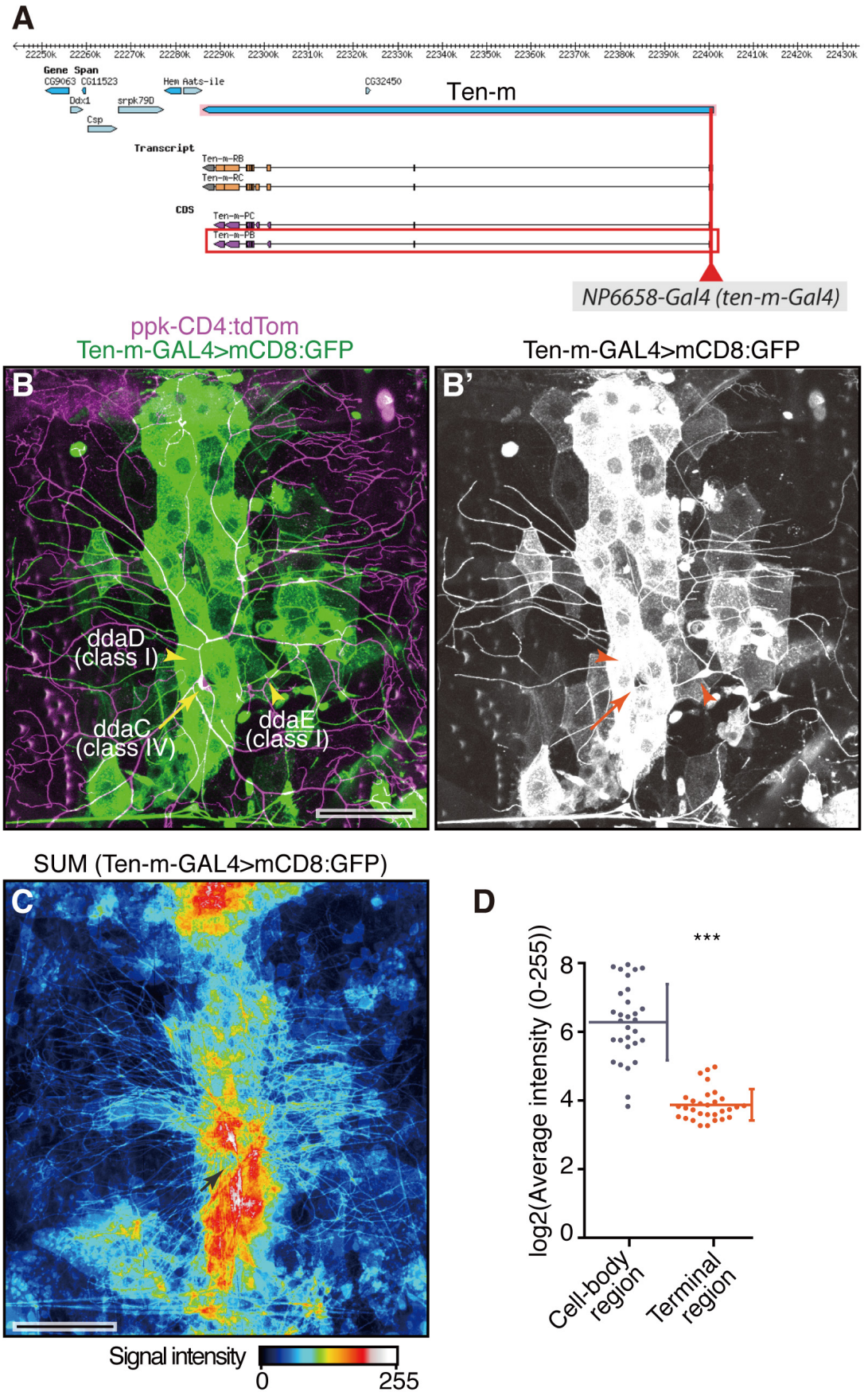
A
Gene Span
Ten-m
Transcript
Ten-m-RB
Ten-m-RC
CDS
Ten-m-PC
Ten-m-PB
NP6658-Gal4 (ten-m-Gal4)
ppk-CD4:tdTom
Ten-m-GAL4>mCD8:GFP
B
ddaD
(class I)
ddaC
(class IV)
ddaE
(class I)
Ten-m-GAL4>mCD8:GFP
B'
SUM (Ten-m-GAL4>mCD8:GFP)
C
Signal intensity
0
255
D
***
log2(Average intensity (0-255))
8
6
4
2
0
Cell-body region
Terminal region

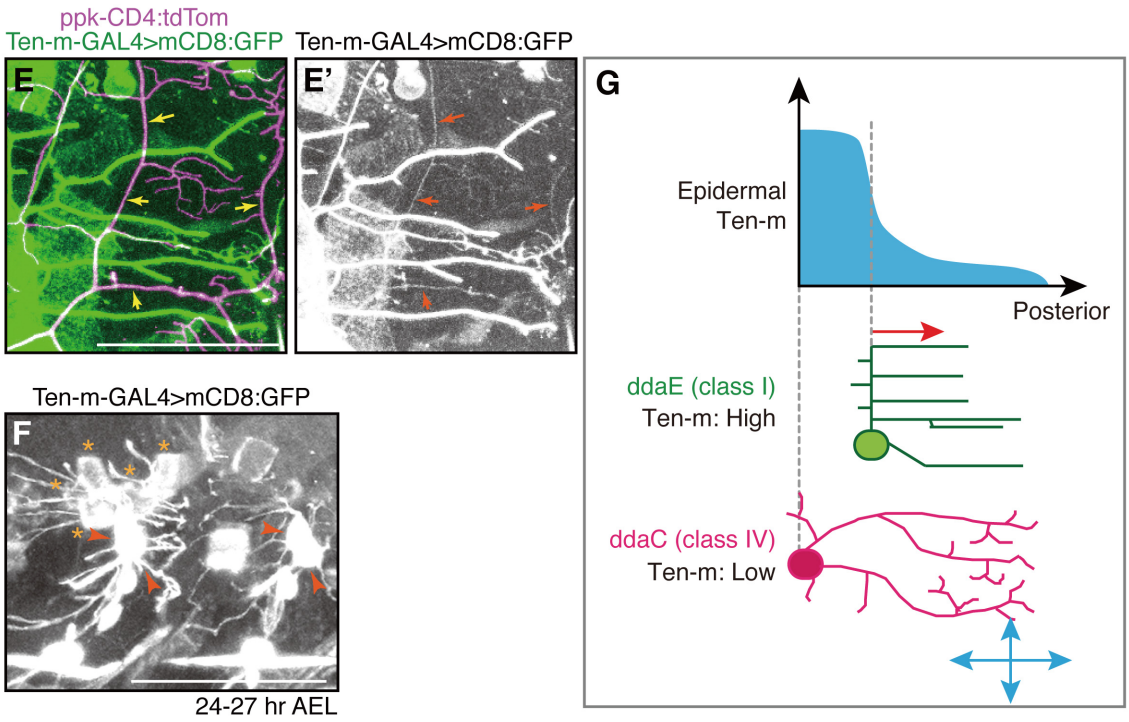

Figure 49. *Ten-m* expression pattern in neuronal and non-neuronal tissues

(A) Schematic showing the *ten-m* genomic region. *NP6658-GAL4* (*ten-m-GAL4*) is a GAL4 enhancer trap located near the 5' end of the *ten-m* coding sequence. Adapted from Hong et al. (2012).

(B-F) *Ten-m* expression in dorsal regions in larval hemisegments. *Ten-m* expression pattern was monitored by mCD8:GFP expression under the *Ten-m-GAL4* enhancer trap line (green in B and E, and B', C, E', F) and co-imaged with a class IV marker *ppk-CD4:tdTom* (magenta in B and E). Cell bodies of class I and IV neurons are marked by arrowheads and arrows, respectively. Dendritic branches of class I are labeled much more intensely than those of class IV by *Ten-m-GAL4*, and the cell bodies of both classes are almost masked by strong signals of overlying epidermis (B and B').

(C) Images of ten hemisegments are overlaid with reference to cell bodies of class IV ddaC (arrow) and the signal intensity is represented by the indicated color code.

(D) Quantification of mCD8:GFP signals in epidermis encompassing the cell bodies (cell-body region) and those close to branch termini of class I ddaE (terminal region). Error bars indicate the mean ± s.d. *** $P < 0.001$ (Wilcoxon-Mann-Whitney test; actual P value is < 0.0001).

(E and E') High-power images of proximal dendritic regions of ddaE and class IV ddaC. In contrast to ddaE branches that were strongly labeled by *Ten-m GAL4*, *ppk-CD4:tdTom*-positive branches of ddaC were only weakly visualized by *Ten-m GAL4* (arrows).

(F) 24-27 hr AEL larva. Labeled cells include ddaD, ddaE (arrows), and a subset of epidermal cells (asterisks).

(G) Schematic diagram depicting expression levels of Ten-m in class I ddaE, class IV ddaC and overlying epidermal cells.

Relevant genotypes are +/*UAS-mCD8:GFP; NP6658/ppk-CD4:tdTom* (B-C, E, and E'), +/*UAS-mCD8:GFP; NP6658/+* (F). Bars, 100 μm (B-C, E, and E'); 50 μm (F).

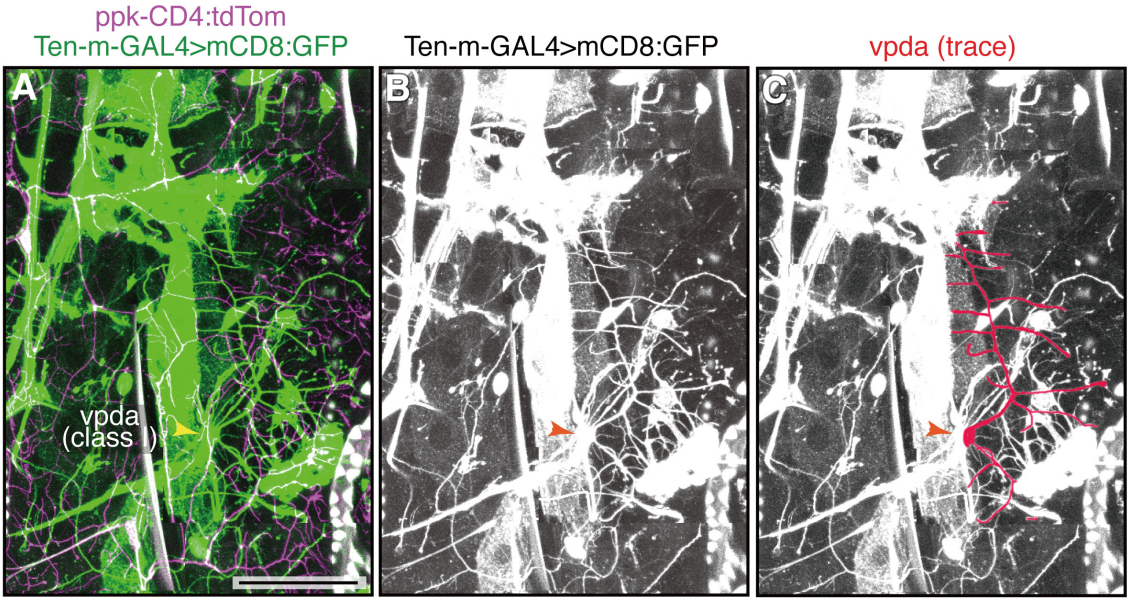

Figure 50. The *Ten-m* expression in a ventral region in larval hemisegments
Cell bodies of class I vpda are marked by arrowheads. *Ten-m* expression pattern was monitored by mCD8:GFP expression under the *Ten-m-GAL4* line. Dendritic branches of class I vpda are traced in C. Relevant genotype is +/*UAS-mCD8:GFP; NP6658 /ppk-CD4:tdTom*. Bar, 100 μm.

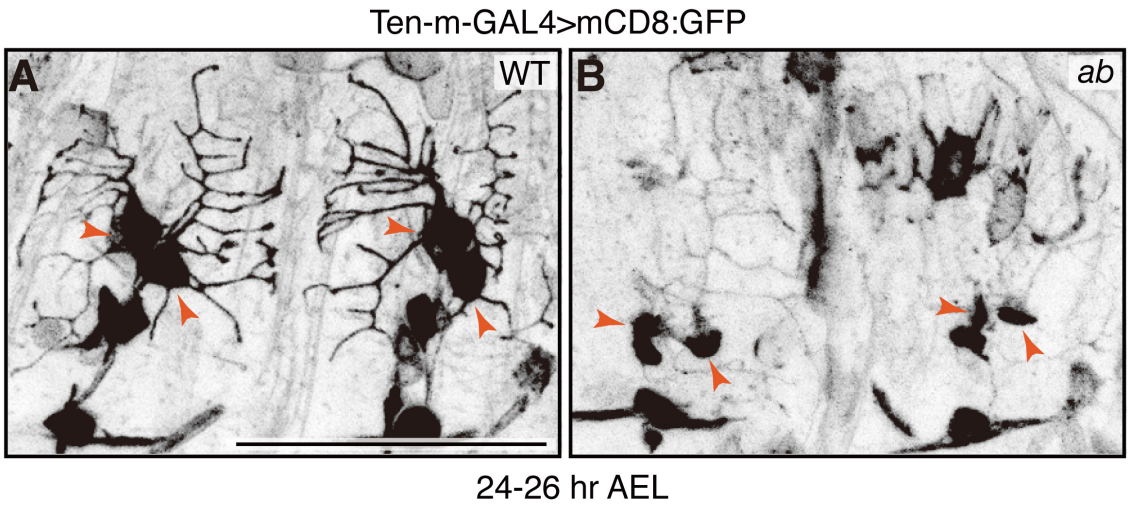

Figure 51. Decrease in *Ten-m* expression level in an *ab* mutant larva

24-26 hr AEL larvae. *Ten-m* expression in dorsal regions in larval hemisegments. *Ten-m* expression pattern was monitored by mCD8:GFP expression under the *Ten-m-GAL4* enhancer trap line. Cell bodies of class I ddaD and ddaE are marked by arrowheads. Note that signals in dendrites were hardly seen in the *ab* mutant. Bar, 50 μm. Relevant genotypes are *+/FRT40A; +/NP6658,UAS-mCD8:GFP* (A), ab^{clu1}/ab^{k02807} *FRT40A* ; *+/NP6658,UAS-mCD8:GFP* (B).

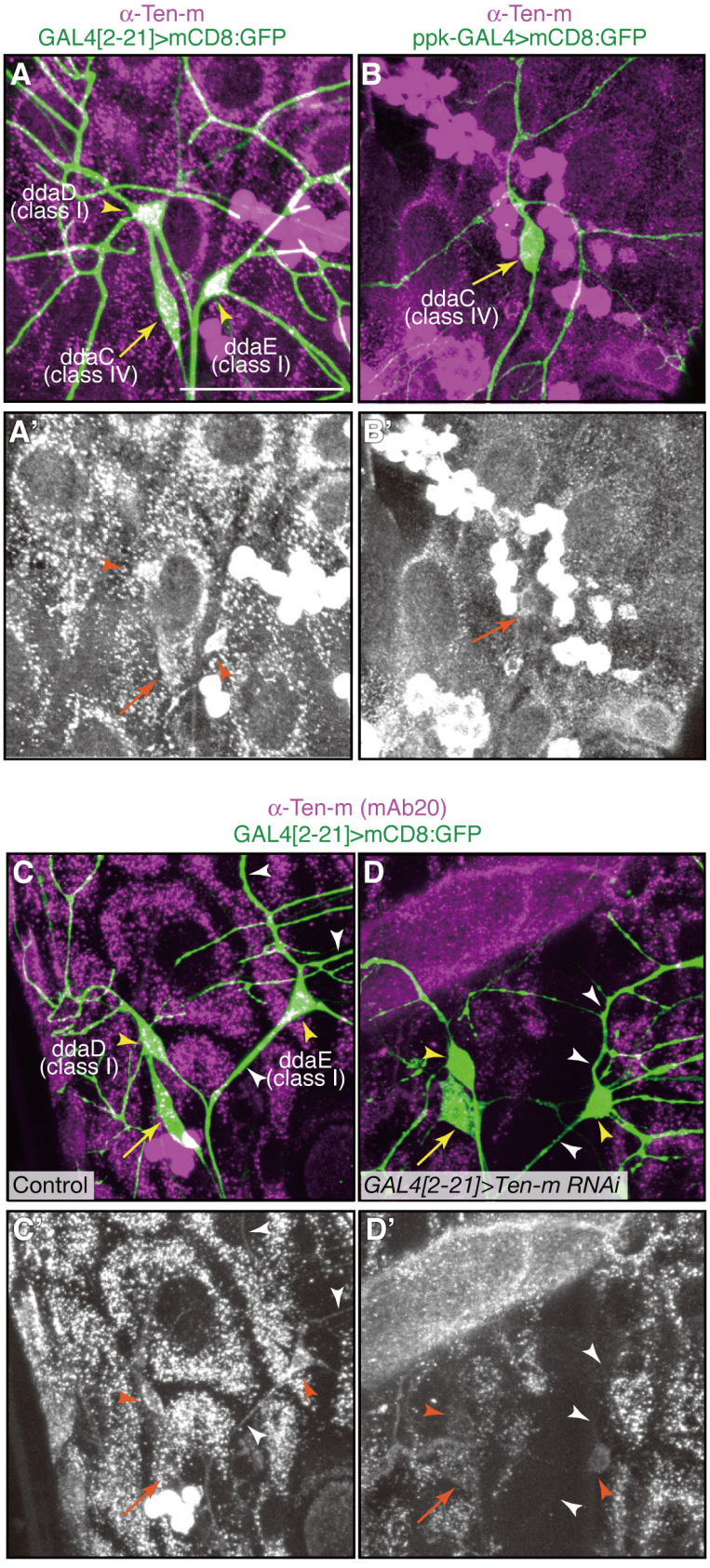

Figure 52. Ten-m expression pattern

Representative images of antibody staining of Ten-m (magenta in A, B, C, and D; and A', B', C', and D') and the marker GFP (green in A, B, C, and D).

In contrast to signals of Ten-m in class I neurons, only weak signals in class IV were observed. (C-D') Knockdown of Tem-m was confirmed by the reduced immunohisto- chemical signals in class I ddaD and ddaE. Control (C and C') and Tem-m-RNAi (D and D').

Note that I sometimes detected Ten-m signals along dendrites or axons of class I neuron ddaE (white arrowheads in C').

Relevant genotypes are *GAL4$^{2-21}$ UAS-mCD8:GFP /+* (A and A'), *ppk-GAL4 UAS-mCD8:GFP/+* (B and B'), *UAS-dicer2 /+; GAL4$^{2-21}$ UAS-mCD8:GFP /+* (C, and C'), and *UAS-dicer2/+; GAL4$^{2-21}$ UAS-mCD8:GFP/UAS-Ten -m-RNAi (VDRC51173)* (D and D').

Bars, 50 μm.

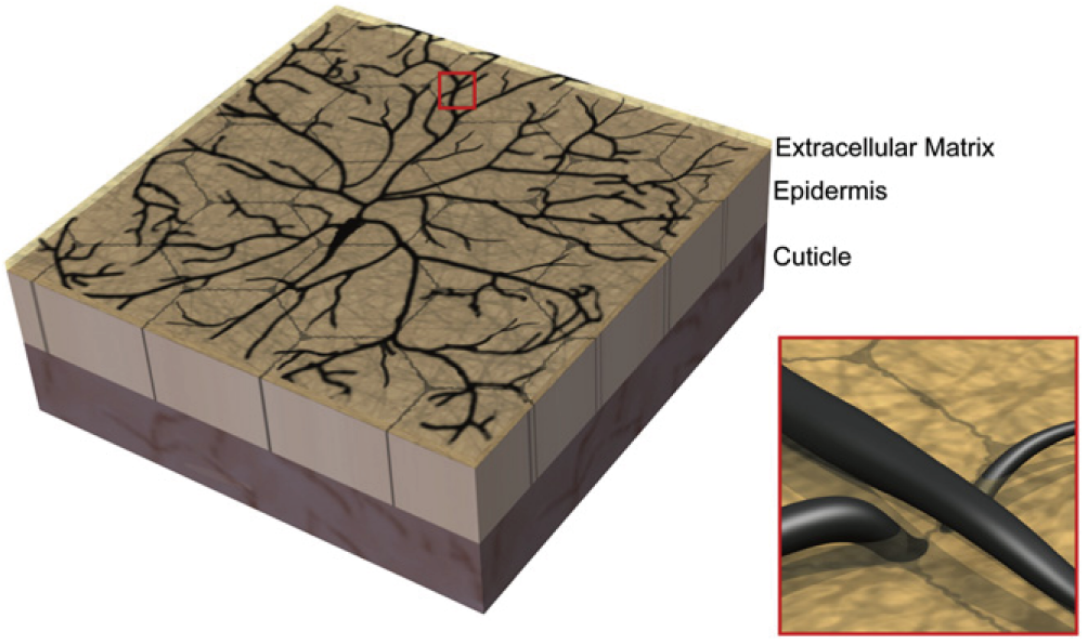

Figure 53. Interaction between dendrites and the extracellular matrix (ECM) secreted by the epidermis

Drosophila class IV dendritic arborization (da) neurons, which tile the larval body wall, grow their dendrites mainly in a two-dimensional (2D) space on the extracellular matrix (ECM) secreted by the epidermis. The dendrites bind laminin in the ECM through cell-autonomous integrin-mediated adhesion. This interaction creates a 2D environment that optimizes contact-dependent self-avoidance to prevent self-crossings in the branches. Impaired integrin function increases the number of enclosed dendrites, which pass through epidermal cells and cross other branches without direct contact (inset). Adapted from Burgess et al. (2012).

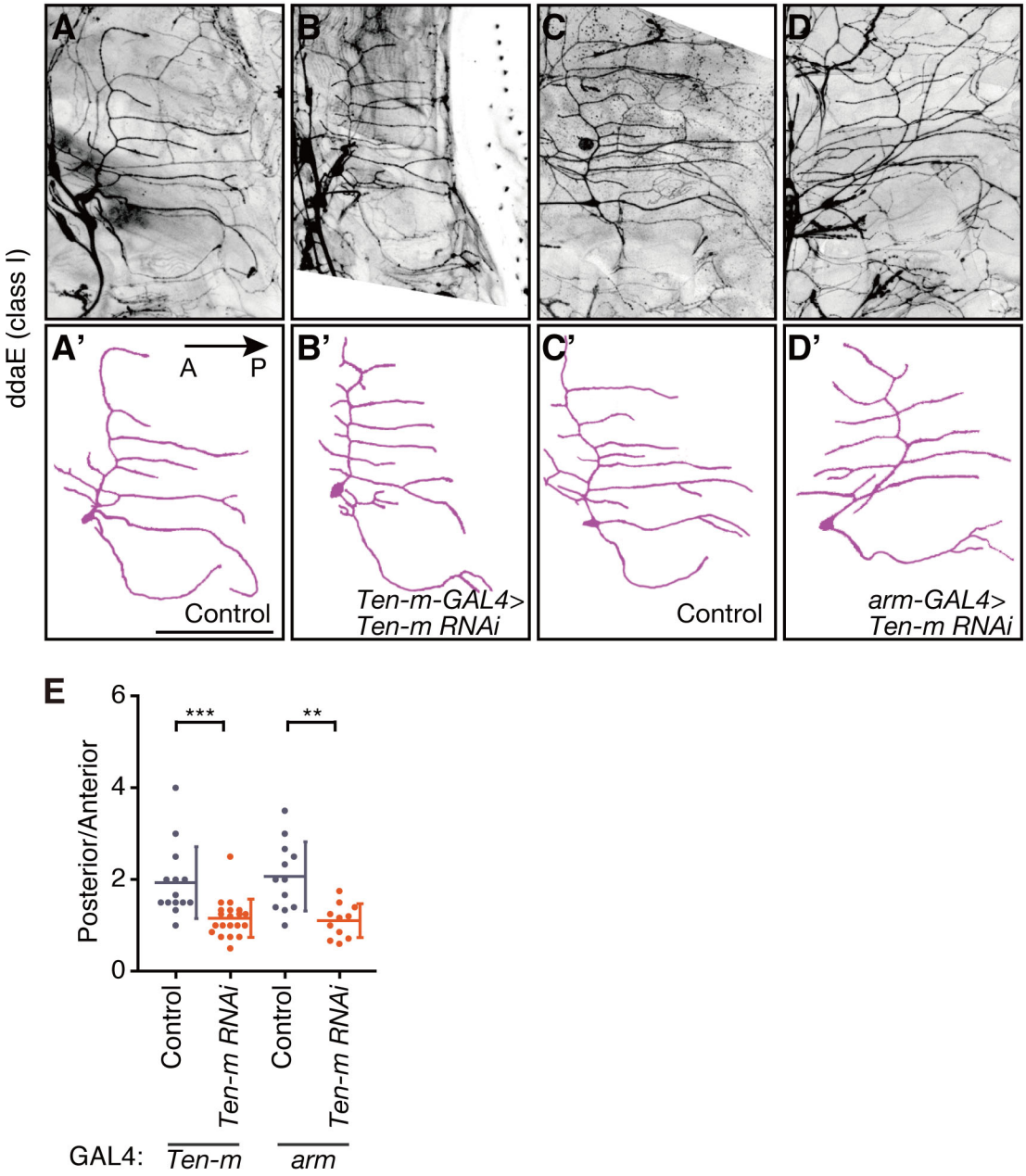

Figure 54. *Ten-m* knockdown phenotypes of class I ddaE by using *Tem-m-GAL4* or *arm-GAL4*

Phenotypes of class I neuron ddaE when *Ten-m* was knocked down by using *Ten-m-GAL4* (B and B') or *arm-GAL4* (D and D'). (A, A', C, and C') Controls. (A', B', C' and D') Tracings of A, B, C and D, respectively. Arrow represents the anterior-posterior axis. (E) Quantitative analysis. The ratio of the number of posterior-directed secondary branches to the number of anterior-directed secondary branches was plotted. Error bars indicate the mean ± s.d. ** $P <$ 0.01, *** $P <$ 0.001 (Wilcoxon-Mann-Whitney test) Actual P values are 0.0001 (*Ten-m-GAL4*), and 0.0021 (*arm-GAL4*). Relevant genotypes are *UAS-dicer2/+; +/NP6658* (A and A'), *UAS-dicer2/+; +; UAS-Ten-m-RNAi (VDRC51173)/NP6658* (B and B'), *UAS-dicer2/arm-GAL4* (C and C'), *UAS-dicer2/+; +/arm-GAL4; UAS-Ten-m-RNAi (VDRC51173)/+* (D and D').

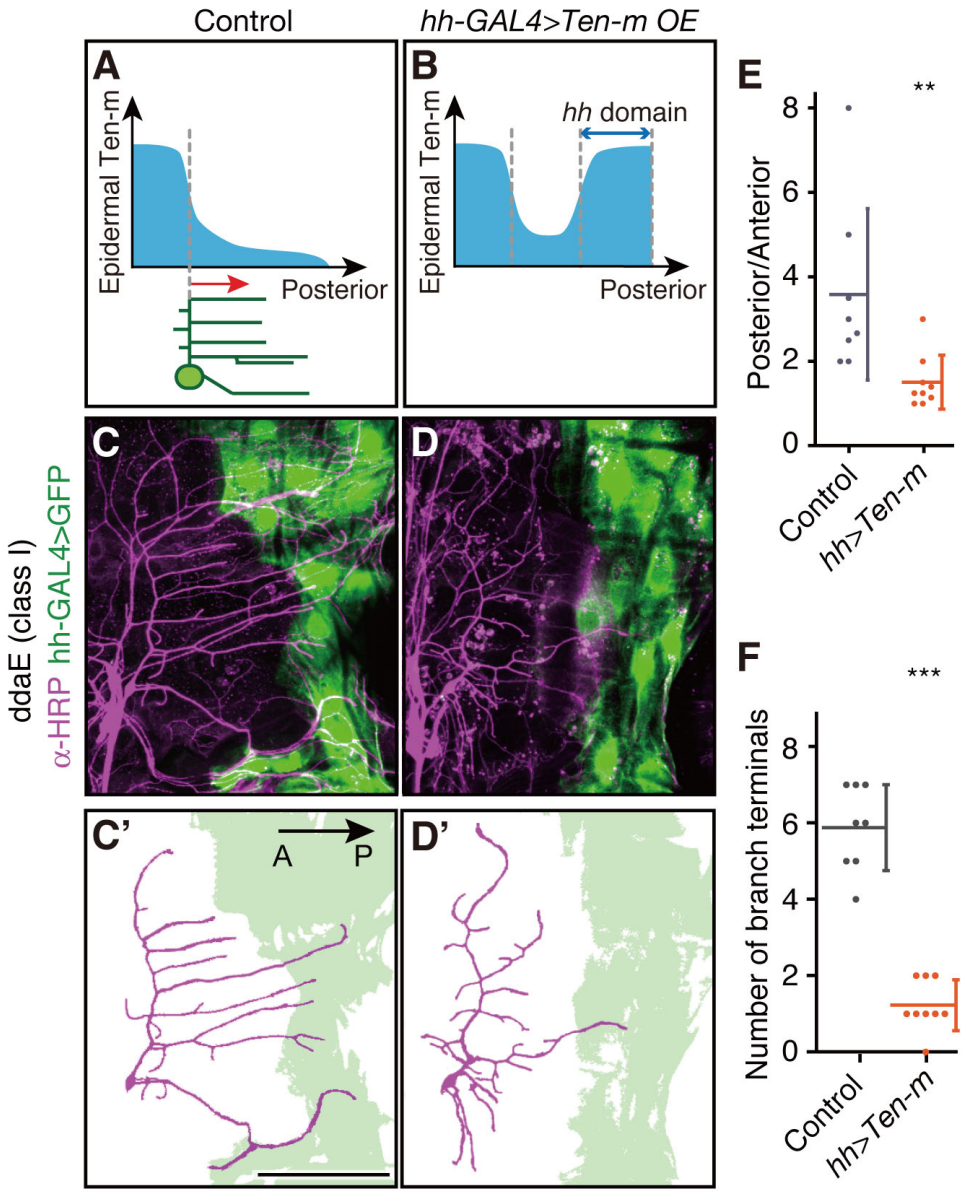

Figure 55. Effects of *Ten-m* overexpression in the epidermal *hh* domain on dendrite patterning of class I ddaE

(A and B) Schematic showing *Ten-m* overexpression in the epidermal *hh* domain.

(C-D') The *hh* domain was visualized by GFP expression driven by *hh-GAL4* (green) and dendrites were labeled by anti-HRP antibody (magenta).

(C' and D') Tracings of C and D, respectively. Arrow represents the anterior-posterior axis.

(E and F) Quantitative analysis.

(E) The ratio of the number of posterior-directed secondary branches to the number of anterior-directed secondary branches was plotted.

(F) The number of branch termini in the *hh* domain. Error bars indicate the mean ± s.d. ** $P < 0.01$, *** $P < 0.001$ (Wilcoxon-Mann-Whitney test) Actual P values are 0.0037 (E), and 0.0005 (F). Bar, 100 μm. Relevant genotypes are *+/hh-GAL4 UAS-GFP* (C and C'), *UAS-Ten-m/hh-GAL4 UAS-GFP* (D and D').

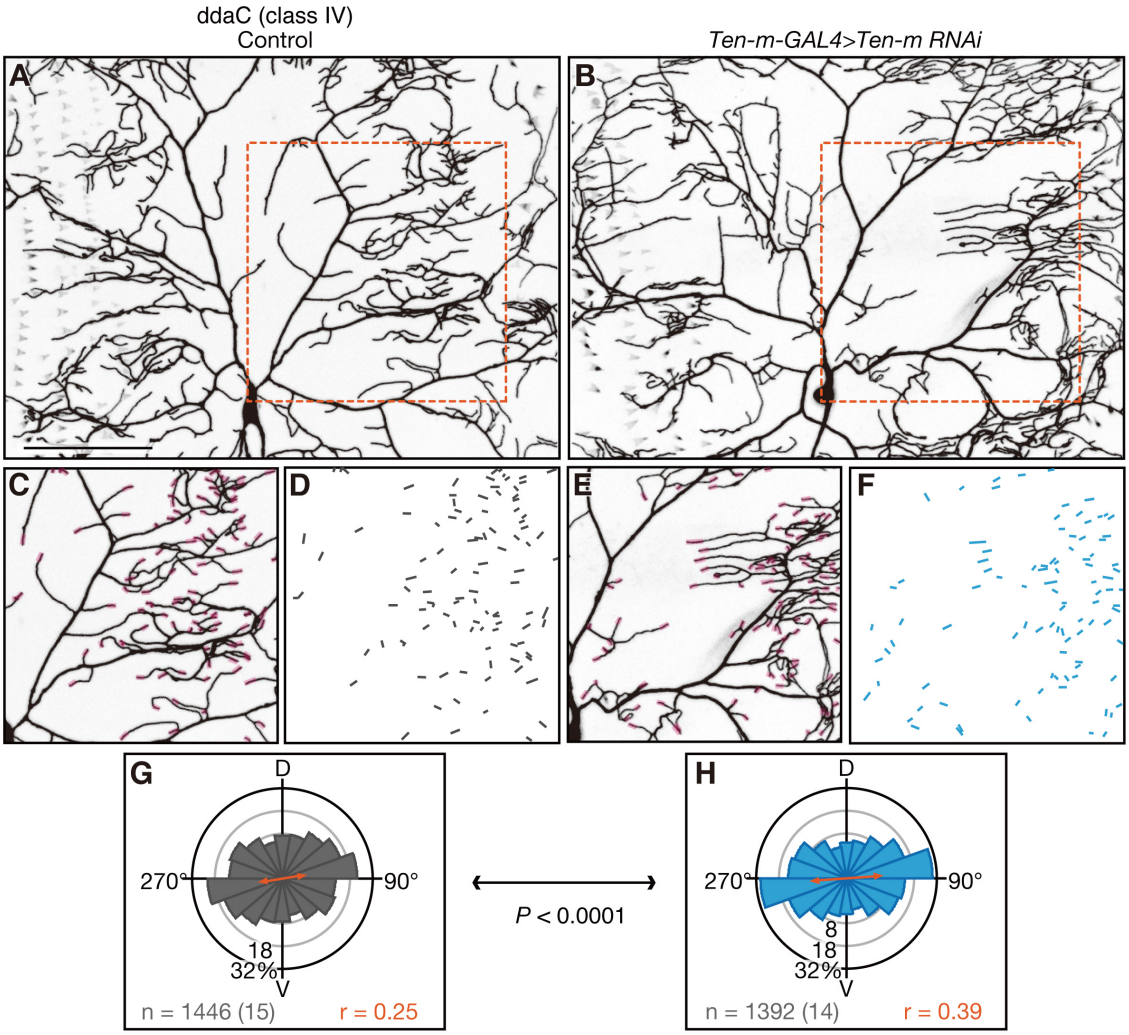

Figure 56. Effects of *Ten-m* knockdown in all *Ten-m*-expressing cell types on orientation distributions of branch termini of class IV ddaC

Images of class IV ddaC when *Ten-m* was knocked down by using *Ten-m-GAL4* (B, E, and F). (A, C, and D) Control.

(C-F) High-power images of boxed areas in A and B. Orientations of branch termini are defined by short line segments, which trace termini to 5-10 μm-distant intra-branch points (D and F). Bar, 100 μm.

(G and H) Orientation distributions of branch termini. In each rose diagram, angles are classed into 9 bins (20° for each bin) and visualized in a point symmetry manner. Data of individual genotypes were collected from 200μm x 200μm boxed areas in A and B. Indicated at a lower left-hand corner of each rose diagram are the number of branch termini and the number of neurons from which the data were collected (in parentheses). The lengths of the mean vector (orange arrows) are indicated (r). Knockdowns significantly biased the orientation distribution (Mardia-Watson-Wheeler test; actual P value is < 0.0001).

Relevant genotypes are *UAS-dicer2/ppk-CD4:tdGFP; +/NP6658* (A, C, D, and G), *UAS-dicer2/+; +/ppk-CD4:tdGFP; UAS-Ten-m-RNAi (VDRC51173)/NP6658* (B, E, F, and H).

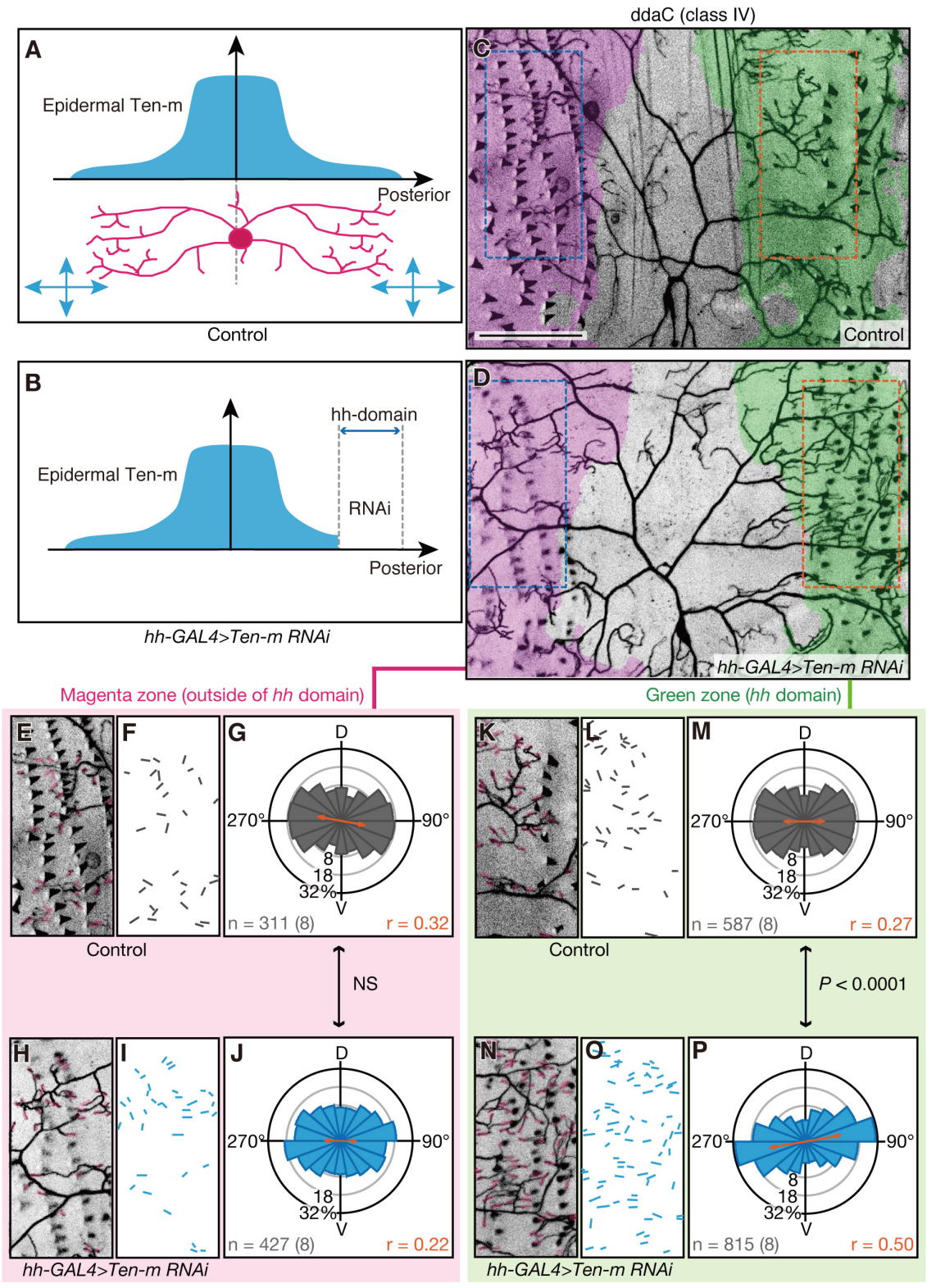

Figure 57. Effects of *Ten-m* knockdown in the epidermal *hh* domain on orientation distributions of branch termini of class IV ddaC

(A and B) Schematic showing *Ten-m* knockdown in the epidermal *hh* domain.

(D, H-I, and N-O) Images of class IV ddaC when *Ten-m* was knocked down by using *hh-GAL4*. (C, E-F, and K-L) Controls.
(E-F, H-I, K-L, and N-O) High-power images of boxed areas in C and D. Orientations of branch termini are defined by short line segments, which trace termini to 5-10 μm-distant intra-branch points (F, I , L, and O). Bar, 100 μm.
(G, J, M, and P) Orientation distributions of branch termini. In each rose diagram, angles are classed into 9 bins (20° for each bin) and visualized in a point symmetry manner. Data were collected from dorsal *hh* domains in dendritic arbors (green zones dorsal to the cell bodies) and from the sides opposite to the *hh* domains (magenta zones dorsal to the cell bodies), respectively. Indicated at a lower left-hand corner of each rose diagram are the number of branch termini and the number of neurons from which the data were collected (in parentheses). The lengths of the mean vector (orange arrows) are indicated (r). In green zone (hh-domain), *Ten-m* knockdown significantly biased the orientation distribution (Mardia-Watson-Wheeler test; actual P value is < 0.0001), whereas in the magenta zones, the distribution was statistically not altered (actual P value is 0.0502).
Relevant genotypes are *UAS-dicer2/ ppk-CD4:tdTom; +/hh-GAL4 UAS-GFP* (C, E-G, and K-M), *UAS-dicer2/+; +/ ppk-CD4:tdTom; UAS-Ten-m-RNAi (VDRC51173)/hh-GAL4 UAS-GFP* (D, H-J, and N-P). NS: Statistically not significant (*P* > 0.05).

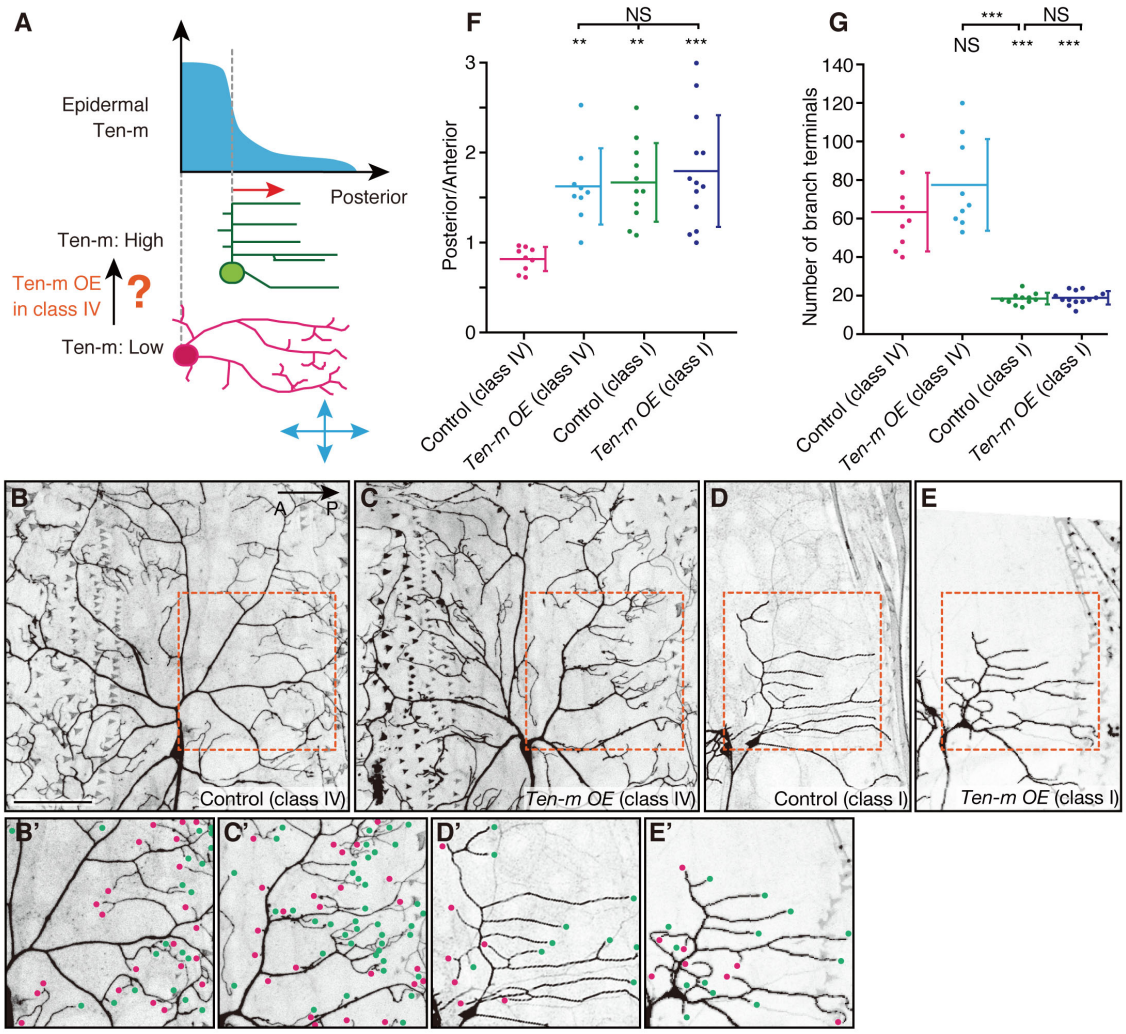

Figure 58. An effect of *Ten-m* overexpression in class IV on directional preference of branch growth along the A-P axis

(A) Schematic showing *Ten-m* overexpression in class IV ddaC. In the wild type, class IV ddaC expressed *Ten-m*, but at a much lower level than class I ddaE. I addressed whether overexpression of *Ten-m* in ddaC affected its dendrite morphogenesis or not.

(B-E') Images of class IV ddaC (B, B', C, and C') or class I ddaE (D, D', E, and E'). Controls (B, B', D, and D') and *Ten-m*-overexpressing neurons (C, C', E, and E').

(B'-E') High-power images of 200μm x 200μm boxed areas in B-E. Anterior-directed and posterior-directed termini are indicated by magenta and green points, respectively.

Bars, 100 μm. Arrow represents the anterior-posterior axis.

Relevant genotypes are *ppk-GAL4 UAS-mCD8:GFP/+* (B and B'), *ppk-GAL4 UAS-mCD8:GFP/UAS-Ten-m* (C and C'), *GAL4$^{2\text{-}21}$ UAS-mCD8:GFP/+* (D and D'), *GAL4$^{2\text{-}21}$ UAS-mCD8:GFP/UAS-Ten-m* (E and E').

(F and G) Quantitative analyses.

(F) The anterior vs. posterior directional bias in the boxed areas was quantified and statistically tested.

(G) The number of termini in the boxed areas. Error bars indicate the mean ± s.d. ** $P < 0.01$,

*** *P* < 0.001 (one-way ANOVA and HSD *post-hoc* test). NS: Statistically not significant (*P* > 0.05). Actual P values are as follows:
(F) 0.0037 (Cont. IV vs. *Ten-m OE* IV), 0.0012 (Cont. IV vs. Cont. I), 0.0001 (Cont. IV vs. *Ten-m OE* I), 0.9965 (*Ten-m OE* IV vs. Cont. I), and 0.9071 (Cont. I vs. *Ten-m OE* I).
(G) 0.1885 (Cont. IV vs. *Ten-m OE* IV), < 0.0001 (Cont. IV vs. Cont. I), < 0.0001 (Cont. IV vs. *Ten-m OE* I), < 0.0001 (*Ten-m OE* IV vs. Cont. I), and 0.9998 (Cont. I vs. *Ten-m OE* I).

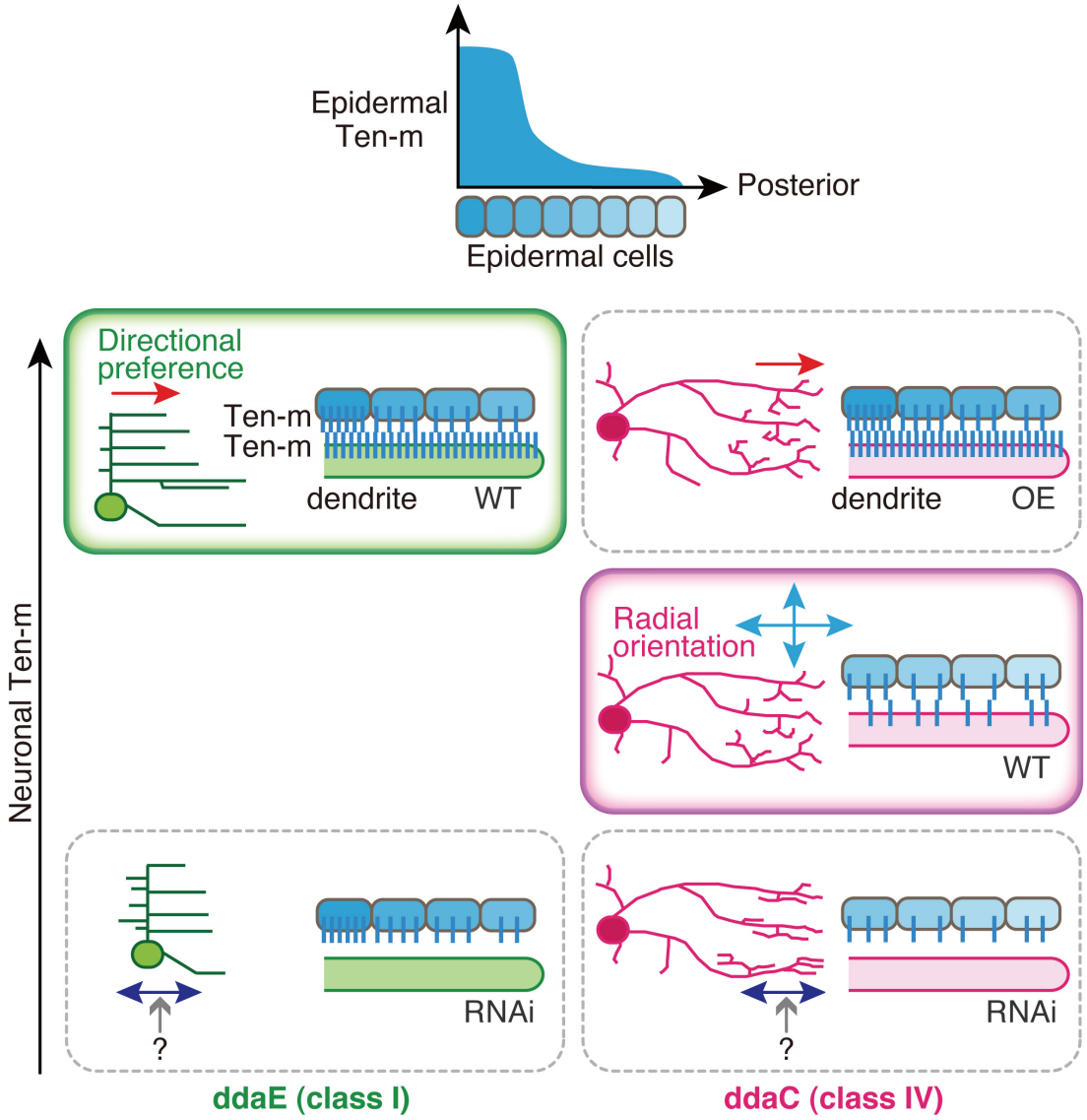

Figure 59. Summary of phenotypes and a hypothetical Ten-m-mediated dendrite-epidermis interaction in various genetic backgrounds

(Top) A diagram showing the non-uniform Ten-m expression profile in the epidermis. The X-axis represents the A-P axis and the Y-axis indicates the amount of Ten-m in the epidermis. An alignment of epidermal cells with a decreasing Ten-m amount is also schematized. The two epidermal cells from the origin along the X axis indicate Ten-m-high cells that encompass cell bodies of da neurons in the dorsal cluster, such as ddaC and ddaE.

(Left and right) Diagrams illustrating dendrite phenotypes of class I ddaE and class IV ddaC, respectively, and hypothetical Ten-m-mediated dendrite-epidermis interactions in different genetic backgrounds. Each diagram of the dendrite phenotype represents the overall ddaE arbor (left) or the posterior half of the ddaC arbor (right). Thick green- and magenta-outlined boxes illustrate wild-type (WT) ddaE and ddaC, respectively.

(Left) Ten-m-high dendrites of WT ddaE respond to the epidermal high-low Ten-m imbalance, and sprout and extend down the lower slope, realizing the predominantly

posterior-oriented comb-like pattern (arrow at the top). When the Ten-m-mediated interaction is disrupted, for example, by a cell-autonomous knockdown, dendrites no longer sense the epidermal Ten-m level, and the directional preference of the branch sprouting is abrogated (double-headed arrow at the bottom).
(Right) In WT ddaC, the low-level expression in the neurons and the epidermis ensures the relatively radial pattern of terminal branches in the *hh* domain (crossed arrows in the middle). When the Ten-m-mediated interaction is abrogated, extension of terminal branches is biased along the A-P axis by an unknown mechanism (double-headed arrow at the bottom). When Ten-m is overexpressed in ddaC, its branches respond to the higher-to-lower level of epidermal Ten-m towards the posterior border in each hemisegment, as does the WT ddaE (arrow at the top).

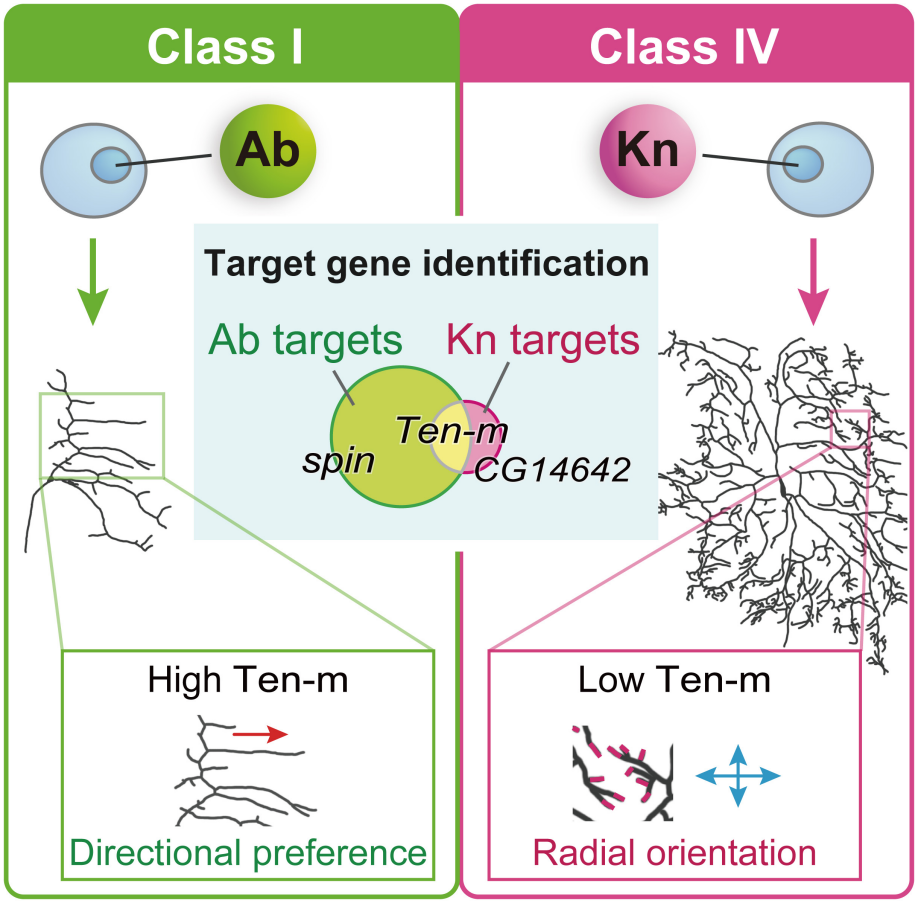

Figure 60. Summary of this study

I focused on transcriptional programs that are directed by the class I selector Ab and the class IV selector Kn. I searched for target genes of Ab and/or Kn on a whole genome scale to better understand how each TF regulates class-selective differentiation, and highlighted a subset of the target genes that are required for shaping the dendritic arbors of both or either of class-I or IV; I then focused on a common target gene *Ten-m*, and how it contributes to producing the class-selective morphological traits.

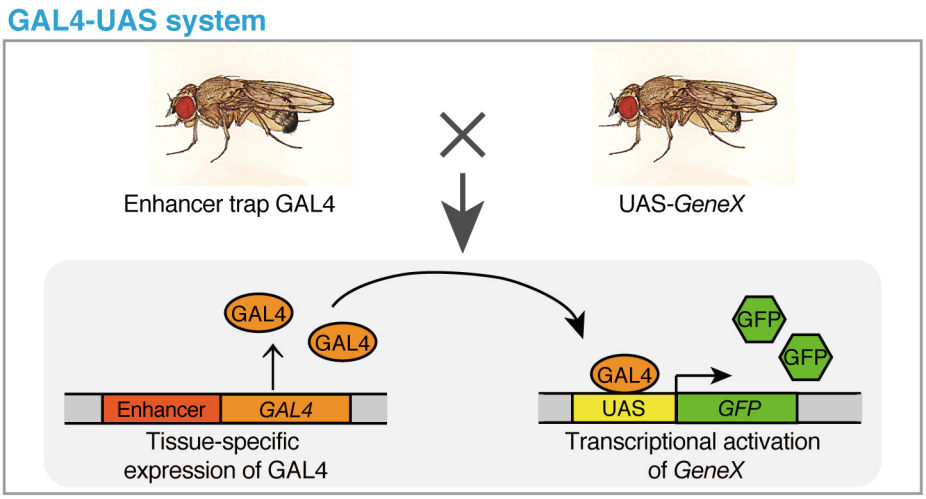

Figure 61. GAL4-UAS system

To activate the target gene in a cell- or tissue-specific pattern, flies carrying the target (*UAS-Gene X*) are crossed to flies expressing GAL4 (Enhancer Trap GAL4). In the progeny of this cross, it is possible to activate *UAS-Gene X* in cells where GAL4 is expressed and to observe the effect of this directed misexpression on development. Painting of *Drosophila* by Emily Jan is modified.

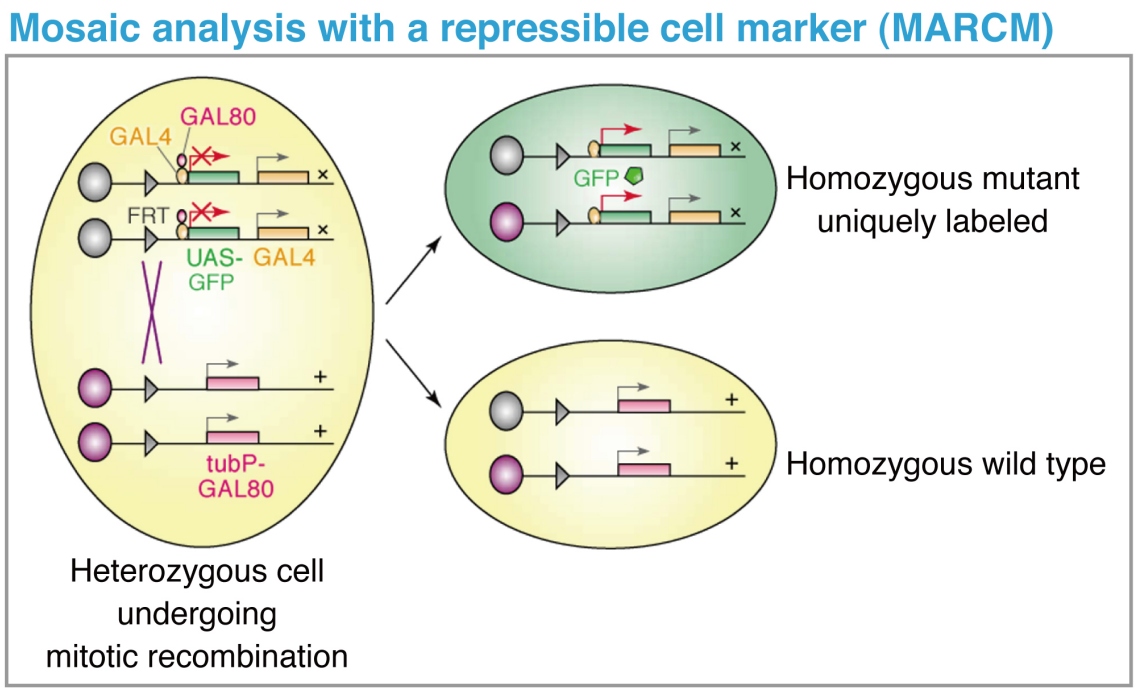

Figure 62. Genetic basis of the mosaic analysis with a repressible cell marker (MARCM) system

The MARCM system allows one to label homozygous mutant cells uniquely in mosaic tissues. After FRT site-specific mitotic recombination, a heterozygous mother cell can give rise to two daughter cells in which the chromosome arms distal to the recombination site become homozygous. *tubP-GAL80* is ubiquitously expressed and efficiently suppresses expression of a UAS-marker gene. If *tubP-GAL80* is inserted on the chromosome arm carrying the wild-type (+) gene of interest, the daughter cell homozygous for the mutant gene (x) no longer contains GAL80. Therefore, the marker gene can be specifically turned on by *GAL4* (orange box) in homozygous mutant cells (green cell). Adapted from Lee and Luo (2001).

Supplemental Tables

Table S1. Lists of the Ab or Kn BSs, of the Ab- or Kn-bound, dependent or target genes, and genes that are regulated by Ab and Kn in quantitatively differential fashions

(see accompanying Excel spreadsheet)

Among candidates of target genes that have been reported previously (Crozatier and Vincent, 2008; Hattori et al., 2007; Jinushi-Nakao et al., 2007), *pickpocket* (*ppk*) was identified as one of *ab*-dependent genes in this study (1C and 1D; see also Table S3A).

Gene symbol	log2(fold change)			
	ab ME		*kn* ME	
	microarray	qPCR	microarray	qPCR
spin	1.3	3.7		NA
ssp4	0.9	3.3		NA
CG14642	2.2	NA	1.6	0.7
CG2201	1.5	NA	1.5	NA
lola	1.8	1.9	1.6	0.2
dOrai	1.7	*	1.6	*
CG31431	4.5	1.3	3.4	1.1
Ten-m	1.9	3.5	1.3	1.5
Imp	1.2	*	1.3	*
Pak3	1.5	2.9	1.5	1.1
tai	1.2	2.8	1.4	1.2
pnr	3.0	1.1	2.4	1.1
CG30080	-2.9	*		NA
Dab	-2.0	NA	-1.9	NA
hts	-1.4	-2.1		NA
ara	-1.0	NA		NA
BicD	-1.7	NA		NA
CG34347	-2.6	NA		NA
sdk	-1.5	NA		NA
CG31140	-3.5	NA	-2.4	*
dlp	-2.4	*	-2.2	*
SK	-2.7	*	-2.5	*
sog	-3.0	*	-1.4	*
Ptp10D	-2.2	-3.3	-1.6	-9.8

Table S2. Fold changes of expression levels of the selected target genes
Comparison of log2(fold-change) made by triplicate microarray experiments and qPCR results for target genes listed in Table S4. An asterisk indicates that fold-change could not be calculated because cDNA from the control sample was not amplified. NA: not analyzed.

Table S3. List of the dependent and the bound genes implicated in neuronal differentiation or neuronal functions, or those encoding miRNA
(see accompanying Excel spreadsheet)

Target genes that yielded strong phenotypes of either class I and/or IV when knocked down

	Gene symbol	Gene function	Binding		Expression		Regulation	RNAi		OE		*kn* ME + RNAi
					ab ME	*kn* ME		I	IV	I	IV	
Up-regulated targets	***spin***	Endosome to lysosome transport	Ab		↑			M			R	NA
	ssp4 (Patronin)	Microtubule severing	Ab		↑			M	R,A	NA	NA	NA
	CG14642	Serine-type endopeptidase activity		Kn	↑	↑			P	NA	NA	+
	CG2201	Choline kinase activity		Kn	↑	↑		M		NA	NA	NA
	lola	Regulation of transcription	Ab	Kn	↑	↑	Ab↑↑ Kn↑	R	R	R	R	+
	dOrai (olf186-F)	Store-operated Ca2+ release-activated Ca2+ channel	Ab	Kn	↑	↑		R	R		A	+
	CG31431	fibroblast growth factor-activated receptor activity	Ab	Kn	↑	↑		M	R	NA	NA	NA
	Ten-m	Cell adhesion	Ab	Kn	↑	↑	Ab↑↑ Kn↑	M	A		M	-
	Imp	mRNA binding	Ab	Kn	↑	↑			R		I	+
	Pak3	Receptor signaling protein serine/threonine kinase activity	Ab	Kn	↑	↑			R	M	A	+
	tai	Transcription coactivator activity	Ab	Kn	↑	↑		R		R,M	A	NA
	pnr	Regulation of transcription	Ab	Kn	↑	↑		M		NA	NA	NA
Down-regulated targets	***CG30080***	Regulation of transcription	Ab		↓			M		NA	NA	NA
	Dab	Signaling pathway	Ab		↓	↓		M			A	NA
	hts	Actin capping	Ab	Kn	↓			M	A	NA	NA	NA
	ara	Regulation of transcription	Ab	Kn	↓			M			R	NA
	BicD	RNA transport	Ab	Kn	↓			M				NA
	CG34347	Actin binding	Ab	Kn	↓			M		NA	NA	NA
	sdk	Pigment cell differentiation	Ab	Kn	↓			M		NA	NA	NA
	CG31140	Diacylglycerol kinase activity		Kn	↓	↓		M		NA	NA	NA
	dlp	Glypican-type heparan sulfate proteoglycan	Ab	Kn	↓	↓		M	M,A		A	NA
	SK	Small conductance calcium-activated potassium channel	Ab	Kn	↓	↓		M		NA	NA	NA
	sog	BMP signaling pathway	Ab	Kn	↓	↓	Ab↓↓ Kn↓	M		NA	NA	NA
	Ptp10D	Protein amino acid dephosphorylation	Ab	Kn	↓	↓			R	NA	NA	NA

A: Abnormal terminals, I: Increased arborization, M: Misrouting, P: Positioning of branch points, R: Reduced arborization

Table S4. Target genes that yielded strong phenotypes of either class I and/or IV when knocked down

The column labeled “Binding” indicates whether each target gene was bound by Ab, Kn, or both. Colored shading indicates altered expression by Ab and/or Kn. In the column of “Expression”, upward and downward arrows indicate up-regulation and down-regulation by Ab or Kn misexpression (ME), respectively. The column labeled “Regulation” indicates

target genes that were either up- or down-regulated more strongly by Ab ME. In the columns labeled “RNAi” and “OE”, only knockdown or overexpression that gave strong phenotypes in “I” (class I) or “IV” (class IV) are labeled. I have categorized those phenotypes and have added annotations at the bottom. NA: not analyzed. In the columns labeled “*kn* ME + RNAi”, knockdowns that suppressed *kn* ME phenotype are labeled as “+”.

References

Abraira, V.E., and Ginty, D.D. (2013). The sensory neurons of touch. Neuron *79*, 618-639.

Adolph, S.K., DeLotto, R., Nielsen, F.C., and Christiansen, J. (2009). Embryonic expression of Drosophila IMP in the developing CNS and PNS. Gene expression patterns : GEP *9*, 138-143.

Agrawal, N., Venkiteswaran, G., Sadaf, S., Padmanabhan, N., Banerjee, S., and Hasan, G. (2010). Inositol 1,4,5-trisphosphate receptor and dSTIM function in Drosophila insulin-producing neurons regulates systemic intracellular calcium homeostasis and flight. J Neurosci *30*, 1301-1313.

Antinucci, P., Nikolaou, N., Meyer, M.P., and Hindges, R. (2013). Teneurin-3 specifies morphological and functional connectivity of retinal ganglion cells in the vertebrate visual system. Cell reports *5*, 582-592.

Bahri, S., Wang, S., Conder, R., Choy, J., Vlachos, S., Dong, K., Merino, C., Sigrist, S., Molnar, C., Yang, X.*, et al.* (2010). The leading edge during dorsal closure as a model for epithelial plasticity: Pak is required for recruitment of the Scribble complex and septate junction formation. Development *137*, 2023-2032.

Bai, J., Uehara, Y., and Montell, D.J. (2000). Regulation of invasive cell behavior by taiman, a Drosophila protein related to AIB1, a steroid receptor coactivator amplified in breast cancer. Cell *103*, 1047-1058.

Baumgartner, S., Martin, D., Hagios, C., and Chiquet-Ehrismann, R. (1994). Tenm, a Drosophila gene related to tenascin, is a new pair-rule gene. The EMBO journal *13*, 3728-3740.

Benjamini, Y., and Hochberg, Y. (1995). Controlling the False Discovery Rate - a Practical and Powerful Approach to Multiple Testing. J Roy Stat Soc B Met *57*, 289-300.

Bertrand, N., Castro, D.S., and Guillemot, F. (2002). Proneural genes and the specification of neural cell types. Nature reviews *3*, 517-530.

Bianco, A., Dienstbier, M., Salter, H.K., Gatto, G., and Bullock, S.L. (2010). Bicaudal-D regulates fragile X mental retardation protein levels, motility, and function during neuronal morphogenesis. Curr Biol *20*, 1487-1492.

Birney, E., Stamatoyannopoulos, J.A., Dutta, A., Guigo, R., Gingeras, T.R., Margulies, E.H., Weng, Z., Snyder, M., Dermitzakis, E.T., Thurman, R.E.*, et al.* (2007). Identification and analysis of functional elements in 1% of the human genome by the ENCODE pilot project. Nature *447*, 799-816.

Boylan, K.L., Mische, S., Li, M., Marques, G., Morin, X., Chia, W., and Hays, T.S. (2008). Motility screen identifies Drosophila IGF-II mRNA-binding protein--zipcode-binding

protein acting in oogenesis and synaptogenesis. PLoS genetics *4*, e36.

Brand, A.H., and Perrimon, N. (1993). Targeted gene expression as a means of altering cell fates and generating dominant phenotypes. Development *118*, 401-415.

Burgess, R.W., Garrett, A.M., and Tadenev, A.L. (2012). Contact is repulsive, but please note the "enclosed". Developmental cell *22*, 5-6.

Castro, D.S., Martynoga, B., Parras, C., Ramesh, V., Pacary, E., Johnston, C., Drechsel, D., Lebel-Potter, M., Garcia, L.G., Hunt, C.*, et al.* (2011). A novel function of the proneural factor Ascl1 in progenitor proliferation identified by genome-wide characterization of its targets. Genes & development *25*, 930-945.

Chen, X., Xu, H., Yuan, P., Fang, F., Huss, M., Vega, V.B., Wong, E., Orlov, Y.L., Zhang, W., Jiang, J.*, et al.* (2008). Integration of external signaling pathways with the core transcriptional network in embryonic stem cells. Cell *133*, 1106-1117.

Choksi, S.P., Southall, T.D., Bossing, T., Edoff, K., de Wit, E., Fischer, B.E., van Steensel, B., Micklem, G., and Brand, A.H. (2006). Prospero acts as a binary switch between self-renewal and differentiation in Drosophila neural stem cells. Developmental cell *11*, 775-789.

Corty, M.M., Matthews, B.J., and Grueber, W.B. (2009). Molecules and mechanisms of dendrite development in Drosophila. Development *136*, 1049-1061.

Crozatier, M., and Vincent, A. (2008). Control of multidendritic neuron differentiation in Drosophila: the role of Collier. Developmental biology *315*, 232-242.

Dalla Torre di Sanguinetto, S.A., Dasen, J.S., and Arber, S. (2008). Transcriptional mechanisms controlling motor neuron diversity and connectivity. Curr Opin Neurobiol *18*, 36-43.

Delmas, P., Hao, J., and Rodat-Despoix, L. (2011). Molecular mechanisms of mechanotransduction in mammalian sensory neurons. Nature reviews *12*, 139-153.

Dennis, G., Jr., Sherman, B.T., Hosack, D.A., Yang, J., Gao, W., Lane, H.C., and Lempicki, R.A. (2003). DAVID: Database for Annotation, Visualization, and Integrated Discovery. Genome biology *4*, P3.

Dermaut, B., Norga, K.K., Kania, A., Verstreken, P., Pan, H., Zhou, Y., Callaerts, P., and Bellen, H.J. (2005). Aberrant lysosomal carbohydrate storage accompanies endocytic defects and neurodegeneration in Drosophila benchwarmer. The Journal of cell biology *170*, 127-139.

Dubois, L., Enriquez, J., Daburon, V., Crozet, F., Lebreton, G., Crozatier, M., and Vincent, A. (2007). Collier transcription in a single Drosophila muscle lineage: the combinatorial control of muscle identity. Development *134*, 4347-4355.

Dubois, L., and Vincent, A. (2001). The COE--Collier/Olf1/EBF--transcription factors: structural conservation and diversity of developmental functions. Mechanisms of

development *108*, 3-12.

Emoto, K., He, Y., Ye, B., Grueber, W.B., Adler, P.N., Jan, L.Y., and Jan, Y.N. (2004). Control of dendritic branching and tiling by the Tricornered-kinase/Furry signaling pathway in Drosophila sensory neurons. Cell *119*, 245-256.

Feske, S. (2007). Calcium signalling in lymphocyte activation and disease. Nature reviews Immunology *7*, 690-702.

Filion, G.J., van Bemmel, J.G., Braunschweig, U., Talhout, W., Kind, J., Ward, L.D., Brugman, W., de Castro, I.J., Kerkhoven, R.M., Bussemaker, H.J.*, et al.* (2010). Systematic protein location mapping reveals five principal chromatin types in Drosophila cells. Cell *143*, 212-224.

Fishell, G., and Hanashima, C. (2008). Pyramidal neurons grow up and change their mind. Neuron *57*, 333-338.

Fujita, P.A., Rhead, B., Zweig, A.S., Hinrichs, A.S., Karolchik, D., Cline, M.S., Goldman, M., Barber, G.P., Clawson, H., Coelho, A.*, et al.* (2011). The UCSC Genome Browser database: update 2011. Nucleic acids research *39*, D876-882.

Gao, F.B., Brenman, J.E., Jan, L.Y., and Jan, Y.N. (1999). Genes regulating dendritic outgrowth, branching, and routing in Drosophila. Genes & development *13*, 2549-2561.

Giniger, E., Tietje, K., Jan, L.Y., and Jan, Y.N. (1994). lola encodes a putative transcription factor required for axon growth and guidance in Drosophila. Development *120*, 1385-1398.

Goulding, M. (2009). Circuits controlling vertebrate locomotion: moving in a new direction. Nature reviews *10*, 507-518.

Grueber, W.B., Jan, L.Y., and Jan, Y.N. (2002). Tiling of the Drosophila epidermis by multidendritic sensory neurons. Development *129*, 2867-2878.

Grueber, W.B., Jan, L.Y., and Jan, Y.N. (2003). Different levels of the homeodomain protein cut regulate distinct dendrite branching patterns of Drosophila multidendritic neurons. Cell *112*, 805-818.

Grueber, W.B., Ye, B., Yang, C.H., Younger, S., Borden, K., Jan, L.Y., and Jan, Y.N. (2007). Projections of Drosophila multidendritic neurons in the central nervous system: links with peripheral dendrite morphology. Development *134*, 55-64.

Guelen, L., Pagie, L., Brasset, E., Meuleman, W., Faza, M.B., Talhout, W., Eussen, B.H., de Klein, A., Wessels, L., de Laat, W.*, et al.* (2008). Domain organization of human chromosomes revealed by mapping of nuclear lamina interactions. Nature *453*, 948-951.

Haeussler, M., and Joly, J.S. (2011). When needles look like hay: how to find tissue-specific enhancers in model organism genomes. Developmental biology *350*, 239-254.

Hammer, Ø., Harper, D.A.T. & Ryan, P.D. (2001). Past: paleontological statistics software package for education and data analysis. Palaeontologia Electronica *4*, 9.

Han, C., Jan, L.Y., and Jan, Y.N. (2011). Enhancer-driven membrane markers for analysis of nonautonomous mechanisms reveal neuron-glia interactions in Drosophila. Proceedings of the National Academy of Sciences of the United States of America *108*, 9673-9678.

Han, C., Wang, D., Soba, P., Zhu, S., Lin, X., Jan, L.Y., and Jan, Y.N. (2012). Integrins regulate repulsion-mediated dendritic patterning of drosophila sensory neurons by restricting dendrites in a 2D space. Neuron *73*, 64-78.

Hattori, Y., Sugimura, K., and Uemura, T. (2007). Selective expression of Knot/Collier, a transcriptional regulator of the EBF/Olf-1 family, endows the Drosophila sensory system with neuronal class-specific elaborated dendritic patterns. Genes to cells : devoted to molecular & cellular mechanisms *12*, 1011-1022.

Hausser, M., and Mel, B. (2003). Dendrites: bug or feature? Curr Opin Neurobiol *13*, 372-383.

Hobert, O. (2011). Regulation of terminal differentiation programs in the nervous system. Annual review of cell and developmental biology *27*, 681-696.

Hobert, O., Carrera, I., and Stefanakis, N. (2010). The molecular and gene regulatory signature of a neuron. Trends in neurosciences *33*, 435-445.

Hong, W., Mosca, T.J., and Luo, L. (2012). Teneurins instruct synaptic partner matching in an olfactory map. Nature *484*, 201-207.

Horiuchi, T., Giniger, E., and Aigaki, T. (2003). Alternative trans-splicing of constant and variable exons of a Drosophila axon guidance gene, lola. Genes & development *17*, 2496-2501.

Hu, S., Fambrough, D., Atashi, J.R., Goodman, C.S., and Crews, S.T. (1995). The Drosophila abrupt gene encodes a BTB-zinc finger regulatory protein that controls the specificity of neuromuscular connections. Genes & development *9*, 2936-2948.

Huang da, W., Sherman, B.T., and Lempicki, R.A. (2009). Systematic and integrative analysis of large gene lists using DAVID bioinformatics resources. Nature protocols *4*, 44-57.

Hughes, C.L., and Thomas, J.B. (2007). A sensory feedback circuit coordinates muscle activity in Drosophila. Molecular and cellular neurosciences *35*, 383-396.

Hwang, R.Y., Zhong, L., Xu, Y., Johnson, T., Zhang, F., Deisseroth, K., and Tracey, W.D. (2007). Nociceptive neurons protect Drosophila larvae from parasitoid wasps. Curr Biol *17*, 2105-2116.

Im, S.H., and Galko, M.J. (2012). Pokes, sunburn, and hot sauce: Drosophila as an emerging model for the biology of nociception. Dev Dyn *241*, 16-26.

Irizarry, R.A., Bolstad, B.M., Collin, F., Cope, L.M., Hobbs, B., and Speed, T.P. (2003). Summaries of Affymetrix GeneChip probe level data. Nucleic acids research *31*, e15.

Iyer, E.P., Iyer, S.C., Sulkowski, M.J., and Cox, D.N. (2009). Isolation and purification of Drosophil peripheral neurons by magnetic bead sorting. J Vis Exp.

Iyer, E.P., Iyer, S.C., Sullivan, L., Wang, D., Meduri, R., Graybeal, L.L., and Cox, D.N. (2013). Functional genomic analyses of two morphologically distinct classes of Drosophila sensory neurons: post-mitotic roles of transcription factors in dendritic patterning. PloS one *8*, e72434.

Jan, Y.N., and Jan, L.Y. (2010). Branching out: mechanisms of dendritic arborization. Nature reviews *11*, 316-328.

Jan, Y.N., and Jan, L.Y. (2003). The control of dendrite development. Neuron *40*, 229-242.

Jinushi-Nakao, S., Arvind, R., Amikura, R., Kinameri, E., Liu, A.W., and Moore, A.W. (2007). Knot/Collier and cut control different aspects of dendrite cytoskeleton and synergize to define final arbor shape. Neuron *56*, 963-978.

Kharchenko, P.V., Alekseyenko, A.A., Schwartz, Y.B., Minoda, A., Riddle, N.C., Ernst, J., Sabo, P.J., Larschan, E., Gorchakov, A.A., Gu, T.*, et al.* (2010). Comprehensive analysis of the chromatin landscape in Drosophila melanogaster. Nature *471*, 480-485.

Kim, I.J., Zhang, Y., Yamagata, M., Meister, M., and Sanes, J.R. (2008). Molecular identification of a retinal cell type that responds to upward motion. Nature *452*, 478-482.

Kim, M.E., Shrestha, B.R., Blazeski, R., Mason, C.A., and Grueber, W.B. (2012a). Integrins establish dendrite-substrate relationships that promote dendritic self-avoidance and patterning in drosophila sensory neurons. Neuron *73*, 79-91.

Kim, S.E., Coste, B., Chadha, A., Cook, B., and Patapoutian, A. (2012b). The role of Drosophila Piezo in mechanical nociception. Nature *483*, 209-212.

Kimura, H., Usui, T., Tsubouchi, A., and Uemura, T. (2006). Potential dual molecular interaction of the Drosophila 7-pass transmembrane cadherin Flamingo in dendritic morphogenesis. Journal of cell science *119*, 1118-1129.

Kind, J., Vaquerizas, J.M., Gebhardt, P., Gentzel, M., Luscombe, N.M., Bertone, P., and Akhtar, A. (2008). Genome-wide analysis reveals MOF as a key regulator of dosage compensation and gene expression in Drosophila. Cell *133*, 813-828.

Kwong, C., Adryan, B., Bell, I., Meadows, L., Russell, S., Manak, J.R., and White, R. (2008). Stability and dynamics of polycomb target sites in Drosophila development. PLoS genetics *4*, e1000178.

Landgraf, M., and Evers, J.F. (2005). Control of dendritic diversity. Current opinion in cell biology *17*, 690-696.

Leamey, C.A., Merlin, S., Lattouf, P., Sawatari, A., Zhou, X., Demel, N., Glendining, K.A.,

Oohashi, T., Sur, M., and Fassler, R. (2007). Ten_m3 regulates eye-specific patterning in the mammalian visual pathway and is required for binocular vision. PLoS biology *5*, e241.

Lee, T., and Luo, L. (2001). Mosaic analysis with a repressible cell marker (MARCM) for Drosophila neural development. Trends in neurosciences *24*, 251-254.

Levine, A., Bashan-Ahrend, A., Budai-Hadrian, O., Gartenberg, D., Menasherow, S., and Wides, R. (1994). Odd Oz: a novel Drosophila pair rule gene. Cell *77*, 587-598.

Li, L. (2009). GADEM: a genetic algorithm guided formation of spaced dyads coupled with an EM algorithm for motif discovery. Journal of computational biology : a journal of computational molecular cell biology *16*, 317-329.

Li, W., Wang, F., Menut, L., and Gao, F.B. (2004). BTB/POZ-zinc finger protein abrupt suppresses dendritic branching in a neuronal subtype-specific and dosage-dependent manner. Neuron *43*, 823-834.

London, M., and Hausser, M. (2005). Dendritic computation. Annu Rev Neurosci *28*, 503-532.

Long, H., Ou, Y., Rao, Y., and van Meyel, D.J. (2009). Dendrite branching and self-avoidance are controlled by Turtle, a conserved IgSF protein in Drosophila. Development *136*, 3475-3484.

Ly, C.V., Yao, C.K., Verstreken, P., Ohyama, T., and Bellen, H.J. (2008). straightjacket is required for the synaptic stabilization of cacophony, a voltage-gated calcium channel alpha1 subunit. The Journal of cell biology *181*, 157-170.

Machanick, P., and Bailey, T.L. (2011). MEME-ChIP: motif analysis of large DNA datasets. Bioinformatics *27*, 1696-1697.

Matsubara, D., Horiuchi, S.Y., Shimono, K., Usui, T., and Uemura, T. (2011). The seven-pass transmembrane cadherin Flamingo controls dendritic self-avoidance via its binding to a LIM domain protein, Espinas, in Drosophila sensory neurons. Genes & development *25*, 1982-1996.

McQuilton, P., St Pierre, S.E., and Thurmond, J. (2012). FlyBase 101--the basics of navigating FlyBase. Nucleic acids research *40*, D706-714.

Mosca, T.J., Hong, W., Dani, V.S., Favaloro, V., and Luo, L. (2012). Trans-synaptic Teneurin signalling in neuromuscular synapse organization and target choice. Nature *484*, 237-241.

Munro, T.P., Kwon, S., Schnapp, B.J., and St Johnston, D. (2006). A repeated IMP-binding motif controls oskar mRNA translation and anchoring independently of Drosophila melanogaster IMP. The Journal of cell biology *172*, 577-588.

Nagoshi, E., Sugino, K., Kula, E., Okazaki, E., Tachibana, T., Nelson, S., and Rosbash, M. (2010). Dissecting differential gene expression within the circadian neuronal circuit of

Drosophila. Nature neuroscience *13*, 60-68.

Negre, N., Brown, C.D., Ma, L., Bristow, C.A., Miller, S.W., Wagner, U., Kheradpour, P., Eaton, M.L., Loriaux, P., Sealfon, R.*, et al.* (2011). A cis-regulatory map of the Drosophila genome. Nature *471*, 527-531.

Ou, Y., Chwalla, B., Landgraf, M., and van Meyel, D.J. (2008). Identification of genes influencing dendrite morphogenesis in developing peripheral sensory and central motor neurons. Neural development *3*, 16.

Parrish, J.Z., Emoto, K., Jan, L.Y., and Jan, Y.N. (2007). Polycomb genes interact with the tumor suppressor genes hippo and warts in the maintenance of Drosophila sensory neuron dendrites. Genes & development *21*, 956-972.

Parrish, J.Z., Kim, M.D., Jan, L.Y., and Jan, Y.N. (2006). Genome-wide analyses identify transcription factors required for proper morphogenesis of Drosophila sensory neuron dendrites. Genes & development *20*, 820-835.

Parrish, J.Z., Xu, P., Kim, C.C., Jan, L.Y., and Jan, Y.N. (2009). The microRNA bantam functions in epithelial cells to regulate scaling growth of dendrite arbors in drosophila sensory neurons. Neuron *63*, 788-802.

Pickersgill, H., Kalverda, B., de Wit, E., Talhout, W., Fornerod, M., and van Steensel, B. (2006). Characterization of the Drosophila melanogaster genome at the nuclear lamina. Nature genetics *38*, 1005-1014.

Ramón y Cajal, S. (1911). Histology of the nervous system of man and vertebrates, (1995 translation). Oxford University Press, Oxford, UK.

Roy, S., Ernst, J., Kharchenko, P.V., Kheradpour, P., Negre, N., Eaton, M.L., Landolin, J.M., Bristow, C.A., Ma, L., Lin, M.F.*, et al.* (2010). Identification of functional elements and regulatory circuits by Drosophila modENCODE. Science *330*, 1787-1797.

Satoh, D., Sato, D., Tsuyama, T., Saito, M., Ohkura, H., Rolls, M.M., Ishikawa, F., and Uemura, T. (2008). Spatial control of branching within dendritic arbors by dynein-dependent transport of Rab5-endosomes. Nature cell biology *10*, 1164-1171.

Schwartz, Y.B., Kahn, T.G., Nix, D.A., Li, X.Y., Bourgon, R., Biggin, M., and Pirrotta, V. (2006). Genome-wide analysis of Polycomb targets in Drosophila melanogaster. Nature genetics *38*, 700-705.

Schwartz, Y.B., Kahn, T.G., Stenberg, P., Ohno, K., Bourgon, R., and Pirrotta, V. (2010). Alternative epigenetic chromatin states of polycomb target genes. PLoS genetics *6*, e1000805.

Sekine, S.U., Haraguchi, S., Chao, K., Kato, T., Luo, L., Miura, M., and Chihara, T. (2013). Meigo governs dendrite targeting specificity by modulating ephrin level and N-glycosylation. Nature neuroscience *16*, 683-691.

Shen, H. (2013). See-through brains clarify connections. Nature *496*, 151.

Shimono, K., Fujimoto, A., Tsuyama, T., Yamamoto-Kochi, M., Sato, M., Hattori, Y., Sugimura, K., Usui, T., Kimura, K., and Uemura, T. (2009). Multidendritic sensory neurons in the adult Drosophila abdomen: origins, dendritic morphology, and segment- and age-dependent programmed cell death. Neural development *4*, 37.

Shin, H., Liu, T., Manrai, A.K., and Liu, X.S. (2009). CEAS: cis-regulatory element annotation system. Bioinformatics *25*, 2605-2606.

Smyth, G.K. (2004). Linear models and empirical bayes methods for assessing differential expression in microarray experiments. Statistical applications in genetics and molecular biology *3*, Article3.

Song, S., Cooperman, J., Letting, D.L., Blobel, G.A., and Choi, J.K. (2004). Identification of cyclin D3 as a direct target of E2A using DamID. Molecular and cellular biology *24*, 8790-8802.

Song, W., Onishi, M., Jan, L.Y., and Jan, Y.N. (2007). Peripheral multidendritic sensory neurons are necessary for rhythmic locomotion behavior in Drosophila larvae. Proceedings of the National Academy of Sciences of the United States of America *104*, 5199-5204.

Southall, T.D., and Brand, A.H. (2009). Neural stem cell transcriptional networks highlight genes essential for nervous system development. The EMBO journal *28*, 3799-3807.

Spletter, M.L., Liu, J., Liu, J., Su, H., Giniger, E., Komiyama, T., Quake, S., and Luo, L. (2007). Lola regulates Drosophila olfactory projection neuron identity and targeting specificity. Neural development *2*, 14.

Sugimura, K., Satoh, D., Estes, P., Crews, S., and Uemura, T. (2004). Development of morphological diversity of dendrites in Drosophila by the BTB-zinc finger protein abrupt. Neuron *43*, 809-822.

Sugino, K., Hempel, C.M., Miller, M.N., Hattox, A.M., Shapiro, P., Wu, C., Huang, Z.J., and Nelson, S.B. (2006). Molecular taxonomy of major neuronal classes in the adult mouse forebrain. Nature neuroscience *9*, 99-107.

Sun, L.V., Chen, L., Greil, F., Negre, N., Li, T.R., Cavalli, G., Zhao, H., Van Steensel, B., and White, K.P. (2003). Protein-DNA interaction mapping using genomic tiling path microarrays in Drosophila. Proceedings of the National Academy of Sciences of the United States of America *100*, 9428-9433.

Sweeney, S.T., and Davis, G.W. (2002). Unrestricted synaptic growth in spinster-a late endosomal protein implicated in TGF-beta-mediated synaptic growth regulation. Neuron *36*, 403-416.

Tanimoto, H., Itoh, S., ten Dijke, P., and Tabata, T. (2000). Hedgehog creates a gradient of DPP activity in Drosophila wing imaginal discs. Molecular cell *5*, 59-71.

Thor, S. (2013). Neuroscience: stem cells in multiple time zones. Nature *498*, 441-443.

Tolhuis, B., de Wit, E., Muijrers, I., Teunissen, H., Talhout, W., van Steensel, B., and van Lohuizen, M. (2006). Genome-wide profiling of PRC1 and PRC2 Polycomb chromatin binding in Drosophila melanogaster. Nature genetics *38*, 694-699.

Tracey, W.D., Jr., Wilson, R.I., Laurent, G., and Benzer, S. (2003). painless, a Drosophila gene essential for nociception. Cell *113*, 261-273.

van Steensel, B., Delrow, J., and Bussemaker, H.J. (2003). Genomewide analysis of Drosophila GAGA factor target genes reveals context-dependent DNA binding. Proceedings of the National Academy of Sciences of the United States of America *100*, 2580-2585.

van Steensel, B., Delrow, J., and Henikoff, S. (2001). Chromatin profiling using targeted DNA adenine methyltransferase. Nature genetics *27*, 304-308.

van Steensel, B., and Henikoff, S. (2000). Identification of in vivo DNA targets of chromatin proteins using tethered dam methyltransferase. Nat Biotechnol *18*, 424-428.

Venkiteswaran, G., and Hasan, G. (2009). Intracellular Ca2+ signaling and store-operated Ca2+ entry are required in Drosophila neurons for flight. Proceedings of the National Academy of Sciences of the United States of America *106*, 10326-10331.

Volgyi, B., Chheda, S., and Bloomfield, S.A. (2009). Tracer coupling patterns of the ganglion cell subtypes in the mouse retina. The Journal of comparative neurology *512*, 664-687.

Vrieseling, E., and Arber, S. (2006). Target-induced transcriptional control of dendritic patterning and connectivity in motor neurons by the ETS gene Pea3. Cell *127*, 1439-1452.

Wilks, T.A., Harvey, A.R., and Rodger, J. (2013). Seeing with Two Eyes: Integration of Binocular Retinal Projections in the Brain (InTech).

Xiang, Y., Yuan, Q., Vogt, N., Looger, L.L., Jan, L.Y., and Jan, Y.N. (2010). Light-avoidance-mediating photoreceptors tile the Drosophila larval body wall. Nature *468*, 921-926.

Yamamoto, M., Ueda, R., Takahashi, K., Saigo, K., and Uemura, T. (2006). Control of axonal sprouting and dendrite branching by the Nrg-Ank complex at the neuron-glia interface. Curr Biol *16*, 1678-1683.

Ye, B., Zhang, Y., Song, W., Younger, S.H., Jan, L.Y., and Jan, Y.N. (2007). Growing dendrites and axons differ in their reliance on the secretory pathway. Cell *130*, 717-729.

Yisraeli, J.K. (2005). VICKZ proteins: a multi-talented family of regulatory RNA-binding proteins. Biology of the cell / under the auspices of the European Cell Biology Organization *97*, 87-96.

Young, T.R., and Leamey, C.A. (2009). Teneurins: important regulators of neural circuitry. The international journal of biochemistry & cell biology *41*, 990-993.

Zheng, L., Michelson, Y., Freger, V., Avraham, Z., Venken, K.J., Bellen, H.J., Justice, M.J., and Wides, R. (2011). Drosophila Ten-m and filamin affect motor neuron growth cone guidance. PloS one *6*, e22956.

Zheng, Y., Josefowicz, S.Z., Kas, A., Chu, T.T., Gavin, M.A., and Rudensky, A.Y. (2007). Genome-wide analysis of Foxp3 target genes in developing and mature regulatory T cells. Nature *445*, 936-940.

Zheng, Y., Wildonger, J., Ye, B., Zhang, Y., Kita, A., Younger, S.H., Zimmerman, S., Jan, L.Y., and Jan, Y.N. (2008). Dynein is required for polarized dendritic transport and uniform microtubule orientation in axons. Nature cell biology *10*, 1172-1180.